Delft University of Technology

Quantum effects of superconducting phase

Erdmanis, J.

DOI
10.4233/uuid:24872ead-0ee2-4854-9728-fe04f5957ca2

Publication date
2021

Document Version
Final published version

Citation (APA)
Erdmanis, J. (2021). *Quantum effects of superconducting phase*. [Dissertation (TU Delft), Delft University of Technology]. https://doi.org/10.4233/uuid:24872ead-0ee2-4854-9728-fe04f5957ca2

Important note
To cite this publication, please use the final published version (if applicable).
Please check the document version above.

Copyright
Other than for strictly personal use, it is not permitted to download, forward or distribute the text or part of it, without the consent of the author(s) and/or copyright holder(s), unless the work is under an open content license such as Creative Commons.

Takedown policy
Please contact us and provide details if you believe this document breaches copyrights.
We will remove access to the work immediately and investigate your claim.

This work is downloaded from Delft University of Technology.
For technical reasons the number of authors shown on this cover page is limited to a maximum of 10.

QUANTUM EFFECTS OF SUPERCONDUCTING PHASE

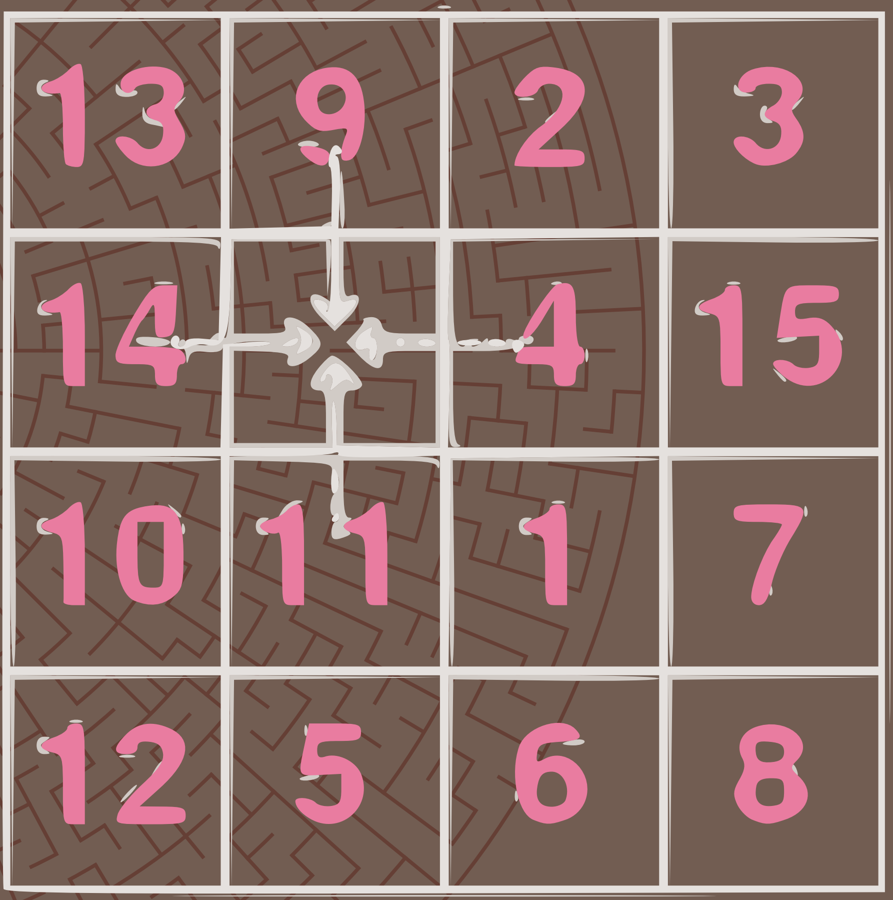

Jānis Erdmanis

QUANTUM EFFECTS OF SUPERCONDUCTING PHASE

Proefschrift

ter verkrijging van de graad van doctor
aan de Technische Universiteit Delft,
op gezag van de Rector Magnificus Prof.dr.ir. T.H.J.J. van der Hagen,
voorzitter van het College voor Promoties,
in het openbaar te verdedigen op
woensdag 8 december 2021 om 15:00 uur

door

Jānis ERDMANIS

Master of Science in Physics,
Universiteit van Letland, Riga, Letland,
geboren te Valmiera, Letland

Dit proefschrift is goedgekeurd door de

promotor: Prof.dr. Y.V. Nazarov
promotor: Prof.dr. Y.M. Blanter

Samenstelling promotiecommissie:

Rector Magnificus,	voorzitter
Prof.dr. Y.V. Nazarov,	Technische Universiteit Delft, promotor
Prof.dr. Y.M. Blanter	Technische Universiteit Delft, promotor
Onafhankelijke leden:	
Prof.dr. G.A. Steele	Technische Universiteit Delft
Prof.dr.ir A. Brinkman	Universiteit Twente
Prof.dr. C. Strunk	Universität Regensburg
Prof.dr. L.S. Levitov	MIT
Prof.dr. C.W.J. Beenakker	Universiteit Leiden
Prof.dr. J.M. Thijssen	Technische Universiteit Delft, reservelid

European Research Council
Established by the European Commission

Keywords: superconductivity, superconducting circuits, phase slips, topology

Printed by: Print&Bind

Front & Back: A gap in knowledge is much like a gap in 15 puzzle, allowing to slide pieces around one by one until a better composition is achieved.

Copyright © 2021 by J. Erdmanis

Casimir PhD series, Delft-Leiden 2021-43

ISBN 978-90-8593-507-0

An electronic version of this dissertation is available at
http://repository.tudelft.nl/.

Sam Loyd's Cyclopedia of Puzzles pp. 234–235

People know what they do; frequently they know why they do what they do;
but what they don't know is what what they do does.

Michel Foucault

CONTENTS

SUMMARY

The microscopic theory of superconductivity proposed by John Bardeen, Leon Cooper, and John Robert Schrieffer has been a vital milestone of condensed matter physics and the basis of development of new quantum technologies. It explained the superconductivity as an emergent phenomenon arising from weak phonon-mediated attraction of individual electrons and giving raise to what we know as the superconducting condensate characterized by a complex order parameter that has a modulus and a phase. In many superconductors, the modulus defines a spectral gap.

Because of the gap, the superconductor cannot host low-energy single-electron excitations. When an electron excitation comes from a normal metal to a superconductor, it is reflected as a hole, and an incoming hole is reflected as an electron. This process is known as Andreev reflection. In the last 60 years, the superconducting heterostructures have been extensively studied, Josephson junction being the most prominent example. The electrons and holes in such structures perform never-ending roundtrips between the superconductor interfaces. This gives raise to Andreev bound state spectrum, that determines the supercurrent-phase relation of the nanostructure.

There is a recent upheaval of interest in nanostructures with multiple superconducting terminals. One of the subjects of interest is Weyl points: for four or more terminals, the Andreev bands can cross zero energy at a point in the space of superconducting phases space. This is a direct analogy to band crossings in the Brillion zone of topological materials. Another subject is the peculiarities of the spectrum under conditions of the superconducting proximity effect, where the gapped-gapless transition in the space of superconducting phase has been observed.

It has been long known that the superconducting phase is, in fact, a quantum variable that is canonically conjugated to charge. It is the basis of all applications for the development of superconducting quantum computing. The 2π periodicity of the superconducting phase also manifests itself in a non-trivial way. It enables events known as quantum phase slips, those promise metrological applications, for instance, a metrological standard of current. Thus it is of great interest to understand the quantum effects of the superconducting phase in novel and more complex setups. This is the main theme of this thesis.

In Chapter 2, we analyze the effects of quantum fluctuations in the vicinity of Weyl points appearing in multiterminal superconducting junctions. To introduce quantum fluctuations of the superconducting phases at the terminals, we embed the junction in a linear circuit. Such circuit separates the external fixed phase from the internal phase, which is softly confined to an external one. The quantum fluctuations produce a drastic change of the bandstructure in the vicinity of the Weyl point. In the semiclassical limit, they flatten it in two of the three directions forming a degenerate subspace we name a Weyl Disk. Degenerate subspaces are attractive from the point of view of quantum computation. We investigate the quantum manipulations within a Weyl disk in Chapter 3. There, we demonstrate the feasibility of holonomic manipulation and propose a swap gate where the readout and initialization are performed outside the disk.

In Chapter 4, we analyze the effect of quantum fluctuations for a generic semiclassical superconducting nanostructure connected to multiple superconducting terminals, which exhibit gap-gapless transition in the superconducting phase space. This Chapter focuses on a special point where two gapped phases are separated by an infinitely narrow gapless phase. We derive a generic quantum field theory that describes the situation and proves a drastic change in the phase diagram in the close vicinity of the special point.

A phase slip is another type of superconducting phase fluctuation. While the concept of coherent quantum phase slips is well-established and predicts current quantization in a.c. driven phase-slip devices, no conclusive experimental observation of quantized current plateaux is presented yet. In Chapter 5, we argue that the known difficulties of such observation can be circumvented in a novel setup consisting of two-phase slips in series that are modulated with a gate voltage. In this Chapter, we investigate the setup in strong, weak, and intermediate coupling regimes. The regimes are defined by the ratio of the gate capacitance and the effective capacitance of phase-slip junctions. In addition, we consider finite temperature effects on the plateau width and give an empirical scaling for those.

SAMENVATTING

De microscopische theorie van supergeleiding, voorgesteld door John Bardeen, Leon Cooper en John Robert Schrieffer, is een cruciale mijlpaal geweest in de fysica van de gecondenseerde materie en de basis voor de ontwikkeling van nieuwe kwantumtechnologieën. Het verklaarde de supergeleiding als een opkomend fenomeen dat voortkomt uit een zwakke fonon-gemedieerde aantrekking van individuele elektronen en aanleiding geeft tot wat we kennen als het supergeleidende condensaat dat wordt gekenmerkt door een complexe ordeparameter die een modulus en een fase heeft. In veel supergeleiders definieert de modulus een spectrale opening.

Vanwege de opening kan de supergeleider geen enkele elektron-excitaties met lage energie bevatten. Wanneer een elektronenexcitatie van een normaal metaal naar een supergeleider komt, wordt het gereflecteerd als een gat en een inkomend gat wordt gereflecteerd als een elektron. Dit proces staat bekend als Andreev-reflectie. In de afgelopen 60 jaar zijn de supergeleidende heterostructuren uitgebreid bestudeerd, waarvan de Josephson-junctie het meest prominente voorbeeld is. De elektronen en gaten in dergelijke structuren voeren eindeloze rondreizen uit tussen de supergeleiderinterfaces. Dit geeft een verhoging van het Andreev-gebonden toestandsspectrum, dat de superstroom-faserelatie van de nanostructuur bepaalt.

Er is een recente omwenteling van interesse in nanostructuren met meerdere supergeleidende terminals. Een van de interessante onderwerpen zijn Weyl-punten: voor vier of meer terminals kunnen de Andreev-banden nul-energie oversteken op een punt in de ruimte van supergeleidende fasenruimte. Dit is een directe analogie met bandovergangen in de Brillion-zone van topologische materialen. Een ander onderwerp zijn de eigenaardigheden van het spectrum onder omstandigheden van het supergeleidende nabijheidseffect, waarbij de gapped-gapless overgang in de ruimte van de supergeleidende fase is waargenomen.

Het is al lang bekend dat de supergeleidende fase in feite een kwantumvariabele is die canoniek wordt geconjugeerd met lading. Het is de basis van alle toepassingen voor de ontwikkeling van supergeleidende quantum computing. De 2π periodiciteit van de supergeleidende fase manifesteert zich ook op een niet-triviale manier. Het maakt gebeurtenissen mogelijk die bekend staanals kwantumfaseverschuivingen, die metrologische toepassingen beloven, bijvoorbeeld een metrologische stroomstandaard. Het is dus van groot belang om de kwantumeffecten van de supergeleidende fase in nieuwe en complexere opstellingen te begrijpen. Dit is het hoofdthema van dit proefschrift.

In Hoofdstuk 2 analyseren we de effecten van kwantumfluctuaties in de buurt van Weyl-punten die voorkomen in multiterminale supergeleidende juncties. Om kwantumfluctuaties van de supergeleidende fasen op de terminals te introduceren, hebben we de junctie ingebed in een lineair circuit. Zo'n circuit scheidt de externe vaste fase van de interne fase, die zachtjes wordt beperkt tot een externe. De kwantumfluctuaties veroorzaken een drastische verandering van de bandstructuur in de buurt van het Weylpunt.

In de semiklassieke limiet, maken ze het plat in twee van de drie richtingen en vormen een gedegenereerde deelruimte die we een Weyl-schijf noemen. Gedegenereerde deelruimten zijn aantrekkelijk vanuit het oogpunt van kwantumberekening. We onderzoeken de kwantummanipulaties binnen een Weyl-schijf in Hoofdstuk 3. Daar demonstreren we de haalbaarheid van holonomische manipulatie en stellen we een swap-gate voor waarbij het uitlezen en initialiseren buiten de schijf wordt uitgevoerd.

In Hoofdstuk 4 analyseren we het effect van kwantumfluctuaties voor een generieke semiklassieke supergeleidende nanostructuur verbonden met meerdere supergeleidende terminals, die een gap-gapless overgang vertonen in de supergeleidende faseruimte. Dit hoofdstuk concentreert zich op een speciaal punt waar twee fasen met tussenpozen worden gescheiden door een oneindig smalle fase zonder tussenruimte. We leiden een generieke kwantumveldentheorie af die de situatie beschrijft en een drastische verandering in het fasediagram in de directe omgeving van het speciale punt aantoont.

Een faseverschuiving is een ander type supergeleidende fasefluctuatie. Hoewel het concept van coherente kwantumfaseverschuivingen goed ingeburgerd is en de huidige kwantisatie in a.c. aangedreven phase-slip apparaten, is er nog geen sluitende experimentele observatie van gekwantiseerde huidige plateaus gepresenteerd. In Hoofdstuk 5 beargumenteren we dat de bekende problemen van dergelijke waarnemingen kunnen worden omzeild in een nieuwe opstelling die bestaat uit tweefasige slips in serie die worden gemoduleerd met een poortspanning. In dit hoofdstuk onderzoeken we de opstelling in sterke, zwakke en intermediaire koppelingsregimes. De regimes worden bepaald door de verhouding van de poortcapaciteit en de effectieve capaciteit van fase-slipovergangen. Daarnaast houden we rekening met eindige temperatuureffecten op de plateaubreedte en geven we daarvoor een empirische schaal.

1

INTRODUCTION

Less you need more you grow.

Rich Hickey

This chapter outlines the key ideas necessary to understand and model quantum effects of the superconducting phase for two elements appearing in the subsequent chapters of this thesis, namely phase slip and multiterminal superconducting junction. To bridge these ideas, I provide an elaborate introduction into superconductivity from where I build the narrative and develop techniques necessary to understand the thesis as a whole. A guiding principle to writing this chapter was my own needs. For my past self before my PhD started when I had only a faint image of solid-state physics, and for my future self years later, as a reference to remember what my PhD was about, now allowing me to forget and to rest my mind in peace to open for new ideas and experiences.

1.1. PREFACE

Already at a young age, I was fascinated with the fact that a single physics formula can explain a great variety of experiences we see every day in different contexts. It is so beautiful to see different sets of knowledge melding together with ease to form an unexpected explanation, and a prediction, proving the permanence of new knowledge to be only complementary to the old one. This mere beauty drove me to study physics after high school. At university I learned about importance of reference frame where one collects structures the known facts so they can be easily recalled and put into practice. While doing my PhD research I learned it to be even more significant for science: it enables one to ask a question with impact and it is an antidote to Kafkaesque experiences. With this, let us build a reference frame for my thesis.

In 1908 Heike Kamerlingh Onnes at Leiden University in the Netherlands produced liquid helium with a boiling temperature at 4.2 K for the first time, thereby pioneering low temperature research. In 1911, in course of studying the resistance of different metals at low temperatures, Onnes observed that at a temperature of 4.15 K, the resistance of mercury disappears [1]. This phenomenon, known as superconductivity, was later on observed in a wide variety of metals and alloys where niobium-titanium is the most commonly used one today [2, 3]. This property had enabled a number of technological applications ranging from lossless electric power transmission lines, particle colliders and confiners where the use of superconductors enables creation of magnetic field of previously inaccessible strength, to such a technological masterpiece as MRI medical devices [3]. These all applications would be here as if medieval craftsmen were building cruiser warships and blacksmiths were forging steam engines today, even if no one would have managed to understand the origin of the phenomenon.

It took 39 years since the discovery of superconductivity till Lev Landau and Vitaly Ginzburg provided a phenomenological description of superconducting phase transitions by introducing a complex order parameter which has a magnitude and a phase [4]. Before this time, condensed matter physics matured explaining emergent phenomena in solids and liquids - magnetism, superfluidity, Bose-Einstein condensates - by application of quantum mechanics to condensed matter problems [5–7]. Inspired by the success of Landau-Ginzburd theory, a few years later, in 1956, John Bardeen, Leon Cooper, and John Robert Schrieffer proposed a microscopic theory of superconductivity [8]. They explained it as a phenomenon emerging from the phonon-mediated electron attraction.

In 1962, Josephson exploited the quantum origin of the superconductor order parameter to come up with a microscopic theory that predicted a current between two weakly coupled superconductors to depend on the phase difference between the two in a fundamental way [9]. Later on, this phenomenon known as the Josephson effect was generalized to arbitrary coupling between superconductor reservoirs with the help of the concept of Andreev bound states [10, 11]. Josephson effect enabled precise metrological applications for voltage standard and ultra-sensitive magnetic field sensors SQUIDs, which in fact you find in practically every MRI scanner [12]. In all these applications, the superconducting phase is a classical variable.

However, already in the 1960s Anderson took the microscopic theory of superconductivity more seriously [13]. He argued that the superconducting phase experiences quantum fluctuations being the canonically conjugated variable to electric charge, since the phase is a sum of the phases of all individual electrons in the condensate. This is a common knowledge today that has given rise to the field of circuit quantum electrodynamics [14] and has enabled the creation of various superconducting qubits - charge, flux [10, 15, 16] and Andreev [17, 18], to name a few.

In this Thesis, we shall explore various quantum effects of superconducting phase fluctuations. In Chapter 2, we consider a Weyl point coupled to an external linear circuit. We show that this gives rise to a new phenomenon: a formation of a degenerate parametric subspace named Weyl disk. In Chapter 3, we further investigate the Weyl disk to demonstrate the possibility of holonomic quantum manipulation. In Chapter 4 we consider the superconducting proximity effect in the presence of quantum fluctuations of the phases to find the drastic effect of the fluctuations on the gap-gapless transition. Lastly, in Chapter 5, we explore the quantum phase slips, fluctuations of the phase of a specific form. We consider a circuit consisting of two phase slip junctions and demonstrate that it is relatively easy to synchronize two phase slips in series to obtain the quantized current plateaux.

1.2. SUPERCONDUCTIVITY

For a common folk who has heard a bit about physics, superconductivity is connected with its macroscopic industrial applications. Let it be lossless electricity transport and powerful electromagnets used in levitating trains and magnetic resonance imaging [2, 3]. The less common association is with CERN, and ITER projects superconductor magnets trap the charged particles in extreme fields. All these are devised from a single property that the superconductor does not have resistance and hence its name.

However, superconductors can not sustain infinite currents, and at sufficiently large magnetic fields or currents that produce it lose their zero resistance property and become a poor metallic conductor. Even this simple property had found a place in industrial fault current limiters [19] and most sensitive calorimeters as ones used in CERN to detect exotic elementary particles [20]. All these applications come from an accidental discovery at Leiden in 1911 for mercury resistance measurements.

Since then, understanding of the quantum origin of superconductivity had opened floodgates in microscopic applications. Single-photon detectors [21], flux and charge qubits [10, 15, 16], a high precision voltage standard [22, 23], and SQUID for ultrasensitive magnetometry [12], to name a few, enabled by a Josephson junction [9]. Besides a Josephson junction, under active research are superconductivity heterostructures promising better quantum computing [17, 18, 24–26] and meteorology [27–30] to develop a better current standard.

1.2.1. BCS GROUND STATE

The microscopic theory of superconductivity raises from a single assumption that there is an attractive interaction between electrons with opposite spin and momenta [31, 32]. But how could it be so? Assuredly, it is not due to gravitation as electron mass is tiny compared to Columb's repulsion. Instead, it turns out that the interaction with the nucleus deforms the lattice in the same way as steel balls placed on a rubber sheet deforms it and thus if placed in close proximity, attracts each other, which we know as a phonon-mediated interaction.

This simplified picture can be understood in a second quantization language. We can make a single electron excitation with a momentum k with creation $\hat{c}_k^\dagger$ and destroy with annihilation $\hat{c}_k$ operators which satisfy the usual anticomutation relations for fermions. That enables us to represent a pair of interacting electrons for a given momenta as $Z_k^\dagger = c_{k,\uparrow} c_{-k,\downarrow}$ which has a total momenta zero. We know that at interaction the momenta of the two interacting electrons are conserved thus it must end in some arbitrary state $Z_{k'}^\dagger$ thus we can write the Hamiltonian describing the situation for a closed system as follows:

$$H = \sum_{k\sigma} \xi_k c_{k\sigma}^\dagger c_{k\sigma} + \frac{1}{N} \sum_{kk'} V_{kk'} Z_k^\dagger Z_{k'} \tag{1.1}$$

where ξ_k are the individual energy levels of electrons in absence of superconductivity, $V_{kk'}$ is the attractive interaction between electrons with opposite momenta and N is the number of electrons in the microcanonical ensemble [32].

To understand the Hamiltonian a mean field approximation is often used. In a simple language it entails replacing the operator product $AB \approx \langle A \rangle B + A \langle B \rangle - \langle A \rangle \langle B \rangle$ which is valid as long as $(A - \langle A \rangle)(B - \langle B \rangle) \to 0$. Bardeen, Cooper and Schrieffer realized that superconductivity can be understood if one chooses $A = Z_k^\dagger$ and $B = Z_{k'}$ which leads to a well known BCS Hamiltonian [8]:

$$H_{BCS} = \sum_{k\sigma} \xi_k c_{k\sigma}^\dagger c_{k\sigma} - \sum_k \Delta_k^* c_{-k\downarrow} c_{k\uparrow} - \sum_k \Delta_k c_{k\uparrow}^\dagger c_{-k\downarrow}^\dagger \tag{1.2}$$

where $\Delta_k = \frac{1}{N} \sum_{k'} V_{kk'} \langle c_{k,\uparrow} c_{-k,\downarrow} \rangle$ is known as a gap and the constant energy offset is dropped. Looking at this Hamiltonian it is not at all clear how it could be a model of a bulk property which does not have a resistance, but it is indeed there as from it follows the Landau theory the macroscopic theory where it is obvious [33]. Also note that the number of interacting electrons are not conserved in the H_{BCS} Hamiltonian and thus the resulting ground state energy should depend weakly on the number of Cooper pairs Z_k the condensate has.

The ground state of this Hamiltonian is:

$$|\Psi_{BCS}\rangle = \prod_k (u_k + v_k c_{k,\uparrow} c_{-k,\downarrow}) |0\rangle \tag{1.3}$$

where u_k and v_k are determined from minimization of energy $E_{BCS} = \langle \Psi_{BCS} | H_{BCS} | \Psi_{BCS} \rangle$. From this ground state it follows that $\langle Z_k \rangle = \langle \Psi_k | Z_k | \Psi_k \rangle = u_k^* v_k$ in which substituting optimal v_k and u_k and using that $\Delta_k = \frac{1}{N} \sum_{k'} V_{kk'} \langle Z_k \rangle$ we can get the self consistency equation:

$$\Delta_k = -\frac{1}{N} \sum_k V_{kk'} \frac{\Delta_{k'}}{2\sqrt{\xi_{k'}^2 + |\Delta_k|^2}} \tag{1.4}$$

which determines Δ_k from the attractive interaction $V_{kk'}$.

The self consistency equation, although nonlinear, can be solved in simple situations, for instance, in the case of contact potential $V_{kk'} = -V_0$. In such situation the solution is a constant $\Delta_k = \Delta_0$ known as a gap and in case of small interaction $V_0 \rho(E_F) \ll 1$ gives a simple form [31, 32]:

$$\Delta_0 = 2\omega_D \exp\left[-\frac{1}{V_0 \rho(E_F)}\right] \tag{1.5}$$

where ω_D is a cutoff frequency. The singularity at $V_0 \to 0$ is the reason why superconductivity did took so long time for a microscopic theory to be developed as it prevents to be obtained with perturbation theory.

From a Meisenner effect, we know that counter current would be produced upon putting superconductor into a magnetic field, which in contrast to normal metal, never fades away due to zero resistance property. The magnetic field thus is pushed away from the bulk. From the minimized E_{BCS} energy we can evaluate the condensation energy density:

$$e_{BCS} = \frac{E_{BCS} - E_{BCS|\Delta_0 \to 0}}{V} \approx -\frac{1}{2}\frac{N}{V}\rho(E_F)\Delta_0^2 \tag{1.6}$$

which can be overcomed in sufficiently large magnetic fields at which superconductivity vanishes.

The Δ_k, however, in general, is a complex number, but the self consistency equation only determines its modulus [13]. The condensate energy thus is independent of its phase. It's often the case that a global phase does not matter, and we can substitute $\hat{c}_k^\dagger \to e^{i\phi}\hat{c}_k^\dagger$ without any effect as it is canceled in the Hamiltonian as creation and annihilation operators come in pairs. However, when we do the same for the BCS Hamiltonian, the gap gets a phase $\Delta \to e^{-2i\phi}\Delta$ with which we conclude that the gauge symmetry is broken at the moment when the attractive interaction of the electrons condenses the electrons. This fact is quite striking since we know that the phase and charge of each electron are conjugate variables. Thus we can conclude that number of Cooper pairs N in the condensate is a conjugate variable to its phase, and we can write Heisenberg uncertainty relation

$$\Delta\phi\Delta N > 1 \tag{1.7}$$

However, the phase of the bulk is meaningless as a coherent superposition of Cooper pair number states is short-lived due to capacitive effects.

1.2.2. EXCITATIONS AND BDG HAMILTONIAN

In the previous section, we extensively discussed the ground state of superconductivity. It is, however, also essential to discuss excitations. Due to BCS Hamiltonian being bilinear without loss of generality, we can turn back to the Schrodinger picture and consider the wavefunction of a single excitation consisting of two components $|\Psi_k\rangle = (c_k^\dagger, c_{-k})|\Psi_{BCS}\rangle$ one for electron and other for the hole.

The application of the BCS Hamiltonian on this state gives us an equation

$$(H_{BCS} - E_{BCS})|\Psi_k\rangle = \begin{pmatrix} \xi_k & \Delta_k^* \\ \Delta_k & -\xi_k \end{pmatrix} |\Psi_k\rangle \tag{1.8}$$

where the Hamiltonian on the right is known as Bogoliubov de Gennes Hamiltonian or simply H_{BdG} [2]. The H_{BdG} Hamiltonian can be used in the Schrodinger equation to look for dynamics or consider scattering problems. It's also common to regard Δ_k as a fixed quantity of the particular material unaffected in what particular heterostructure or nanostructure the superconductor elements are used.

In the H_{BdG} Hamiltonian, we already see that eigenstates of this Hamiltonian are a superposition of electron and hole states. In precise terms, stationary states can be found by diagonalizing H_{BdG} which corresponds to the superconductor excitations with energies $\pm E_k$ where

$$E_k = \sqrt{\xi_k^2 + \Delta_k^2} \tag{1.9}$$

That means there are no excitations below the gap energy and explains why cooper pairs do not dissipate energy when moving through the condensate.

The two eigenstates of H_{BdG} are $\gamma_k^\dagger|\Psi_{BCS}\rangle = (u_k c_k^\dagger - v_k^* c_{-k})|\Psi_{BCS}\rangle$ corresponding to energy $+E_k$ and $\gamma_{-k}|\Psi_{BCS}\rangle = (v_k c_k^\dagger + u_k^* c_{-k})|\Psi_{BCS}\rangle$ with eigenvalue $-E_k$ where u_k and v_k are coherence factors which we already saw in previous section for BCS. Their square is given as [31, 32]:

$$|u_k|^2 = \frac{1}{2}\left(1 + \frac{\xi_k}{\sqrt{\xi_k^2 + |\Delta_k|^2}}\right) \qquad |v_k|^2 = \frac{1}{2}\left(1 - \frac{\xi_k}{\sqrt{\xi_k^2 + |\Delta_k|^2}}\right) \tag{1.10}$$

At large energies $\xi_k \gg \Delta_k$ the quasiparticles described by γ are holes bellow the Fermi energy and electrons above it. However at low energies $\xi_k \ll \Delta_k$ we get a perfect superposition between holes and electrons.

Of practical interest of this thesis is a superconductor heterostructures thus we need to Fourier transform BdG Hamiltonian and obtain:

$$\hat{H}_{BdG}(\mathbf{x}) = \begin{pmatrix} \hat{H}_0(\mathbf{x}) & \Delta(\mathbf{x}) \\ \Delta(\mathbf{x}) & -\hat{H}_0^*(\mathbf{x}) \end{pmatrix} \tag{1.11}$$

where $\Delta(\mathbf{x})$ is treated as a parameter one specifies and $\hat{H}_0 = -\frac{\hbar}{2m}\nabla^2 - \mu$. That allows modeling easily an interface between superconductor and metal by setting $\Delta(\mathbf{x}) = 0$ for the latter and a constant for a superconductor. The BdG Hamiltonian allows modeling the interface in a similar manner as one models a barrier in one-dimensional Schrodinger mechanics.

1.2.3. Andreev reflection and bound states

The simplest heterostructure and rather crucial for understanding this thesis is the normal-superconductor interface. Consider an electron moving from the normal metal to the superconductor interface. If its energy is lower than that of the gap $\epsilon_k < |\Delta|$, we know that it would not be able to live in the superconductor as there are no excitations in the superconductor below this energy. Thus we could expect it to be reflected, but instead, a hole comes back [34].

The amplitude of the hole can be calculated using a scattering formalism. For simplicity, consider an ideal contact between superconductor and metal in one dimension where negative $x < 0$ corresponds to a normal state and $x > 0$ to a superconducting one. The wavefunction for an incident particle in the normal metal and possible amplitudes in the superconductor are [10]:

$$\psi(x<0) = (e^{ixE/\hbar v_F}, r_A e^{-ixE\hbar v_F}) \qquad \psi(x>0) = (A,B)e^{-x\sqrt{\Delta^2-E^2}/\hbar v_F} \tag{1.12}$$

where r_A is the Andreev reflection amplitude, and A, B coefficients to be found. When one matches these solutions one finds the Andreev reflection amplitude:

$$r_A = e^{i\chi} = e^{-i\phi}\left(\frac{E}{\Delta} - i\frac{\sqrt{\Delta^2 - E^2}}{\Delta}\right) \tag{1.13}$$

The question then remains: where did two electrons go after scattering? As mentioned previously with regards to BCS Hamiltonian, the Cooper pair number in the superconductor does not affect its condensate state and thus is cheap to create. Putting these things together, we see that during Andreev's reflection superconductor, a Cooper pair is created in the superconductor. Similarly, when a hole comes, it is reflected as an electron, and thus the cooper pair leaves the superconductor. That is a nutshell, explains how a superconductor conducts current in a microscopic level.

An interesting situation arises when the normal metal is sandwiched between multiple superconductors. Then the electron gets reflected from one superconductor as a hole and gets back to another one converted back to an electron. Such motion at specific energies E can be cyclic. In general, it corresponds to solving the equation [11]:

$$\det(1 - e^{-2i\arccos(E/|\Delta|)} S e^{i\hat{\phi}} S^* e^{-i\hat{\phi}}) = 0 \tag{1.14}$$

where $\hat{\phi} = \mathrm{diag}(\vec{\phi})$ are superconducting phases of all terminals and S is the scattering matrix connecting all normal and Andreev reflections between terminals. Returning to the case of the sandwiched normal metal between two superconductors solving this condition gives energies of Andreev bound states [10]:

$$E_A = \Delta\sqrt{1 - T\sin^2(\phi/2)} \tag{1.15}$$

where T is a transmission eigenvalue corresponding to a scattering matrix S.

The Andreev-bound states are, in fact, observable. If voltage bias is applied between two superconductors leads the phase difference is moving in time $\dot{\phi} = \frac{2e}{\hbar}V$ to compensate the potential difference of the condensate. Meanwhile, change of phase changes the energy of the system attributed to Andreev bound states $IV = \dot{E}_A$. Combining that gives what is known as supercurrent:

$$I_A = -\frac{2e}{\hbar}\frac{\partial E_A}{\partial\phi} \tag{1.16}$$

which had been studied extensively. In particular, a situation where two superconductors are coupled together with tunnel junction $T \to 0$ gives us a Josephson junction as commonly used [9]:

$$I = I_c \sin(\phi) \tag{1.17}$$

where $I_c = e\Delta T/2\hbar$. Remarkably Andreev bound states coupled to a resonator can also be used to create a qubit possible as the superconducting phase can be coupled coherently with other circuit elements [17, 18].

1.3. QUANTIZATION IN SUPERCONDUCTING CIRCUITS

As discussed previously, the wavefunction of a different number of Cooper pairs in the system can only be superimposed only incoherently due to capacitive effects. That makes the superconducting phase meaningless, so what does it mean to have a phase difference, for instance, in a Josephson junction? Does it really have a quantum origin as the sum of individual electron phases?

For most applications [12, 22, 23], the Josephson junction is a nonlinear circuit element that has a periodic dependence on magnetic flux which goes through it:

$$I = I_c \sin(2\pi\Phi/\Phi_0) \tag{1.18}$$

with $\Phi_0 = 2e/\hbar$ which at small fluxes acts like inductance whereas for a voltage bias one uses a Faraday law $\Phi = dV/dt$. With this nonlinear element, we can understand how to make a high precision voltage standard by converting periodic current drive into Shapiro steps or ultra sensitive magnetic field sensor known as SQUID. The phase thus enters there as a classical variable.

In the 1980s, experiments came up with circuits that could no longer be explained by treating the phase as a classical variable [35]. They considered a current biased Josephson junction whose potential energy can be interpreted in terms of the phase:

$$U(\phi) = \frac{\hbar}{2e}(I_c \cos\phi - I\phi) \tag{1.19}$$

where I is a bias current and $U(\phi)$ is known as a washboard potential. What to notice is that upon the bias current reaches I_c the phase remains fixed, and thus there is no voltage drop on the junction, whereas in opposite case voltage $V = \frac{2e}{\hbar}\dot{\phi}$ can be measured. However, Voss and Webb showed that this classical picture becomes inadequate when the current is close to a critical current showing that the tunneling of the phase can happen [35, 36]. This realization stimulated efforts to create a small Josephson junction operated in a charging regime that could be used as a nonlinear element for the current standard [37–39]. Unfortunately, signatures for such Bloch oscillations are just not usable for metrology [40].

But how could there be tunneling of phase when it is meaningless? The key insight comes from recognizing that if two superconductors are separated with a tunnel barrier, the Cooper pairs tunnel back and forth [13]. Thus, it is possible to have coherence between states in which a total number of electrons is differently partitioned between the two sides. We can consider a relative Cooper pair number to the system $n = N_1 - N_2$ and a relative phase difference $\phi = \phi_1 - \phi_2$ as conjugated variables:

$$[\hat{\phi}, \hat{n}] = 1 \tag{1.20}$$

while the phase on the left superconductor ϕ_1 and on the right ϕ_2 individually remain meaningless.

Using the phase and charge conjugation, we see that we can transform Josephson junction in its conjugated form [36]:

$$H_J = -E_J \cos\hat{\phi} = -\frac{E_J}{2}\sum_n |n\rangle\langle n+1| + |n+1\rangle\langle n| \tag{1.21}$$

which merely describes a tunneling between states differing by a single Cooper pair with strength E_J and is the same for all configurations. That could be so because the condensate depends only weakly on the number of Cooper pairs as long as charge effects are screened. The second Hamiltonian has practical implications, which had enabled to make a Cooper pair box [10, 14, 16].

In practice, the microscopic theory of superconductor is not necessary to understand its behavior in a circuit. It is only necessary to describe superconductors with their macroscopic degrees of freedom, write down the Hamiltonian of a conserved system and say that the phase is of a quantum origin; thus, one can apply 1.20. For example, knowing the energy of the LC oscillator to be $E = Q^2/2C + \Phi^2/2L$ enables us to write the Hamiltonian of such system as:

$$H_{osc}(\phi, n) = \frac{(2e\hat{n})^2}{2C} + \Phi_0^2 \frac{\hat{\phi}^2}{2L} \tag{1.22}$$

which is simply a Hamiltonian of a harmonic oscillator with energy levels $E_k = \hbar\omega(k+1/2)$ with $\omega = 1/\sqrt{LC}$.

In practice, any superconductor system that may depend on the phase is always embedded in a linear circuit. Thus, strictly speaking, the internal phase on the nanostructure is always a quantum variable subject to fluctuations. Thus the Hamiltonian for whole structure becomes:

$$H = H_n(\hat{\phi}) + H_{osc}(\hat{\phi} - \phi^r, \hat{n}) \tag{1.23}$$

where H_n is the Hamiltonian of an arbitrary phase dependent system and H_{osc} for the external linear system, which permits the internal phase to fluctuate around the external phase ϕ^r.

1.3.1. IMAGINARY TIME FORMALISM

An alternative formulation of quantum mechanics is a path integral formalism that gives the advantage to analyze systems with large degrees of freedom and obtain an effective description and particularly useful to analyze the system's ground state [41].

To see why let's consider a generic Hamiltonian:

$$H = \frac{\hat{Q}^2}{2C} + V(\hat{\phi}) \tag{1.24}$$

where $\hat{Q} = 2e\hat{n}$. As it is time independent we know that an arbitrary wavefunction evolves in time as $|\psi(t)\rangle = e^{-iHt/\hbar}|\psi(0)\rangle$. In path integral formulation the unitary operator is projected to coordinate representation and considers a function which is called a propagator:

$$K(0, t, \phi, \phi') = \langle\phi| e^{-iHt/\hbar} |\phi'\rangle \tag{1.25}$$

Dirac noticed that the propagator of a free particle is proportional to an exponent $K(0, t, \phi, \phi') \propto e^{-iS_c(\phi, \phi', t)/\hbar}$ where S_c is a classical action of a free particle which for our variables is $S_c = \frac{C\Phi_0^2}{2} \int \dot{\phi}^2 dt$ [42]. Feynman further saw that it is possible to decompose the potential into straight segments and calculate the final propagator as a product which gives a remarkably simple result [43]:

$$K(0, t, \phi, \phi') = \int D\phi e^{iS[\phi]/\hbar} \tag{1.26}$$

where the brackets denote that the action is evaluated at a particular point of the phase and integration is over each phase at each point separately. Alternatively, one can look at the integral as integration over all possible trajectories $\phi(t)$ satisfying boundary conditions, and hence it is known as a path integral. The action $S[\phi]$ is given as:

$$S[\phi] = \int_0^t \left(\frac{C\Phi_0^2}{2}\dot{\phi}^2 - V(\phi) \right) dt \tag{1.27}$$

and encompasses quite a general class of problems as the potential can be arbitrary. Also, a number of degrees of freedom can be arbitrary, which can be easily restored, and so one can also consider a generic Lagrangians.

A great part of application of path integrals have found in computation of partition function and density matrix. The density matrix at equilibrium enables to compute operator averages $\langle \hat{Q} \rangle = \mathrm{Tr}[Qe^{-\beta\hat{H}/\hbar}]$ where $\beta = \hbar/k_B T$ and in coordinate representation is given as:

$$\rho(\phi,\phi') = \frac{1}{Z}\langle \phi | e^{-\beta H/\hbar} | \phi' \rangle \tag{1.28}$$

where $Z = \int \rho(\phi,\phi) d\phi$ is a normalization factor also known as microcanonical partition function. The form of the density matrix is in fact very similar to how we defined the propagator. In fact if we evaluate propagator at imaginary time $t = -i\hbar\beta$ we get an important identity $K(0,-i\hbar\beta,\phi,\phi') = \langle \phi | e^{-\beta H/\hbar} | \phi' \rangle = Z\rho(\phi,\phi')$. On the other hand evaluating propagator at imaginary time with path integral gives us:

$$\rho(\phi,\phi') = \frac{1}{Z}\int D\phi e^{-\beta S_E[\phi]/\hbar} \tag{1.29}$$

where S_E is:

$$S_E[\phi] = \int_0^\beta \left(\frac{C\Phi_0^2}{2}\dot{\phi}^2 + V(\phi) \right) d\tau \tag{1.30}$$

is known as Euclidean action which one obtains from normal action by inverting the potential. The minus sign in the exponent makes it easy to see that the dominant contribution comes from the trajectory which minimizes Euclidean action and thus in practice can be expanded up to the second order and evaluated as Gaussian integrals.

As an example let's consider the LC oscillator. The Euclidean action of it is $S_E[\phi] = \int_0^\beta \left(\frac{C\Phi_0^2}{2}\dot{\phi}^2 + \frac{\Phi_0^2}{2L}\phi^2 \right) d\tau$. We can assume that the phase is periodic $\phi(\tau) = \phi(\tau + \hbar\beta)$ and thus we can express it in Fourier series $\phi(\tau) = \frac{1}{\beta}\sum_n \phi_m e^{-i\nu_n\tau}$ with $\nu_n = 2n\pi/\beta$ known as Matsubara frequencies and insert that in the Euclidean action which gives:

$$S_{ext} = \frac{\beta C\Phi_0^2}{2}\sum_n \phi_n\phi_{-n}\left(\nu_n^2 + \frac{1}{LC} \right) \tag{1.31}$$

This form of action allows to calculate a correlator for different modes:

$$\langle \phi_m\phi_{-m} \rangle = \frac{\int D\phi \phi_m\phi_{-m} e^{-\beta S_{ext}/\hbar}}{\int D\phi e^{-\beta S_{ext}/\hbar}} = \frac{\hbar}{\beta C\Phi_0^2}\frac{1}{\nu_m^2 + 1/LC} \tag{1.32}$$

where other cross correlators are zero. This correlator shows that the system which is embeded in a linear circuit would only experience quantum fluctuations with frequencies $\nu_n \ll 1/\sqrt{LC}$. It is particularly useful for renormalization procedure for tracing out high frequency modes to get an effective action for low energy.

1.4. TOPOLOGY

In some circumstances, the bands in a bandstructure cross. These crossings can be topologically protected, meaning that perturbations of the system would not make them disappear. Thus, they have been praised with words like topological protection. It's present in topological materials, and the crossings themselves have gained a name of Weyl points [44]. The Weyl part is merely to say that they cross without curvature; thus, at the crossing point, the quasiparticles like electrons in the Brillion zone do not have a mass.

Nevertheless of simplicity, the Weyl points have attracted considerable interest [24]. Topological insulators are characteristic with nonconducting bulk, and only on the surface, the bands cross [45]. Another class of materials is semimetals, where valence and conduction bands touch at the Fermi level. Depending on whether the bands are nondegenerate or doubly degenerate, topological material is called a topological Weyl semimetal or a topological Dirac semimetal [46].

One of the exciting properties of topological materials is that spin and momentum are locked together [47]. Thus a current flowing in one direction has a defined spin of its electrons. In addition, the electrons in a Weyl semimetal have exceptionally high mobilities. For Weyl semimetals, the main measurement is that of Fermi Arc, which connects the pair of Weyl nodes with opposite chiralities on the material surface, which can be measured with spectroscopy [48, 49].

In its essence, properties of topological materials are given by their bandstructure in the Brillion zone. On the other hand, we saw that superconductor heterostructure properties are similarly determined by Andreev bound state spectrum in superconducting space. Since both quasimomentum and superconducting phase spaces are periodic, it should be possible to simulate properties of topological materials with superconductor heterostructures if one manages to make a Weyl point in Andreev bound state spectrum.

Recently a new system where Weyl points are hosted was proposed using the multiterminal superconducting junction [50]. It was realized that if more than four terminals surround a normal scattering region, then it may be feasible to find Andreev bound state crossing in three (or more) superconductivity phase space (in contrast to a Brillion zone) and would appear in pairs as in Weyl semimetal. The Weyl singularity in superconductivity phase space opens new avenues for exploring its behavior in the superconductor circuits.

In contrast to momentum can be coupled with other circuit elements allowing to explore the effect of quantum fluctuations. To simplify the description we shall always assume that the superconducting phases are tuned to the crossing. Thus, for a four-terminal setup, we can linearize one of the Weyl points and considers the effect of the Weyl Hamiltonian, which can be written as:

$$H_W = \frac{2e}{\hbar} \sum_n I_n \hat{\phi}_n \sigma_n \tag{1.33}$$

where I_n are currents according to the current formula for Andreev bound states. This Hamiltonian form is commonly known as spin-orbit coupling if we call $\hat{\phi}_n$ as momentum.

1.5. HOLONOMIC COMPUTATION

The Schrodinger equation determines all dynamics for a state evolution in a Hilbert space. On the contrary, the measurement, a fundamental concept in quantum mechanics, is independent of a phase and is formally defined for a pure state which forms a projective Hilbert space. It has been recognized that a state which forms a loop in projective Hilbert space by time-dependent evolution of the Schrodinger equation would gain a phase factor in the Hilbert space. This phase factor can be separated into two parts. A dynamical phase is dependent on the energy of the state and the time it takes to evolve the loop. A geometric phase that depends solely on the loop it makes in the projective Hilbert space [51].

The geometric phase is an attractive building block for a quantum computer. For instance, there are setups where the dynamical phase can be neglected. When the loop is executed fast in a controlled manner with a degenerate base subspace, it has been actively studied in nonadiabatic geometric quantum manipulation [52, 53]. Alternatively, the loop can be executed adiabatically in a degenerate manifold where the projective Hilbert space matches the degenerate subspace of a parameterized Hamiltonian. The resulting geometric phase then reduces to a holonomic phase and is a basis of actively studied holonomic quantum manipulation [54–57].

In a realistic scenario a geometric phase is associated to a periodic time dependent Hamiltonian $H(\tau) = H(0)$ which has a cyclic states $|\psi(\tau)\rangle = e^{i\phi}|\psi(0)\rangle$. As shown this phase consists of two parts $\phi = \gamma + \beta$ - a dynamical and geometric phase. A dynamical phase is due to Hamiltonian $\gamma = -\frac{1}{\hbar}\int_0^\tau \langle\psi(t)|H(t)|\psi(t)\rangle dt$ which is execution time dependent. The geometric phase on the other hand depends only on the path it makes in the projective Hilbert space:

$$\beta = \int_0^\tau \langle\tilde{\psi}(t)|i\frac{d}{dt}|\tilde{\psi}(t)\rangle dt \tag{1.34}$$

where $|\tilde{\psi}(t)\rangle$ are the states from the projective Hilbert space so that $|\tilde{\psi}(\tau)\rangle = |\tilde{\psi}(0)\rangle = |\psi(0)\rangle$.

Experimentally the geometric phase has been used to construct quantum gates in a three-level system consisting of two degenerate levels with an excited state $\{|0\rangle, |e\rangle, |1\rangle\}$ [52]. The idea here is that the loops are formed in the projective Hilbert space within these three levels where one point of the loop is within the degenerate subspace $\{|0\rangle, |1\rangle\}$. Thus changing the loop, one can change the composition of cyclic states and the acquired phase enabling to implement all manipulations for a state encoded in degenerate subspace.

Alternatively, a loop in projective Hilbert space can be made by changing the parameters of the Hamiltonian adiabatically. For a single level, the cyclic state six an eigenstate of the Hamiltonian, and the corresponding geometric phase in such case is called a Berry phase [55]. Degenerate systems are fascinating as we can expect that the different manifold trajectories with fixed endpoints associate a particular holonomic phase and the state to which it applies. Thus each trajectory represents a unitary operator, which is called a holonomic transformation [54]. The formula, therefore, generalizes to

$$U = \mathscr{P} e^{-i \int_0^{\tau} \vec{M}(\vec{x}) \cdot d\vec{l}} \tag{1.35}$$

where $M^k_{ml}(t) = i \langle \tilde{\psi}_m(\vec{x}) | \partial_k | \tilde{\psi}_l(\vec{x}) \rangle$ is a gauge potential of the degenerate manifold and $\mathscr{P}$ is path ordering [58].

The gauge potential can be Abelian and non-Abelian. In the case of the Abelian connection, a set of unitary operators representing all trajectories with fixed endpoints can be diagonalized simultaneously. Another way to paraphrasing the formula is that the Abelian connection is equivalent to a property that the gauge potential is diagonalizable for all manifold points. If it is not true, the gauge potential is non-Abelian. A non-Abelian connection is fascinating as it allows holonomic transformations from different trajectories to realize a universal set of quantum gates. However, the experimental implementation of them is difficult due to nonadiabatic corrections.

A particular example is indistinguishable two-dimensional anyon systems which provide a connection with a vanishing curvature [59]. In such systems, holonomic transformations are the same for a set of trajectories from the same homotopy class specified by winding angle around two anyons alone. Topological quantum computation recognizes that non-Abelian anyons provide a way to implement universal quantum computations moving anyons around each other in closed paths, a procedure called braiding is robust against trajectory fluctuations and thus, in theory, allows to implement a gate with exceptional fidelity [25, 60] . That has raised interest in non-Abelian anyonic excitations such as Majorana bound states [61, 62] and in fractional quantum Hall effect [63, 64] where anyons can be identified at the beginning and the end of computations.

1.6. PHASE SLIPS

In one dimension, fundamental theorems predict that a long-range superconductivity order is destroyed due to fluctuations of the order parameter [65, 66]. In particular, a one-dimensional superconductor wire could overcome the condensation energy either with thermal or quantum fluctuations, putting the gap to zero and thus effectively splitting the wire in half. On the other hand, we know that the phase is not uniquely defined and leaves the system unchanged upon $\phi \to \phi + 2\pi n$. We also saw that the absolute phase for an isolated superconductor itself is meaningless as coherence between Cooper pair states is short-lived. Thus, is it possible that when the order parameter is restored, the phase had locally slipped by 2π?

The 2nd Josephson relation predicts if such a process happens, it creates a voltage pulse $\delta V = \Phi_0 \dot{\phi}$ between the ends of the wire. In the absence of current bias, the phase slips $\pm 2\pi$ happen with equal frequency, and thus there is no measurable voltage bias. But the situation changes when current bias is applied as it makes a phase gradient $I \propto \nabla \phi$, breaking the symmetry and making one side event happen more frequently than another one. On average, this produces a voltage that we can interpret as resistance [36].

The frequency of the phase slips depends on the effective potential of the barrier, which needs to be overcome. We can make an estimate for the barrier from the condensation energy density 1.6 by multiplying that with a cross-section of the wire S and superconductor coherence length ξ, which gives us:

$$U \approx \frac{\nu \Delta_0(T)^2}{2} S\xi(T) \tag{1.36}$$

where the gap and coherence length is temperature dependent and $\nu = N\rho(E_F)/V$ is an electron density in a normal state at Fermi energy. According to statistical mechanics, the frequency for thermally activated phase slips and thus resistance is $R \propto e^{-U/k_B T}$. The resistance and particular temperature dependence had been confirmed close to the superconductor's critical temperature, supporting the presence of thermal phase slips [67].

At very cold temperatures, the critical thermal fluctuations do freeze out; however, some finite resistance persists [68]. One possibility is that the quantum phase tunnels through the barrier U instead. A typical timescale from Heisenberg uncertainty relations for a fluctuation on the superconducting wire could be around $\tau = \hbar/\Delta_0$. Thus we may estimate the resistance to be $U \propto e^{-\tau U/\hbar}$. However, such resistance measurements are not conclusive as each phase slip releases an energy $I\Phi_0$ and thus heats up the sample.

Quantum mechanics offers some more flexibility in the aspect and enables to test coherence between the presence and absence of quantum phase slip. One way to observe such coherence is by embedding a thin superconductor wire in a superconductor loop subjected to an external magnetic field [28, 36]. In such a system, the energy is described by

$$E_N = (\Phi_{ext} - M\Phi_0)^2/2L \tag{1.37}$$

where L is the inductance of the loop and M is the phase winding number. The states determined by M known as fluxoid states differ by the persistent loop current. For instance between adjacent states $|\rangle$ and $|M+1\rangle$ the current difference is $\Phi_0/2L$.

An interesting situation occurs when neighboring fluxoid states cross and from a degeneracy $\Phi_{ext} = (2M+1)\Phi_0/2$. A quantum phase slip can increase the fluxoid number from M with a tunneling matrix element $|M+1\rangle\langle M|$ in the Hamiltonian. This tunneling matrix element is independent of fluxoid number and is symmetric; thus, if a coherent quantum phase slip takes place, there should be a tunneling matrix element between the fluxoid states coupling them, which can be expressed as

$$H_S = \frac{E_S}{2} \sum_M |M+1\rangle\langle M| + |M\rangle\langle M+1| \tag{1.38}$$

where E_S is a phase slip strength. Such tunneling matrix element lifts the degeneracy of adjacent fluxoid states observed in spectroscopy measurements confirms the presence of coherent quantum phase slip in a thin superconductor wire [27, 69, 70].

This Hamiltonian is equivalent to the Hamiltonian for Josephson junction 1.21 where a number of Cooper pairs is interchanged with fluxoid number. We know that the fluxoid number is determined by the number of windings of the phase; thus, it's conjugate to charge as $[\hat{Q}, \hat{M}] = 2e$. Therefore transforming the phase slip Hamiltonian to a charge representation using formula $e^{2\pi i \hat{Q}/2e} = \sum_M |M-1\rangle\langle M|$ we get a phase slip Hamiltonian:

$$H_S = E_S \cos(2\pi \hat{Q}/2e) \tag{1.39}$$

which is the same as for Josephson junction, only phase interchanged with charge and thus in analogy, a thin superconductor wire is called a phase slip junction.

The similarity is, in fact, not only approximate but exact duality, meaning that any circuit consisting of Josephson junctions has an equivalent circuit with phase slip junctions where $\hat{Q} \to \hat{\phi}$ and $I \to V$ [29]. This has driven interest in metrology in implementing the current standard in a dual circuit as done with Josephson junctions for voltage standard [71]. However, Coulomb blockade measurements of the phase slip junction have not been conclusive as those can be interpreted with granularity and thus can be interpreted to originate from a small Josephson junction in the wire. Only slight signatures of Shapiro steps had been observed, which are useless for metrology [30].

1.7. QUANTUM CIRCUIT THEORY

The BdG Hamiltonian, as we saw previously, could give us all the necessary information for understanding the quantum system and allows us to understand, for instance, Andreev's bound states of a normal metal. However, it is not always possible to solve it and depends on the system's geometry, which narrows understanding of a particular setup. However, it is possible to approximate the Andreev-bound states with continuum and use the Green function method and associated quantum circuit theory in many situations [10, 72]. The latter offers an excellent alternative for understanding quantum transport in a wide variety of systems without being fixed to a specific geometry.

To start with, we need to introduce Green functions. In general, different choices of Green functions correspond to different physical theories and situations. In particular for quantum circuit theory with superconductivity is convenient to parameterize the Green functions with a following Keldysh space (τ_1, τ_2, τ_3) structure:

$$G = \begin{pmatrix} R & K \\ 0 & A \end{pmatrix} \tag{1.40}$$

where R, A, K are 2×2 matrices in Nambu space (η_1, η_2, η_3) known as retarded, advanced and Keldysh Green functions [73, 74]. The Green functions, in general, are normalized $G^2 = 1$ and from the chosen structure, it follows that $R^2, A^2 = 1$ and $RK - AK = 0$. It is also known that advanced and retarded Green functions are related to each other $R(\epsilon) = -\eta_3 A(-\epsilon)\eta_3$ thus one gives another.

In case we are in bulk and know that it would not be perturbed in any meaningful way due to a small nanostructure it is connected to, we can set the Green function for an arbitrary superconductor to be:

$$\begin{pmatrix} R \\ A \end{pmatrix} = \frac{\pm 1}{\sqrt{\epsilon^2 - |\Delta|^2}} \begin{bmatrix} \epsilon & \Delta^* \\ -\Delta & -\epsilon \end{bmatrix} \qquad K = \begin{bmatrix} \tanh \frac{\epsilon + eV}{2k_B T} & 0 \\ 0 & -\tanh \frac{\epsilon - eV}{2k_B T} \end{bmatrix} \tag{1.41}$$

With these Green functions, we can model a superconductor state with arbitrary phase ϕ and also a normal metal by setting the gap $\Delta = 0$. And lastly, with the Keldysh part, we can model the effects of temperature and set the voltage bias V.

The retarded (and advanced) Green function in fact does have a physical meaning for providing the density of states [10]:

$$\nu(\epsilon)/\nu_0 = \mathrm{ReTr}\{\eta_3 R\} \tag{1.42}$$

where ν_0 is a density of states in a normal state and the trace explicitly is $\mathrm{Tr}[Q] = \frac{1}{\hbar}\sum_{ij}\int Q_{ii,jj}(\epsilon,\epsilon)d\epsilon$ with summation over Keldysh and Nambu space. For example, plugging in a retarded Green function given in 1.41 gives us expected BCS density of states [31, 32]:

$$\nu(\epsilon)/\nu_0 = \Theta(\epsilon^2 - |\Delta|^2)\frac{|\epsilon|}{\sqrt{\epsilon^2 - |\Delta|^2}}. \tag{1.43}$$

In general we don't know the Green functions of small islands and we need to solve for them. One way to do that is by discretizing the system into nodes for unknown Green functions and connectors through which a matrix current flows [10, 72]. For a single connector the matrix current is given as:

$$\hat{I} = G_Q \sum_p \frac{T_p(\hat{G}_1\hat{G}_2 - \hat{G}_2\hat{G}_1)}{2 + \frac{T_p}{2}(\hat{G}_1\hat{G}_2 + \hat{G}_2\hat{G}_1 - 2)} \tag{1.44}$$

where the sum is over transverse mode with transmission eigenvalues T_p, quantum conductance G_Q, and $G_{1,2}$ are Green functions at the end of the nodes. The matrix current is associated to a real electric current which for a choose parametrization of the Green function 1.40 is given as

$$I_{el} = \frac{1}{4e}\int d\epsilon \mathrm{Tr}[\eta_3\tau_1\hat{I}] \tag{1.45}$$

where τ_1 selects nondiagonal matrix current element in the Keldysh space.

In the case of multiple connectors with intermediate nodes, the Green functions at unknown nodes are determined from the matrix current conservation at each node: $\sum_i \hat{I}_{ij} = 0$ which automatically also conserves electric current. An important thing to notice is that because of the chosen form of the Green functions, the diagonal blocks decouple, and we can solve equations in terms of $\hat{R}$ and $\hat{A}$ separately.

The equations (1), (2) enable to reformulate the problem of finding the Green function as minimization of a connector action given as:

$$S = \sum_{ij}\mathrm{Tr}[\mathscr{F}_{ij}(G_iG_j + G_jG_i)] \tag{1.46}$$

where $\mathscr{F}$ is a connector characterizing function:

$$\mathscr{F} = \sum_p \log(1 + \frac{T_p}{2}(x-1)) \tag{1.47}$$

This connector characterizing function for ballistic connector is $\mathscr{F}_B(x) = \frac{G_B}{G_Q}\log\frac{1+x}{2}$ for tunnel junction $\mathscr{F}_T(x) = -\frac{G_T}{2G_Q}(1-x)$ and for diffusive connector $\mathscr{F}_D(x) = \frac{G_D}{8G_Q}\arccos^2(x)$.

Because the Keldysh space structure 1.40 retarded and advanced Green functions decouples and we can minimize the action separately by substituting $G \to R$. Furthermore to relieve us from daunting matrix products we can express $\hat{R} = \vec{s}\cdot\vec{\eta}$ where $\vec{s}$ is called a spectral vector which at the north pole $s_3 = 1$ represents a normal state and $s_3 = 0$ a superconducting one. With it the connector network action reduces into a simpler problem:

$$S = \sum_{ij}\mathrm{Tr}[\mathscr{F}(\vec{s}_i\cdot\vec{s}_j)] \tag{1.48}$$

with $|\vec{s}_i| = 1$. In particular, when terminal phases are time-independent, the operators s_i, become diagonal in energy representation. Thus the formula can be interpreted as minimization of elastic energy of a given network on a hemisphere held in place with external nodes (bulk terminals).

In case of low energy limit, the formula for the electric current 1.45 enables us to calculate conductance $I_{el} = GV$ with the following formula:

$$G_{ij} = \frac{\partial^2 \mathscr{F}}{\partial x^2}(\vec{s}_i \cdot \vec{s}_j) \tag{1.49}$$

In particular, we can recover Landauer conductance by setting both vectors at the north pole thus $\vec{s}_i \cdot \vec{s}_j = 1$ and also Andreev conductance if one is in the superconducting state $\vec{s}_i \cdot \vec{s}_j = 0$ [10, 34].

1.8. STRUCTURE OF THE THESIS

CHAPTER 2: WEYL DISKS

In multiterminal superconducting nanostructures, a Weyl point may be present in the Andreev-bound state spectrum. This offers new opportunities for new physical phenomena as the superconducting phase can be considered a quantum variable. To explore the situation, we consider the Weyl point at vicinity coupled with an external linear circuit forming a soft constraint for the internal phase in the nanostructure with an external reservoir phase. With a quasiclassical approach, we show that the Weyl point spectrum in the presence of quantum fluctuations becomes flattened in two of the three directions forming what we call a Weyl disk. We support this theoretical observation numerically and show that this prediction is generic and also valid for Coulomb-type interactions, which models a bound state of Weyl exciton and a massive hole.

CHAPTER 3: HOLONOMIC QUANTUM MANIPULATION IN THE WEYL DISK

As proposed in the previous chapter, the presence of two-dimension degenerate subspace Weyl disk begs to ask whether it is applicable for quantum computation. In this chapter, we investigate the possible manipulations at the ground state of the Weyl disk system, considering the properties of wavefunctions of this manifold. Using quasiclassical approximation, we show that we can predict the properties of the wave function it's localization and spin. That enables us to evaluate the connection of the Weyl disk manifold, which shows that Abelian holonomic transformations are possible. We propose a possible quantum manipulation where initialization and readout are being done outside the disk and discuss nonadiabatic corrections. Lastly, we show a realization of a swap gate and evaluate its fidelity as a function of execution time by numerically integrating the time-dependent Schrodinger equation.

CHAPTER 4: DRASTIC EFFECT OF WEAK INTERACTION NEAR SPECIAL POINTS

A generic semiclassical nanostructure connected to multiple superconducting terminals hosts a quasi-continuous spectrum of Andreev-bound states. Recently, it has been discovered that depending on the point in the superconducting phases space, the quasi-continuous spectrum may be gapless or gaped, for which a topological number can be associated. A particular fascinating situation occurs at a special point when all superconducting phases are set to $0, \pi$. In such a situation, the two topologically distinct gaped phases are separated with infinitely narrow gapless phase. This chapter investigates the effect of quantum fluctuations of superconducting phases at the vicinity of a special point when the system is embedded in a linear circuit. We focus on a weak interaction limit and derive a universal generic action using a quantum circuit theory for the special point, enabling us to investigate renormalization effects. Our results indicate a drastic change of phase diagram, which squeezes the gapless region, suggesting that the two gaped phases are always in direct contact at the special point. In addition, we see an exponentially small low energy scale at the gapless phase, which suggests a breakdown of the perturbation theory for arbitrary weak interaction hinting at a drastic change of the Andreev spectrum. A similar phenomenon where arbitrary weak interaction qualitatively changes the fermionic spectrum is superconductivity.

CHAPTER 5: SYNCHRONIZATION OF BLOCH OSCILLATIONS BY GATE VOLTAGE MODULATION

Another type of superconductor quantum phase effect is phase slips. The concept of coherent quantum phase slips is well-established. However, at this moment, no conclusive experimental observation of quantized plateaux has been presented. This chapter proposes a novel setup consisting of two-phase slips in series modulated with a gate voltage. This setup is advantageous as with relatively small a.c. modulation gives rise to a pronounced plateau of quantized current of the width of the order of the Coulomb blockade threshold. We investigate the setup is strong, weak, and intermediate coupling regime defined by a ratio of gate capacitance and the effective capacitance of phase-slip junctions. For intermediate coupling, we find the rise of fractional steps and evaluate its width. Finally, we consider finite temperature effects on the plateau width and give an empirical scaling applicable for all integer steps. In contrast, no such generic scaling exists for fractional steps, but we see that a higher denominator makes the step significantly less resistant to smoothening.

REFERENCES

[1] H. K. Onnes, *The disappearance of the resistivity of mercury*, Comm. Leiden (1911).

[2] P. G. de Gennes, *Superconductivity of Metals and Alloys* (W. A. Benjamin, New York, 1966).

[3] M. Tinkham, *Introduction to superconductivity* (McGraw-Hill, New York, 1975).

[4] V. Ginzburg and L. Landau, Zh. Eksp. Teor. Fiz **20**, 1064 (1950).

[5] P. Anderson, *Notes on theory of magnetism* (Tokyo, 1954).

[6] P. W. Anderson, *Considerations on the flow of superfluid helium,* (1984).

[7] P. Anderson, *Basic notions of condensed matter physics* (Addison-Wesley, Reading, Massachusetts, 1984).

[8] J. Bardeen, L. N. Cooper, and J. R. Schrieffer, *Theory of superconductivity*, Physical Review **108**, 1175 (1957).

[9] B. D. Josephson, *Possible new effects in superconductive tunnelling*, Physics Letters **1**, 251 (1962).

[10] Y. V. Nazarov and Y. M. Blanter, *Quantum Transport* (Cambridge University Press, Cambridge, 2009).

[11] C. W. J. Beenakker, *Universal limit of critical-current fluctuations in mesoscopic josephson junctions*, Physical Review Letters **67**, 3836 (1991).

[12] J. Clarke, *Squid fundamentals*, in *SQUID Sensors: Fundamentals, Fabrication and Applications* (Springer Netherlands, 1996) pp. 1–62.

[13] P. Anderson, *Special effects in superconductivity*, in *Lectures on the Many-body Problems*, edited by E. R. Caianiello (Academic, New York, 1964) pp. 113–135.

[14] A. Blais, A. L. Grimsmo, S. M. Girvin, and A. Wallraff, *Circuit quantum electrodynamics*, Rev. Mod. Phys. **93**, 025005 (2021).

[15] M. H. Devoret and R. J. Schoelkopf, *Superconducting circuits for quantum information: An outlook*, Science **339**, 1169 (2013).

[16] A. A. Houck, J. Koch, M. H. Devoret, S. M. Girvin, and R. J. Schoelkopf, *Life after charge noise: recent results with transmon qubits*, Quantum Information Processing **8**, 105 (2009).

[17] A. Zazunov, V. S. Shumeiko, E. N. Bratus', J. Lantz, and G. Wendin, *Andreev level qubit*, Physical Review Letters **90**, 087003 (2003).

[18] C. Janvier, L. Tosi, L. Bretheau, Ç. Ö. Girit, M. Stern, P. Bertet, P. Joyez, D. Vion, D. Esteve, M. F. Goffman, H. Pothier, and C. Urbina, *Coherent manipulation of andreev states in superconducting atomic contacts*, Science **349**, 1199 (2015).

[19] M. Alam, M. Abido, and I. El-Amin, *Fault current limiters in power systems: A comprehensive review*, Energies **11**, 1025 (2018).

[20] D. Twerenbold, *Cryogenic particle detectors*, Reports on Progress in Physics **59**, 349 (1996).

[21] G. N. Gol'tsman, O. Okunev, G. Chulkova, A. Lipatov, A. Semenov, K. Smirnov, B. Voronov, A. Dzardanov, C. Williams, and R. Sobolewski, *Picosecond superconducting single-photon optical detector*, Applied Physics Letters **79**, 705 (2001).

[22] S. Shapiro, *Josephson currents in superconducting tunneling: The effect of microwaves and other observations*, Physical Review Letters **11**, 80 (1963).

[23] F. Lloyd, C. Hamilton, J. Beall, D. Go, R. Ono, and R. Harris, *A josephson array voltage standard at 10 v*, IEEE Electron Device Letters **8**, 449 (1987).

[24] P. B. Pal, *Dirac, majorana, and weyl fermions*, Amer. J. Phys. **79**, 485 (2011).

[25] A. Y. Kitaev, *Fault-tolerant quantum computation by anyons*, Annals of Physics **303**, 2 (2003).

[26] J. D. Bommer, H. Zhang, Önder Gül, B. Nijholt, M. Wimmer, F. N. Rybakov, J. Garaud, D. Rodic, E. Babaev, M. Troyer, D. Car, S. R. Plissard, E. P. Bakkers, K. Watanabe, T. Taniguchi, and L. P. Kouwenhoven, *Spin-orbit protection of induced superconductivity in majorana nanowires*, Physical Review Letters **122**, 187702 (2019).

[27] O. V. Astafiev, L. B. Ioffe, S. Kafanov, Y. A. Pashkin, K. Y. Arutyunov, D. Shahar, O. Cohen, and J. S. Tsai, *Coherent quantum phase slip*, Nature **484**, 355 (2012).

[28] J. Mooij and C. Harmans, *Phase-slip flux qubits*, New Journal of Physics **7**, 219 (2005).

[29] J. E. Mooij and Y. V. Nazarov, *Superconducting nanowires as quantum phase-slip junctions*, Nature Physics **2**, 169 (2006).

[30] Z. M. Wang, J. S. Lehtinen, and K. Y. Arutyunov, *Towards quantum phase slip based standard of electric current*, Applied Physics Letters **114**, 242601 (2019).

[31] Y. V. Nazarov and J. Danon, *Advanced Quantum Mechanics* (Cambridge University Press, 2013).

[32] C. Timm, *Theory of Superconductivity* (2016).

[33] L. Gorkov, *Microscopic derivation of the ginzburg-landau equations in the theory of super-conductivity*, Sov. Phys. JETP , 1364 (1959).

[34] A. F. Andreev, *The thermal conductivity of the intermediate state in superconductors*, Sov. Phys. JETP **19**, 1228 (1964).

[35] R. F. Voss and R. A. Webb, *Macroscopic quantum tunneling in 1-μm nb josephson junctions*, Physical Review Letters **47**, 265 (1981).

[36] A. Hriscu, *Theoretical Proposals of Quantum Phase-slip Devices*, Ph.D. thesis (2012).

[37] L. Kuzmin and D. Haviland, *Observation of the bloch oscillations in an ultrasmall josephson junction*, Physical Review Letters **67**, 2890 (1991).

[38] U. Geigenmüller and G. Schön, *Single electron effects and bloch oscillations in normal and superconducting tunnel junctions*, Physica B: Condensed Matter **152**, 186 (1988).

[39] D. V. Averin, A. B. Zorin, and K. K. Likharev, *Bloch oscillations in small josephson junctions*, Soviet Physics - JETP **61**, 407 (1985).

[40] G. Schön and A. Zaikin, *Quantum coherent effects, phase transitions, and the dissipative dynamics of ultra small tunnel junctions*, Physics Reports **198**, 237 (1990).

[41] M. Hilke, *Introduction to path integrals*, (2006).

[42] P. Dirac, *The lagrangian in quantum mechanics*, Physikalische Zeitschrift der Sowjetunion **3**, 64 (1933).

[43] L. M. Brown, *Feynman's Thesis: A New Approach to Quantum Theory* (World Scientific, 2005).

[44] H. Weyl, *Electron und Gravitation*, Z. Phys. **56**, 330 (1929).

[45] M. Z. Hasan and C. L. Kane, *Colloquium: Topological insulators*, Reviews of Modern Physics **82**, 3045 (2010).

[46] B. Yau and C. Felser, *Topological materials: Weyl semimetals*, Annu. Rev. Condensed Matter Phys. **2017.8**, 337 (2017).

[47] P. Li, W. Wu, Y. Wen, C. Zhang, J. Zhang, S. Zhang, Z. Yu, S. A. Yang, A. Manchon, and X. xiang Zhang, *Spin-momentum locking and spin-orbit torques in magnetic nano-heterojunctions composed of weyl semimetal WTe2*, Nature Communications **9** (2018), 10.1038/s41467-018-06518-1.

[48] S. Jia, S.-Y. Xu, and M. Z. Hasan, *Weyl semimetals, fermi arcs and chiral anomalies*, Nature Materials **15**, 1140 (2016).

[49] M. Z. Hasan *et al.*, *Discovery of a Weyl fermion semimetal and topological Fermi arcs*, Science **349**, 613 (2015).

[50] R.-P. Riwar, M. Houzet, J. S. Meyer, and Y. V. Nazarov, *Multi-terminal josephson junctions as topological matter*, Nature Communications **7**, 11167 (2016).

[51] Y. Aharonov and J. Anandan, *Phase change during a cyclic quantum evolution*, Physical Review Letters **58**, 1593 (1987).

[52] A. A. A. Jr, J. M. Fink, K. Juliusson, M. Pechal, S. Berger, A. Wallraff, and S. Filipp, *Experimental realization of non-abelian non-adiabatic geometric gates*, Nature **496**, 482 (2013).

[53] E. Sjöqvist, D. M. Tong, L. M. Andersson, B. Hessmo, M. Johansson, and K. Singh, *Non-adiabatic holonomic quantum computation*, New Journal of Physics **14**, 103035 (2012).

[54] P. Zanardi and M. Rasetti, *Holonomic quantum computation*, Physics Letters A **264**, 94 (1999).

[55] M. V. Berry, *Quantal phase factors accompanying adiabatic changes*, Proceedings of the Royal Society of London. A. Mathematical and Physical Sciences **392**, 45 (1984).

[56] J. Pachos, P. Zanardi, and M. Rasetti, *Non-Abelian Berry connections for quantum computation*, Phys. Rev. A **61**, 010305 (1999).

[57] D. J. Moore, *Berry phases and rabi oscillations*, Quantum Optics: Journal of the European Optical Society Part B **4**, 123 (1992).

[58] F. Wilczek and A. Zee, *Appearance of gauge structure in simple dynamical systems*, Physical Review Letters **52**, 2111 (1984).

[59] J. M. Leinaas and J. Myrheim, *On the theory of identical particles*, Il Nuovo Cimento B Series 11 **37**, 1 (1977).

[60] G. P. Collins, *Computing with quantum knots*, Scientific American **294**, 56 (2006).

[61] E. Prada, P. San-Jose, M. W. A. de Moor, A. Geresdi, E. J. H. Lee, J. Klinovaja, D. Loss, J. Nygård, R. Aguado, and L. P. Kouwenhoven, *From andreev to majorana bound states in hybrid superconductor–semiconductor nanowires*, Nature Reviews Physics **2**, 575 (2020).

[62] R. M. Lutchyn, E. P. A. M. Bakkers, L. P. Kouwenhoven, P. Krogstrup, C. M. Marcus, and Y. Oreg, *Majorana zero modes in superconductor–semiconductor heterostructures*, Nature Reviews Materials **3**, 52 (2018).

[63] D. E. Feldman, *The smallest particle collider*, Science **368**, 131 (2020).

[64] J. Nakamura, S. Liang, G. C. Gardner, and M. J. Manfra, *Direct observation of anyonic braiding statistics*, Nature Physics **16**, 931 (2020).

[65] P. C. Hohenberg, *Existence of long-range order in one and two dimensions*, Physical Review **158**, 383 (1967).

[66] N. D. Mermin and H. Wagner, *Absence of ferromagnetism or antiferromagnetism in one- or two-dimensional isotropic heisenberg models*, Physical Review Letters **17**, 1133 (1966).

[67] D. McCumber and B. Halperin, *Time scale of intrinsic resistive fluctuations in thin superconducting wires*, Physical Review B **1**, 1054 (1970), cited By 418.

[68] C. Lau, N. Markovic, M. Bockrath, A. Bezryadin, and M. Tinkham, *Quantum phase slips in superconducting nanowires*, Physical Review Letters **87** (2001), 10.1103/physrevlett.87.217003.

[69] S. De Graaf, R. Shaikhaidarov, T. Lindström, A. Tzalenchuk, and O. Astafiev, *Charge control of blockade of cooper pair tunneling in highly disordered tin nanowires in an inductive environment*, Physical Review B , 99 (2019).

[70] S. De Graaf, S. Skacel, T. Hönigl-Decrinis, R. Shaikhaidarov, H. Rotzinger, S. Linzen, and O. Astafiev, *Charge quantum interference device*, Nature Physics **14**, 590 (2018).

[71] J. P. Pekola, O.-P. Saira, V. F. Maisi, A. Kemppinen, M. Möttönen, Y. A. Pashkin, and D. V. Averin, *Single-electron current sources: Toward a refined definition of the ampere*, Reviews of Modern Physics **85**, 1421 (2013).

[72] Y. V. Nazarov, *Novel circuit theory of andreev reflection*, Superlattices and Microstructures **25**, 1221 (1999).

[73] L. Keldysh, *Diagram technique for nonequilibrium processes*, Soviet Physics JETP **20**, 1018 (1965).

[74] P. Coleman, *Introduction to Many-Body Physics* (Cambridge University Press, 2015).

2

WEYL DISKS

A variety of quantum systems exhibits Weyl points in their spectra where two bands cross in a point of three-dimensional parameters space with conical dispersion in the vicinity of the point. We consider theoretically the soft constraint regime where the parameters are dynamical quantum variables. We have shown that in general the soft constraints, in quasi-classical limit, result in Weyl discs where two states are (almost) degenerate in a finite 2d region of the 3d parameter space. We provide concrete calculations for two setups: Weyl point in a four-terminal superconducting structure and a Weyl exciton, i.e., a bound state of Weyl electron and a massive hole.

This chapter have been published as **Janis Erdmanis**, Árpád Lukács, Yuli V. Nazarov *Weyl Disks: Theoretical prediction*, Physical Review B (2018). For numerical code and data see https://doi.org/10.5281/zenodo.4068509

2.1. INTRODUCTION

The Weyl equation is written to describe the propogation of massless fermions [1, 2]. The 2×2 Weyl Hamiltonian is linear in the particle momenta $\mathbf{k}$ and has a conical spectrum with degeneracy at $\mathbf{k} = 0$. The Weyl equation describes neutrini if their masses can be neglected [3].

A variety of quantum systems exhibits similar spectral singularities in the vicinity of crossing of two bands in 3D parameter space. The degeneracy points are refered as Weyl points (WP). In solid state state physics the parameter space is the Brillion zone of a crystal lattice and Weyl physics is an active subject in experimental and theoretical research. WP are predicted theoretically in [4, 5], and recently observed experimentally [6, 7]. For reviews on materials hosting WPs, see [5, 8]. In the case of polyatomic molecules, the parameter space for Born-Oppenheimer energy levels is the positions of the nuclei; the existence of points of degeneracy is demonstrated in Refs. [9–11]. For molecular nanomagnets, the parameter space is the direction and magnitude of the external magnetic field; WPs result in resonances in tunneling probability [12, 13]. In the context of quantum transport, a setup with a WP in the space of two gate voltages and a superconducting phases has been proposed to realize a robust quantized current source [14]. WPs have been recently predicted [15, 16] in the spectrum of Andreev bound states (ABS) [17] in four terminal superconducting nanostructures where three independent phases form 3D paramater space. Quantized topological transconductance has been predicted. Similarly, WP can be also realized in three terminal systems [18].

It seems a relevant approximation to treat the parameters forming the space where the WP occurs, as fixed numbers (hard constraint). However, much more realistic and general situation is where the parameters are dynamical quantum variables, which can be the subject of fluctuations and also backaction from the system hosting the WP. To describe this situation of a *soft constraint*, one would, e.g., promote a parameter x to an operator $\hat{x}$, and add an energy term $A(\hat{x} - x_0)^2$ that attempts to constrain $\hat{x}$ to x_0 at sufficiently large A, and add a Hamiltonian accounting for the dynamics of $\hat{x}$.

In this Letter, we demonstrate the drastic consequences of a soft constraint in the vicinity of a WP. The degeneracy of two bands that has been restricted to a singular point for a hard constraint, in the quasi-classical limit spreads over to a finite two-dimensional region that we term *Weyl disc*. Quantum effects lift the degeneracy at the disc, resulting in strong anisotropy of the conical spectrum. We assess the situation in detail and provide detailed calculation of the quantum spectrum for two, very different, and physically interesting setups. The first setup is a multi-terminal superconducting nanostructure embedded in a linear circuit. The second setup is an exemplary band structure where a *Weyl exciton* consisting of a Weyl electron and a massive hole can be formed.

2.2. SETUP

Let us first describe the setups in detail. As shown in Ref. [15], the ABS spectrum of a four-terminal superconducting nanostructure can have WPs where ABS energy reaches zero (relative to Fermi level). This implies that the ground state of the nanostructure is close to the first excited singlet state. We count the phases from the WP position. The effective Hamiltonian in the vicinity of the WP reads $\hat{H}_{\mathrm{WP}} = (\hbar/2e) I_{na} \hat{\phi}_n \hat{\sigma}_a$, where $\hat{\sigma}_a$ denote the

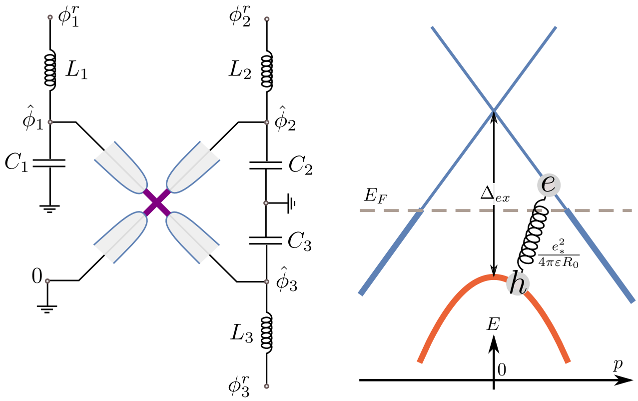

Figure 2.1: The two setups under consideration. Left: the 4 terminal superconducting nanostructure embedded in a linear circuit made of small inductances, $L_{1,2,3}$ and capacitances $C_{1,2,3}$. Right: a model band structure that supports Weyl excitons with energy $\approx \Delta_{ex}$ that are bound states of a Weyl electron and a massive hole, with the hole mass providing a soft constraint for the electron momentum.

Pauli matrices in the space of ground and excited singlet states [15]. The soft constraint situation occurs naturally if one takes into account self-inductances of the superconducting leads and associated capacitances (see Fig. 2.1). This promotes the superconducting phases at the nanostructure to dynamical variables $\hat{\phi}_n$, which are softly constrained to the superconducting phases ϕ_n^r, fixed by the magnetic fluxes in the corresponding superconducting loops. The full Hamiltonian encompasses inductive and capacitive energy and reads [15, 19, 20]

$$\hat{H} = \hat{H}_{\text{WP}} + \sum_n \left[\frac{(\hbar/2e)^2}{2L_n} (\hat{\phi}_n - \phi_n^r)^2 + \frac{(2e\hat{N}_n)^2}{2C_n} \right]. \tag{2.1}$$

Here the number operators $\hat{N}_n$ are canonically conjugate variables to the phases $\hat{\phi}_n$: $[\hat{N}_n, \hat{\phi}_m] = -i\delta_{nm}$ [17]. Here the inductive energy provides the soft constraint, and the capacitive energy is responsible for the quantum fluctuations of the phases.

For a complementary example with very different physical content, let us consider a solid exemplary band structure (Fig. 2.1b). It comprises an electron band with a WP and a parabolic valence band. To soft-constrain the momentum of the Weyl electron, let us tie it to a massive hole coming from the valence band. The bond is naturally provided by the Coulomb interaction, and the resulting particle is a sort of exciton, described by the Hamiltonian

$$\hat{H}_{\text{ex}} = \Delta_{\text{ex}} + \hat{H}_{\text{WP}} + \sum_n \frac{(\hat{p}_n - p_n^T)^2}{2m_n^*} - \frac{e_*^2}{4\pi\epsilon_0 r}, \tag{2.2}$$

where we count all momenta from the quasi-momentum of the Weyl point, $\hat{H}_{\text{WP}} = v_{na}\hat{p}_n\hat{\sigma}_a$, $\hat{p}_n$ are the components of the quasi-momentum of the Weyl electron, p_n^T are those of the total exciton quasi-momentum, m_n^* are the (possibly anisotropic) hole masses, and the last term presents Coulomb attraction between electron and hole, $r = |\mathbf{r}|$ being the distance between these two particles.

Let us note the close similarity: H_{WP} and the soft constraint term in Eq. (2.2) are brought to the form in Eq. (2.1) with the replacements $p_n \to P\phi_n$, $Pv_{na} \to (\hbar/2e)I_{na}$, $(P^2/2m_n^*) \to (\hbar/2e)^2/2L_n$, where P is a constant with momentum dimension. Since $\mathbf{r}$ is canonically conjugate to $\mathbf{p}$, the Coulomb energy plays a role similar to the capacitive energy in the Hamiltonian (2.1), providing the quantum fluctuations of $\mathbf{p}$.

For both setups, we evaluate the energies of the discrete quantum states, analyzing their dependence on the parameters, either ϕ_n^r or p_n^T.

2.3. RESULTS

Systems described by the Hamiltonians (2.1, 2.2), depending on the parameters, can be in two regimes: the quasi-classical and the opposite, deeply quantum one.

To understand the regimes, let us consider the one-dimensional version of Eq. (2.1). It is exactly solvable, since the quasi-spin part has a single spin component, which can be diagonalized simultaneously with the Hamiltonian. For the spin eigenvalue $\sigma = \pm 1$, the kinetic part of the Hamiltonian is $(\hbar/2e)^2(1/2L)(\hat{\phi} - \phi^r + \sigma\phi_0)^2 - LI^2/2$, with $\phi_0 = (2e/\hbar)IL$. At $\phi^r = 0$, it gives rise to two degenerate minima separated by $2\phi_0$ with an energy barrier $E_B = LI^2/2$ between them. The Hamiltonian for both values of σ is that of a harmonic oscillator, with frequency $\omega = 1/\sqrt{LC}$. The quasiclassical parameter $\mathcal{Q}$ is defined as the ratio of the barrier height and the energy quantization of the oscillators, and reads

$$\mathcal{Q} = \frac{1}{2}\left(\frac{LIe}{\hbar}\right)^2 \frac{\hbar}{e^2 Z}, \tag{2.3}$$

where $Z = \sqrt{L/C}$ is the characteristic impedance of the oscillator. In Eq. (2.3), an estimation for the first term is ratio of typical inductance of the superconducting structure, which has to be small to provide good confinement. However, the second term is large, estimated as the ratio of vacuum impedance to resistance quantum $\sim 10^2$. This is why the quasi-classical limit $\mathcal{Q} \gg 1$ is well achievable. In a 3d case, we define $\mathcal{Q}$ with respect to the maximal $L_n I_n^2$ (*easy direction*).

Similar analysis for the Hamiltonian (2.2) yields in 1d a barrier height of $E_B = m^* v^2/2$. The parameter $\mathcal{Q}$ is defined as the ratio of the barrier height to the ground state Coulomb binding energy $E_b \propto (e_*^2/4\pi\epsilon_0)^2 m^*/2\hbar^2$, yielding

$$\mathcal{Q} = \left(\frac{\hbar v 4\pi\epsilon_0}{e_*^2}\right)^2. \tag{2.4}$$

If one estimates the Weyl velocity v with the typical Fermi velocity for metals $v_F \sim 10^6\mathrm{ms}^{-1}$, and the dielectric constant as $\epsilon_r \approx 10$, $\mathcal{Q} \sim 25$, therefore the quasi-classical limit is well achievable in solids. In a 3d case, we define $\mathcal{Q}$ with the parameters in the easy direction (maximal mv^2).

The deeply quantum limit $\mathcal{Q} \ll 1$ is in fact not interesting, since there the Weyl energy is not modified by the soft constraint, except for trivial perturbative corrections.

In this study we concentrate on the quasi-classical limit. We give analytical results valid at $\mathcal{Q} \gg 1$ and numerical results for $\mathcal{Q} \sim 5$.

In the quasi-classical regime, we neglect the fluctuations of the phases ϕ_n and replace the quasi-spin term, H_{WP} with one of its eigenvalues. The matrix I_{na} can be diagonalized

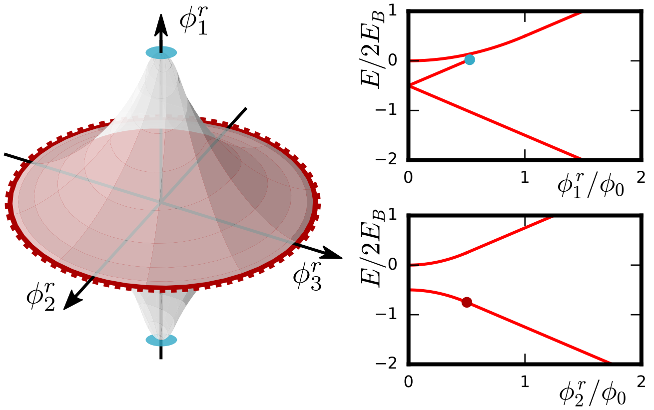

Figure 2.2: The Weyl disc. *Left*: The region in parameter space ϕ_n^r (or p_n^T) where three quasi-classical energy minima exists. The two minima are degenerate at the disc in the plane (ϕ_2^r, ϕ_3^r). *Right*: The quasi-classical energy spectrum in the easy direction (*top*) and in a direction within the disc (*bottom*). The dots mark the region edges. (The paramerer choice is $L_n = L/n$ and $I_n = I$.)

by a coordinate transformation $I_{na} \to I_n \delta_{na}$[1]. Then we need to minimize

$$E_{\mathrm{cl},\sigma} = \frac{\sigma\hbar}{2e}\sqrt{\sum_n I_n^2 \phi_n^2} + \left(\frac{\hbar}{2e}\right)^2 \sum_n \frac{(\phi_n - \phi_n^r)^2}{2L_n}. \tag{2.5}$$

If $|\phi_n^r| \gg \phi_0$, the minimization reproduces the two cones of the Weyl spectrum, $(\sigma\hbar/2e)\sqrt{\sum_n I_n^2 (\phi_n^r)^2}$. In the vicinity of the Weyl point $|\phi_n| \sim \phi_0$, the Weyl spectrum is drastically modified (see Fig. 2.2). Most importantly, the minimization gives two minima for $\sigma = -1$ in the 3d region shown in the figure. These two minima are precisely degenerate at a 2d *Weyl disc*, which is perpendicular to the *easy direction*, where $L_n I_n^2$ is maximal ($n = 1$ for the easy direction). The disc is an ellipse with dimensions $(4e/\hbar)(L_1 I_1^2 - L_m I_m^2)/I_m$, $m = 2, 3$.

In Fig. 2.2 we plot the energies along the easy direction and in the plane of the disc. There is a linear dependence of the energies in the easy direction. The second minimum for $\sigma = -1$ disappears at a critical value of ϕ_1^r. For even larger ϕ_1^r, the Weyl spectrum $E \approx (\hbar/2e) I_1 \sigma \phi_1^r$ is seen again. If we move along the disc, two minima remain degenerate until they merge at the disc edge.

The same minimization applies to the Weyl exciton setup. In this case, the lowest curves in Fig. 2.2 define the lower boundary of the continuos spectrum. The bound exciton states follow the edge at slightly lower energy, with binding energy $E_b \ll E_B$. If we move along the disc, all bound states remain doubly degenerate, till the edge of the disc. They split linearly if we move in the easy direction.

This brings us to the main conclusion of the paper: in the quasi-classical limit $\mathcal{Q} \gg 1$, soft constraints extend the isolated degeneracy in the WP into a finite 2d region. This property of WP can be used for the purposes of quantum manipulation and computation.

---

[1] see appendix

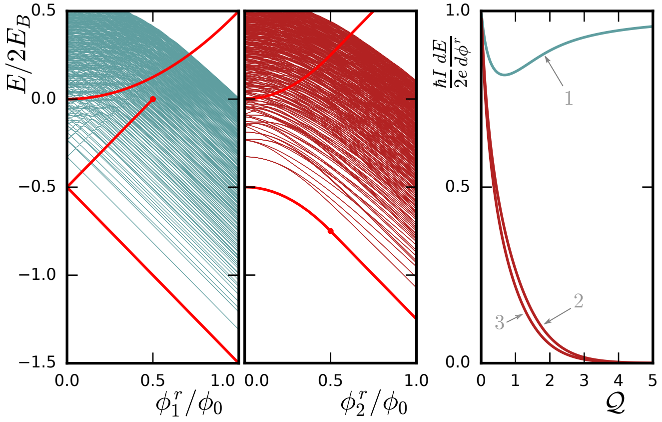

Figure 2.3: The energy spectrum of the circuit shown in Fig. 2.1 for $\mathcal{Q} = 5$ in the easy direction (*left panel*) and in the plane of the disc (*center panel*). The parameters are $L_n = L/n$, $C_n = C = \hbar^2\mathcal{Q}^2/LE_B^2$, $I_n = I$ and $\mathcal{Q} = 5$ (L and I arbitrary). We also show the "velocities" $\partial E/\partial\phi_n^r$ vs. the quasi-classical parameter $\mathcal{Q}$ in the ground state (*right panel*).

At large but finite values of $\mathcal{Q}$ the degeneracy at the disc is lifted, albeit the corresponding energy splittings remain relatively small at moderate values of $\mathcal{Q}$. We illustrate this with numerical results for both setups. In Fig. 2.3 we plot the full energy spectrum of the superconducting nanostructure for $\mathcal{Q} = 5$. Besides the ground state, the spectrum includes the corresponding excitations in three oscillators. For comparison, in Fig. 2.3, we plot in red the quasi-classical results from Fig. 2.2. Upon a small shift, the lowest curves give a good approximation for the numerical energies of the lowest states. At $\phi^r = 0$ all levels are doubly degenerate. If we move in the easy direction, the levels are split with $\Delta E \propto (\hbar/e)I_1\phi_1^r$. The levels become increasingly dense at higher energies. Since the level begin to cross, this behaviour is restricted to increasingly small values of ϕ_1^r. At $\phi_1^r < 0.5\phi_0$, the crossings are avoided at an exponentially small energy scale corresponding to the tunneling amplitude between the minima. The amplitude increases with energy owing to a bigger overlap of the oscillator excited states in two minima.

If we move in a perpendicular direction, we observe an exponentially small energy splitting at $\phi_{2,3} \approx 0.4\phi_0$. At small $\phi_{2,3}^r$, the splitting is $\Delta E \approx (\hbar/e)I_{2,3}\phi_{2,3}^r e^{-2\mathcal{Q}}$ in the ground state[2]. We see this suppression in the plot of the normalized "velocities" of the lowest state, $(2e/\hbar I_1)\partial E/\partial\phi_n^r$ at $\phi^r \to 0$ (Fig. 2.3, right panel). In the deep quantum limit, $\mathcal{Q} \lesssim 1$, all velocities remain the same as for the original Weyl spectrum. The velocity in the easy direction stays closer to this value at any $\mathcal{Q}$.

In Fig. 2.4 we show spectrum of the exciton Hamiltonian (2.2) for $\mathcal{Q} = 20$ is shown. For the same of numerical efficiency, we have computed the spectrum in 2d limit. This is valid in the higly anisotropic limit $m_3^* \ll m_{1,2}^*$. Also, graphene provides a practical example of a stable conical spectrum in 2d. With graphene data, $v \approx v_F$ and a substrate with a relative permittivity ~ 10, $\mathcal{Q} \sim 20$ [21]. The continuous spectrum is shown by the shaded region. Its lower edge is given by the quasi-classical result (Fig. 2.2). Below the

---

[2] see appendix

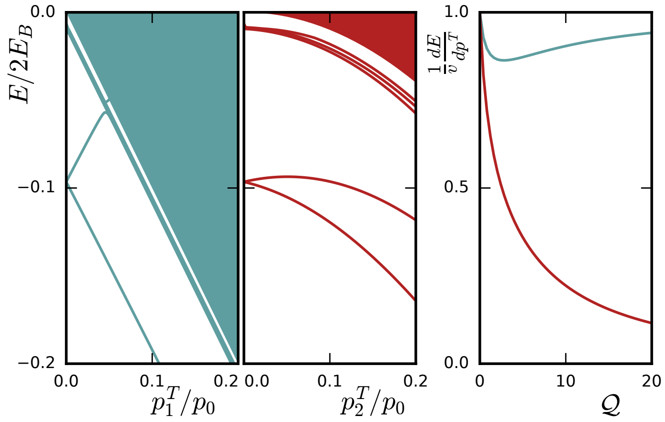

Figure 2.4: The energy spectrum of a two-dimensional anisotropic Weyl exciton for $\mathcal{Q} = 20$ in the easy direction (*left panel*) and in the plane of the disc (*center panel*). The parameters are $m_n = m/n$, $v_n = v$, $e_*^2 = \hbar v 4\pi\epsilon_0/\sqrt{\mathcal{Q}}$ and $\mathcal{Q} = 20$ (v and m arbitrary). We also show the velocities $\partial E/\partial p_n^T$ vs. the quasi-classical parameter $\mathcal{Q}$ in the lowest state of the exciton (*right panel*).

edge, we plot the energies of the five lowest bound states. If we go in the easy direction, we observe an almost unmodified Weyl spectrum for the lowest and the first excited states. In contrast to this, the splitting between these states remains small in the plane of the disc. This is seen for the lowest and the first excited states as for third and fourth excited states, that are close to the edge. In the right panel of Fig. 2.4, we plot the normalized velocities of the lowest state vs. $\mathcal{Q}$. Similarly to the case of the superconducting nanostructure, the Weyl velocity in the easy direction is hardly modified, while that in perpendicular direction is strongly suppressed with increasing $\mathcal{Q}$. In fact, the wave function of the bound state near one of the minima is singular in coordinate space owing to the the singularity of the Coulomb potential at $r \to 0$. The calculation of the amplitude of tunneling between the minima demonstrates that the value of the amplitude is determined by this singularity. This results in power-law suppression $\partial E/\partial p_n^T = \pm v_n/2\mathcal{Q}^4$ in the ground state[3] in 3d. In 2d, $\partial E/\partial p_n^T = \pm v_n/2(\mathcal{Q}/4)^3$. [In 2d, we use the definition $\mathcal{Q} = 4E_B/E_b$ to obtain Eq. (2.4).]

2.4. SUMMARY AND CONCLUSIONS

In conclusion, we have shown that a Weyl spectrum is essentially modified by soft constraints of the spectral parameters in the quasi-classical limit. A Weyl disc emerges in the vicinity of the WP. There are two degenerate states at the disc, that are slightly split at moderate values of the quasi-classical parameter $\mathcal{Q}$. Such extension of a degenerate point to a finite region of parameter space can be useful for purposes of quantum technologies.

We illustrate this general statement with two examples of very different physical systems. The first system is a multi-terminal superconducting nanostructure where the spectral parameters are the superconducting phases and the soft constraint is realized by an

---

[3] see appendix

external circuit. The second example concerns a Weyl exciton that is the bound state of a Weyl electron and a massive hole. The mass provides a soft constraint of the total exciton quasi-momentum to the momentum of the Weyl electron. We show that in both examples, the quasi-classical regime can be achieved with a reasonable parameter choice.

2.5. APPENDIX

In this supplementary material, we present the details and the derivations of the results in the main text. We present the detailed minimization of the energy in the quasi-classical limit for the two setups considered in the main text, for the nanostructure and for the Weyl exciton. We present the perturbation theory for the splitting at the Weyl disc, at large but finite $\mathcal{Q}$. We shortly summarize the numerical approach we use. We present estimated exciton parameters for a number of materials with Weyl points in their band structure, as well as a proposed way of detecting Weyl excitons. In the last section, we outline the advantages of a nanodevice tuned to its Weyl point as a physical realization of a qubit.

2.5.1. QUASI-CLASSICAL APPROXIMATION: NANOSTRUCTURE

The quasi-classical energy expression is obtained from the Hamiltonian (2.1) by replacing the operator $\hat{\phi}_n$ with its mean value ϕ_n, and at the same time, the quasi-spin part of the Hamiltonian H_{WP} with one of its eigenvalues $\sigma\sqrt{I_{na}I_{ma}\phi_n\phi_m}$, with $\sigma = \pm 1$. The resulting expression is

$$E_{\mathrm{cl},\sigma} = \left(\frac{\hbar}{2e}\right)^2 \sum_n \frac{(\phi_n - \phi_n^r)^2}{2L_n} + \frac{\sigma\hbar}{2e}\sqrt{I_{na}I_{ma}\phi_n\phi_m}. \tag{2.6}$$

Note, that it $\phi = I^{-1}OI_0\phi'$, where $I_0 = \mathrm{diag}(I_1, I_2, I_3)$, and $O = (O^T)^{-1}$ is such that $G^{-1} = I_0^{-2}OI^TLIO^T$ is diagonal, then the form (2.5) is achieved.

To obtain the quasi-classical approximation of the energy levels, one shall minimize (2.6) w.r.t. ϕ_n. This amounts to either setting $\phi_n = 0$ (minimum at the boundary), or solving the equation

$$\frac{\partial E_{\mathrm{cl},\sigma}}{\partial \phi_n} = \left(\frac{\hbar}{2e}\right)^2 \frac{\phi_n - \phi_n^r}{L_n} + \frac{\sigma\hbar}{2e}\frac{I_n^2\phi_n}{\sqrt{\sum_k I_k^2\phi_k^2}} = 0 \tag{2.7}$$

and verifying that the second derivative matrix,

$$\frac{\partial^2 E_{\mathrm{cl},\sigma}}{\partial \phi_n \partial \phi_m} = \left(\frac{\hbar}{2e}\right)^2 \frac{\delta_{nm}}{L_n} + \frac{\sigma\hbar}{2e}\left[\frac{I_n^2\delta_{nm}}{\sqrt{\sum_k I_k^2\phi_k^2}} + \frac{I_n^2\phi_n I_m^2\phi_m}{\left(\sum_k I_k^2\phi_k^2\right)^{3/2}}\right] \tag{2.8}$$

is positive definite. The boundary of the solid body, where three solutions (one for $\sigma = 1$ and two for $\sigma = -1$) exist in the left hand side of Fig. 2.2 is given by the vanishing of one eigenvalue (and hence the determinant) of the matrix (2.8). There, one of the $\sigma = -1$ solutions ceases to be a true minimum.

For simplicity sake, let us assume in what follows, that $0 < L_3I_3^2 < L_2I_2^2 < L_1I_1^2$. The direction corresponding to the latter one, ϕ_1 is thus the easy direction.

The minima of $E_{\mathrm{cl},\sigma}$ are obtained as follows:

1. For $\sigma = 1$ and $\sum_n (\hbar/2e)^2(\phi_n^r/L_n I_n)^2 < 1$, the minimum is at $\phi_n = 0$, as there is no solution to Eq. (2.7). Here, the obtained minimum is $E_{\mathrm{cl},+} = \sum_n (\hbar/2e)^2(\phi_n^r)^2/2L_n$.
2. For $\sigma = 1$ and $\sum_n (\hbar/2e)^2(\phi_n^r/L_n I_n)^2 \geq 1$, the solutions are obtained in a parametric form as
$$I_n\phi_n = r u_n\,, \quad I_n\phi_n^r = \left(r + \frac{\sigma 2e}{\hbar} L_n I_n^2\right) u_n\,, \tag{2.9}$$
where $u_n u_n = 1$ (3d unit vector). Here, the quasi-classical energy is
$$E_{\mathrm{cl},\sigma} = \sum_n \frac{L_n I_n^2 u_n^2}{2} + \frac{\sigma\hbar}{2e} r\,. \tag{2.10}$$
Items 1. and 2. shall be referred to as the *upper energy surface*.
3. For $\sigma = -1$ and $(2e/\hbar)L_2 I_2^2 < r < (2e/\hbar)L_1 I_1^2$, for a domain of parameters ϕ_n^r, Eq. (2.9) gives minima (2.10). One boundary of this domain is at $r = (2e/\hbar)L_1 I_1^2$, and the other one is determined by the radius $r_c(u)$, where the second derivative matrix (2.8) ceases to be positive definite (its determinant crosses zero). This surface is shown in Fig. 2.2.
4. For $\sigma = -1$ and $r = (2e/\hbar)L_1 I_1^2$, the *Weyl disc* is obtained. Here $\phi_1^r = 0$, and
$$\begin{aligned} E_{\mathrm{cl},-} = &-\frac{L_1 I_1^2}{2} \\ &-\left(\frac{\hbar}{2e}\right)^2 \sum_{n\neq 1} \frac{(\phi_n^r)^2/(2L_n L_1)}{(I_1/I_n)^2/L_n - 1/L_1}\,. \end{aligned} \tag{2.11}$$
5. For $\sigma = -1$ and $r > (2e/\hbar)L_1 I_1^2$, Eq. (2.9) yields the minima (2.10).
Items 4. and 5. shall be referred to as the *intermediate* and the *lower energy surfaces*, respectively.

2.5.2. QUASI-CLASSICAL APPROXIMATION FOR THE EXCITON

Let us perform a similar analysis for the Hamiltonian (2.2). The quasi-classical energy is in this case
$$E_{\mathrm{cl},\sigma} = \sum_n \frac{(p_n - p_n^T)^2}{2m_n^*} + \sigma\sqrt{v_{na} v_{ma} p_n p_m}\,, \tag{2.12}$$
where, similarly to the case of the nanostructure, with the transformation $\mathbf{p} \to v^{-1} O v_0 \mathbf{p}'$, where v_0 and $m^{-1} = v_0^{-2} O v^T m v O^T$ are diagonal, $O^T O = 1$, can be transformed to the form
$$E_{\mathrm{cl},\sigma} = \sum_n \frac{(p_n - p_n^T)^2}{2m_n^*} + \sigma\sqrt{\sum_n v_n^2 p_n^2}\,. \tag{2.13}$$
The minimization is done in a similar fashion. The first and second derivatives are
$$\frac{\partial E_{\mathrm{cl},\sigma}}{\partial p_n} = \frac{p_n - p_n^T}{m_n^*} + \sigma \frac{v_n^2 p_n}{\sqrt{\sum_k v_k^2 p_k^2}}\,, \tag{2.14}$$

and

$$\frac{\partial^2 E_{\mathrm{cl},\sigma}}{\partial p_n \partial p_m} = \frac{\delta_{nm}}{m_n^*} + \sigma \left[\frac{v_n^2 \delta_{nm}}{\sqrt{\sum_k v_k^2 p_k^2}} + \frac{v_n^2 p_n v_m^2 p_m}{(\sum_k v_k^2 p_k^2)^{3/2}} . \right] \tag{2.15}$$

The minima are as follows:

1. For $\sigma = 1$ and $\sum_n (p_n^T / m_n^* v_n)^2 < 1$, the minimum is at $p_n = 0$, as there is no solution to Eq. (2.14). Here, the obtained minimum is $E_{\mathrm{cl},+} = \sum_n (p_n^T)^2 / 2m_n^*$.

2. For $\sigma = 1$ and $\sum_n (p_n^r / m_n^* v_n)^2 \geq 1$, the solutions are obtained in a parametric form as

$$v_n p_n = s u_n , \quad v_n p_n^T = \left(s + m_n^* v_n^2 \right) u_n , \tag{2.16}$$

   where $u_n u_n = 1$ (3d unit vector). Here, the quasi-classical energy is

$$E_{\mathrm{cl},\sigma} = \sum_n \frac{m_n v_n^2 u_n^2}{2} + \sigma s . \tag{2.17}$$

   Items 1. and 2. shall form the *upper energy surface.*

3. For $\sigma = -1$ and $m_2 v_2^2 < s < m_1 v_1^2$, for a domain of parameters p_n^T, Eq. (2.16) gives minima (2.17). One boundary of this domain is at $s = m_1 v_1^2$, and the other one is determined by the radius $s_c(u)$, where the second derivative matrix (2.15) ceases to be positive definite (its determinant crosses zero). This surface is shown in Fig. 2.2.

4. For $\sigma = -1$ and $s = m_1 v_1^2$, the *Weyl disc* is obtained. Here $p_1^T = 0$, and

$$E_{\mathrm{cl},-} = -\frac{m_1 v_1^2}{2} - \sum_{n \neq 1} \frac{(p_n^T)^2 / (2 m_n^* m_1^*)}{(v_1 / v_n)^2 / m_n^* - 1 / m_1^*} . \tag{2.18}$$

5. For $\sigma = -1$ and $s > m_1 v_1^2$, Eq. (2.16) yields the minima (2.17).

   Items 4. and 5. form the *intermediate* and the *lower energy surfaces*, respectively. The solid body on Fig. 2.2 shows the parameter values for which both solution exist.

2.5.3. PERTURBATION THEORY

We obtain here formulae for the energy splitting between the degenerate levels in the Weyl disc with the help of perturbation theory. Let us write the Hamiltonian (2.2) in the form

$$\hat{H} = \frac{(\hat{\mathbf{p}} - \mathbf{p}^T)^2}{2m^*} + \hat{H}_{\mathrm{WP}} + V(\mathbf{r}) , \tag{2.19}$$

where we have assumed that the effective masses are isotropic, and $\hat{H}_{\mathrm{WP}} = \sum_n v_n \hat{p}_n \hat{\sigma}_n$. Let us note first, that the nanostructure Hamiltonian (2.1) is also of this form, with the replacements $m_n \to (2eP/\hbar)^2 L_n$ (P is an arbitrary constant of momentum dimension), $v_n \to (\hbar / 2eP) I_n$, $\hat{p}_n \to P \hat{\phi}_n$, $p_n^T \to P \phi_n^r$ and $x_n \to (\hbar / P) \hat{N}_n$. The potential for the exciton is then $V(\mathbf{r}) = e_*^2 / (r \pi \epsilon_0 r) + \Delta_{\mathrm{ex}}$, and for the nanostructure $V(\mathbf{r}) = \sum_n k_n x_n^2 / 2 = \sum_n (2eN_n)^2 / 2C_n$.

We split the Hamiltonian (2.19) into unperturbed part and perturbation as $H = H_0 + H_1$, where $H_1 = \sum_{n\neq 1} v_n \hat{p}_n \hat{\sigma}_n$. We start with the solutions of the problem

$$\left[\frac{\hat{\mathbf{p}}^2}{2m^*} + V(\mathbf{r})\right]\psi_0 = \tilde{E}\psi_0(\mathbf{r})\,. \tag{2.20}$$

In the case of the superconducting nanostructure, these are

$$\psi_0(\phi) = \prod_k \phi^H_{nk}(\phi_k)\,, \quad \tilde{E} = \sum_k \hbar\omega_k\left(n_k + \frac{1}{2}\right), \tag{2.21}$$

where ϕ^H_{nk} are harmonic oscillator eigenstates with $\omega_k = 1/\sqrt{L_k C_k}$. For the exciton, the eigenfunctions are hydrogen eigenfunctions, and the energy levels are

$$\tilde{E} = -\left(\frac{e_*^2}{4\pi\epsilon_0}\right)^2 \frac{m^*}{\hbar^2}\frac{1}{2n^2}\,, \tag{2.22}$$

where n is the principal quantum number, and there is a degeneracy $\ell = 0,\dots,n-1$ and $m = -\ell,\dots,\ell$. In two dimensions, $1/2n^2$ shall be replaced by $1/2(n-1/2)^2$, and the degeneracy is due to $m = -n+1,\dots,n-1$. In both cases, $n = 1,2,\dots$.

If ψ_0 solves Eq. (2.20), then so does

$$\psi(\mathbf{r}) = \exp\left(\frac{\mathrm{i}}{\hbar}\left[(p_1^T - \sigma m_1^* v_1)x_1 + p_2^T x_2 + p_3^T x_3\right]\right)\psi_0(\mathbf{r})|\sigma\rangle \tag{2.23}$$

solve $H_0\psi = E_0\psi$ where $\hat{\sigma}_1|\sigma\rangle = \sigma|\sigma\rangle$, and $E_0 = \tilde{E} - m_1^* v_1^2/2 + \sigma v_1 p_1^T$, or, for the nanostructure $E_0 = \tilde{E} - L_1 I_1^2/2 + \sigma(\hbar/2e)I_1\phi_1^r$. Eq. (2.23) describes wave functions localized at the two energy minima (i.e., shifted in momentum space).

We obtain the energy splitting in the disc as $\Delta E = 2|t|$, where

$$\begin{aligned} t &= \langle\sigma|\hat{H}_1|-\sigma\rangle = \langle\sigma|\sum_k v_k p_k^T \hat{\sigma}_k|-\sigma\rangle \\ &= \langle\sigma|\sum_k v_k p_k^T \hat{\sigma}_k|-\sigma\rangle_{\mathrm{spin}} \int \mathrm{d}^d x \mathrm{e}^{\frac{2\mathrm{i}}{\hbar} m_1^* v_1 x_1} |\psi_0(\mathbf{r})|^2 \end{aligned} \tag{2.24}$$

is the tunneling matrix element between states of the same quantum number localized about the two energy minima. Evaluating Eq. (2.24) for the nanostructure yields

$$\begin{aligned} t &= \langle\sigma|\sum_k \hbar I_k \phi_k^r/2e\hat{\sigma}_k|-\sigma\rangle_{\mathrm{spin}} \mathrm{e}^{-2\mathcal{Q}} L_{n_1}(4\mathcal{Q})\,, \\ &\sim \langle\sigma|\sum_k \hbar I_k \phi_k^r/2e\hat{\sigma}_k|-\sigma\rangle_{\mathrm{spin}} \mathrm{e}^{-2\mathcal{Q}} \frac{(4\mathcal{Q})^{n_1}}{n_1!}\,, \end{aligned} \tag{2.25}$$

where n_1 is the excitation of the easy direction oscillator. The asymptotic formula holds in the quasi-classical limit, $\mathcal{Q} \to \infty$.

For the exciton, the same kind of calculation for the ground state $\psi_0 = \mathrm{e}^{-\tilde{r}}/\sqrt{\pi}$, where $\tilde{r} = m/\hbar^2(e^2/4\pi\epsilon_0)r$, yields

$$t = \frac{\langle\sigma|\sum_k v_k p_k^T \hat{\sigma}_k|-\sigma\rangle_{\mathrm{spin}}}{2(1+\mathcal{Q}^2)^2} \sim \frac{\langle\sigma|\sum_k v_k p_k^T \hat{\sigma}_k|-\sigma\rangle_{\mathrm{spin}}}{2\mathcal{Q}^4} \tag{2.26}$$

Material	Ref.	a, c Å	PPB	Δp $\hbar\pi/a$	Δ_{ex} eV	m_* m_e	v 10^5ms^{-1}	ϵ_r
graphene	[22–24]	2.5	K	0	10	20	6	17…37
germanene	[22, 25]	3.8	K	0	4	20	3	17…37
TaAs	[26–28]	3.5,11.8	Σ	0.02	0.4	0.2	4	100
NbAs	[26, 28]	3.5,11.8	Σ	0.02	0.1	0.2	4	250

Table 2.1: Data of some materials with Weyl points in their band structure. Notation (other than those used in the main text): a and c are the lattice constants, Δp the distance between the Weyl point and the parabolic minimum in the Brillouin zone and PPB the position of the parabolic minimum in the Brillouin zone.

in 3d. The suppression in Eq. (2.26) is of the power-law type, in contrast to the exponential suppression in Eq. (2.25), as a result of the non-smooth behavior of the hydrogen wave functions at the origin, owing to the singularity of the Coulomb potential. In 2d, $t = \langle\sigma|p_2^T v_2\hat\sigma_2|-\sigma\rangle/(1+\mathcal{Q}^2)^{3/2} \sim \langle\sigma|p_2^T v_2\hat\sigma_2|-\sigma\rangle/\mathcal{Q}^3$.

2.5.4. NUMERICAL METHODS

In the case of the superconducting nanostructure, we use the fact, that the Hamiltonian (2.1) contains 3 harmonic oscillators to introduce CAPs as $\hat\phi_n - \phi_n^r = (\hat a_n{}^\dagger + \hat a_n)/\alpha_n$, yielding

$$\hat H = \sum_n \hbar\omega_k \left(\hat a_n{}^\dagger \hat a_n + \frac{1}{2}\right) + \sum_n \frac{\hbar I_n}{2e}\hat\phi_n\hat\sigma_n, \tag{2.27}$$

where $\omega_n = 1/\sqrt{L_n C_n}$, $\alpha_n = e\sqrt{2/\hbar}(L_n/C_n)^{1/4}$, and $[\hat a_n, \hat a_m{}^\dagger] = \delta_{nm}$.

The quasiclassical analysis presented in the main text yields that the ground state is centered at $\phi_1 = \pm\phi_0$, $\phi_{2,3} = 0$, similarly to a coherent state with parameter $\pm\sqrt{Q}$, therefore the number of states necessary to expand it is $N \sim \mathcal{Q}$. In the orthogonal directions, we use $N/2$ states, and 2 for spin. We find he low-lying eigenvalues of the resulting sparse $N^3/2 \times N^3/2$ matrix with Julia library routines. For Fig. 2.3, we have used $N = 50$.

In the case of the exciton, we use a standard finite difference approach, with a 5 point stencil for both second derivatives, and Richardson extrapolation from two different grid scpacings to enhance the accuracy. The grid used is equidistant in a logarithmic variable to enhance resolution in the vicinity of the origin, where the wave function is non-smooth. We use a couple of hundred points in each direction. The accurary is verified with computing the standard Coulomb eigenvalues on the same grid, and comparing them to the exact results.

2.5.5. ESTIMATED EXCITON DATA FOR SOME MATERIALS

The exctions considered in the main text are bound states of one quasiparticle with a Weyl spectrum and one with a parabolic dispersion. Here we consider some examples, in materials whose band structure contains a Weyl point and a close parabolic minimum.

In Table 2.1 we summarize some data of these materials, and the sources of the data, whereas in Table 2.2, the resulting exciton parameters are given (from the quasi-classical approximation. The binding energy was estimated as $E_b = (e^2/4\pi\epsilon_0\epsilon)^2 m^*/2\hbar^2$ and qua-

Material	E_b eV	$\mathcal{Q}$
graphene	1.2…0.2	17…103
germanene	1.2…0.2	4…26
TaAs	$3\cdot10^{-4}$	300
NbAs	$5\cdot10^{-5}$	1800

Table 2.2: Data of Weyl excitons calculated from material data in Table 2.1.

siclassicla parameter $Q = (\hbar v 4\pi\epsilon_0\epsilon/e^2)^2$ [see Eq. (2.4)]. In the case of 2D materials, ϵ_r is the relative dielectric constant of the substrate.

2.5.6. DETECTION OF WEYL EXCITONS

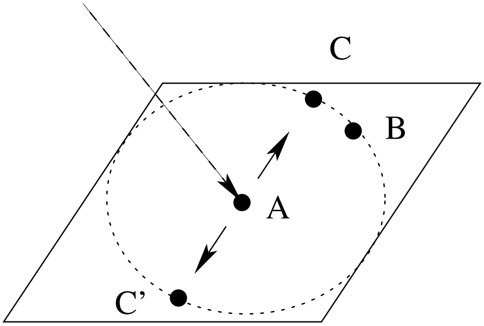

Figure 2.5: A proposed experiment for the detection of Weyl excitons.

Let us consider the following proposed experiment, as depicted in Fig. 2.5 At point "A" in a sample, excitons are created (e.g., by light irradiation, or, if the non-zero momentum of the exciton necessitates, with two-photon absorption or with an accompanying phonon, etc., [29, 30]). Provided that these are Weyl excitons, their velocity in the directions other than the easy one, $\partial E/\partial p_n^T$, are suppressed. Therefore, excitons only propagate in the easy direction (marked by solid arrows), they cannot be detected in other direction from where they were created, e.g., at point "B", unlike at the points "C" and "C'". Detection of excitons may be possible by detecting the photon created by its decay, or by splitting the exciton into an electron and a hole by electric field, and detecting these by conduction measurement [31].

2.5.7. POSSIBLE QUANTUM COMPUTATION APPLICATIONS

The possibility of using such a system as the physical realization of a qubit. The external phases ϕ_n^r are in this case the tunable parameters wich can be used to perform manipulation of the states of this qubit (see Ref. [17]).

The energy levels of the system at hand are degenerate for a finite range of parameters, i.e., within the Weyl disc. The existence of such a degenerate subspace for a parametric

Hamiltonian is at the basis of holonimical quantum computation [32, 33]. An advantage of such schemes is their robustness against parametric noise [34]. For reviews, see Refs. [35, 36]. On the possibility of the coherent manipulation of the Andreev states of superconducting junctions, and their readout, see Ref. [37].

REFERENCES

[1] H. Weyl, *Electron und Gravitation*, Z. Phys. **56**, 330 (1929).

[2] P. B. Pal, *Dirac, majorana, and weyl fermions*, Amer. J. Phys. **79**, 485 (2011).

[3] T.-P. Cheng and L.-F. Li, *Gauge theory of elementary particle physics*, Vol. 38 (Clarendon Press, Oxford, 1984) pp. 78–79.

[4] C. Herring, *Accidental degeneracy in the energy bands of crystals*, Physical Review **52**, 365 (1937).

[5] M. Z. Hasan *et al.*, *A Weyl fermion semimetal with surface Fermi arcs in the transition metal monopnictide TaAs class*, Nat. Comm. **6**, 7373 (2015).

[6] L. Lu, Z. Wang, D. Ye, L. Ran, J. D. Joannopoulos, and M. Soljacic, *Experimental observation of Weyl points*, Science **349**, 622 (2015).

[7] M. Z. Hasan *et al.*, *Discovery of a Weyl fermion semimetal and topological Fermi arcs*, Science **349**, 613 (2015).

[8] B. Yau and C. Felser, *Topological materials: Weyl semimetals*, Annu. Rev. Condensed Matter Phys. **2017.8**, 337 (2017).

[9] G. Herzberg and H. C. Longuet-Higgins, *Intersection of potential energy surfaces in polyatomic molecules*, Discuss. Faraday Soc. **35**, 77 (1963).

[10] F. Faure and B. I. Zhilinskii, *Topological Chern indices in molecular spectra*, Phys. Rev. Lett. **85**, 960 (2000).

[11] B. I. Zhilinskii, *Symmetry, invariants, and topology in molecular models*, Phys. Rep. **341**, 85 (2001).

[12] W. Wernsdorfer and R. Sessoli, *Quantum phase interference and parity effects in magnetic molecular clusters*, Science **284**, 133 (1999).

[13] W. Wernsdorfer, N. E. Chakov, and G. G. Christou, *Quantum phase interference and parity effects in* Mn_12 *single-molecule magnets*, Phys. Rev. Lett. **95**, 037203 (2005).

[14] R. Leone, L. P. Lévy, and P. Lafarge, *Cooper-pair pump as a quantized current source*, Phys. Rev. Lett. **100**, 117001 (2008).

[15] R.-P. Riwar, M. Houzet, J. S. Meyer, and Y. V. Nazarov, *Multi-terminal josephson junctions as topological matter*, Nature Communications **7**, 11167 (2016).

[16] E. Eriksson, R.-P. Riwar, M. Houzet, J. S. Meyer, and Y. V. Nazarov, *Topological transconductance quantization in a four-terminal Josephson junction*, Phys. Rev. **B95**, 075417 (2017).

[17] Y. V. Nazarov and Y. M. Blanter, *Quantum Transport* (Cambridge University Press, Cambridge, 2009).

[18] J. S. Meyer and M. Houzet, *Non-trivial Chern numbers in three-terminal Josephson junctions*, Phys. Rev. Lett. **119**, 136807 (2017).

[19] D. V. Averin and K. K. Likharev, *Coulomb blockade of single electron tunneling, and coherent oscillations in small tunnel junctions*, J. Low. Temp. Phys. **62**, 345 (1986).

[20] A. I. Larkin, K. K. Likharev, and Yu. N. Ovchinnikov, *Secondary quantum macroscopic effects in weak superconductivity*, Physica **126B**, 414 (1984).

[21] A. H. Castro Neto, F. Guinea, N. M. R. Peres, K. S. Novoselov, and A. K. Geim, *The electronic properties of graphene*, Rev. Mod. Phys. **81**, 109 (2009).

[22] P. Miró, M. Audiffred, and T. Heine, *An atlas of two-dimensional materials*, Chem. Soc. Rev. **43**, 6537 (2014).

[23] E. Kogan and V. U. Nazarov, *Symmetry classification of energy bands in graphene*, Phys. Rev. B **85**, 115418 (2012).

[24] Q. A/S, *Band structure of 2d graphene*, `https://quantumwise.com/documents/tutorials/latest/BasicGrapheneTutorial/index.html/chap.graphene_bandstructure.html`.

[25] L. Zhang, P. Bampoulis, A. N. Rudenko, Q. Yao, A. van Houselt, B. Poelsema, M. I. Katsnelson, and H. J. W. Zandvliet, *Structural and electronic properties of germanene on* MoS_2, Phys. Rev. Lett. **116**, 256804 (2016).

[26] D. Grassano, O. Pulci, A. M. Conte, and F. Bechstedt, *Validity of Weyl fermion picture for transition metals monopnictides TaAs, TaP, NbAs, and NbP from ab initio studies*, Sci. Rep. **8**, 3534 (2018).

[27] J. Buckeridge, D. Jevdokimovs, C. R. A. Catlow, and A. A. Sokol, *Bulk electronic, elastic, structural, and dielectric properties of the Weyl semimetal TaAs*, Phys. Rev. B **93**, 125205 (2016).

[28] C.-C. Lee, S.-Y. Xu, S.-M. Huang, D. S. Sanchez, I. Belopolski, G. Chang, G. Bian, N. Alidoust, H. Zheng, M. Neupane, *et al.*, *Fermi surface interconnectivity and topology in Weyl fermion semimetals TaAs, TaP, NbAs, and NbP*, Phys. Rev. B **92**, 235104 (2015).

[29] R. S. Knox, *Polarons and Excitons in Polar Semiconductors and Ionic Crystals* (Academic, N.Y., 1963) pp. 271–292.

[30] R. Loudon, *Theory of non-linear optical processes in semiconductors and insulators*, Proc. Phys. Soc. Lond. **80**, 952 (1962).

[31] L. Ju, L. Wang, T. Cao, T. Taniguchi, K. Watanabe, S. G. Louie, F. Rana, J. Park, J. Hone, F. Wang, *et al.*, *Tunable excitons in bilayer graphene*, Science **358**, 907 (2017).

[32] P. Zanardi and M. Rasetti, *Holonomic quantum computation*, Physics Letters A **264**, 94 (1999).

[33] J. Pachos, P. Zanardi, and M. Rasetti, *Non-Abelian Berry connections for quantum computation*, Phys. Rev. A **61**, 010305 (1999).

[34] P. Solinas, P. Zanardi, and N. Zanghì, *Robustness of non-Abelian holonomic quantum gates against parametric noise*, Phys. Rev. A **79**, 042316 (2004).

[35] E. Sjöqvist, *Trend: A new phase in quantum computation*, Physics **1**, 35 (2008).

[36] V. Lahtinen and J. Pachos, *A short introduction to topological quantum computation*, SciPost Physics **3**, 021 (2017).

[37] C. Janvier, L. Tosi, L. Bretheau, Ç. Ö. Girit, M. Stern, P. Bertet, P. Joyez, D. Vion, D. Esteve, M. F. Goffman, H. Pothier, and C. Urbina, *Coherent manipulation of andreev states in superconducting atomic contacts*, Science **349**, 1199 (2015).

3

HOLONOMIC QUANTUM MANIPULATION IN THE WEYL DISK

It has been shown that a Weyl point in a superconducting nanostructure may give rise to a Weyl disk where two quantum states are almost degenerate in a 2D manifold in the parametric space. This opens up the possibility of a holonomic quantum manipulation: a transformation of the wave function upon adiabatic change of the parameters within the degenerate manifold. In this paper, we investigate in detail the opportunities for holonomic manipulation in Weyl disks.

We compute the connection at the manifold in quasiclassical approximation to show it is Abelian and can be used for a phase gate. To provide a closed example of quantum manipulation that includes a state preparation and read-out, we augment the holonomic gate with a change of parameters that brings the system out of the degenerate subspace. For numerical illustrations, we use a finite value of quasiclassical parameter and exact quantum dynamics. We investigate the fidelity of an example gate for different execution times.

This chapter is submitted to PRB as Victor Boogers, **Janis Erdmanis**, Yuli Nazarov, *Holonomic quantum manipulation in the Weyl Disk*, https://arxiv.org/abs/2107.04814 (2021). For numerical code and data see https://doi.org/10.5281/zenodo.5089041

3.1. INTRODUCTION

A quantum computer promises unprecedented advantage over classical one for a set of challenging problems like protein folding [1] and prime number factorization [2]. However, building it is a challenge since it is necessary to isolate a set of quantum states from the environment as well as to manipulate it within the same environment. A particular obstacle is a decoherence whereby the states pick up the fluctuations of the environment, which adds stochastic dynamical phases and may induce dissipation [3, 4].

An alternative way to meet the challenge is the quantum manipulation within degenerate subspaces that have gained considerable interest nowadays [5–7]. The resonant manipulation that can be applied in the most systems with well-separated energy levels, does not work for degenerate subspaces. Instead, the manipulation is performed within a degenerate manifold: a set of parameters within which the states are degenerate and distinct. An adiabatic change of parameters in time along a trajectory within this manifold corresponds to a unitary operator in the degenerate subspace, that depends on the trajectory rather then on the way it is traversed. Such mapping of a trajectory to a unitary operator for manifold is often characterized with a connection that sets how a wavefunction defined at a point is transported to other points in an infinitesimally small neighbourhood. An important property of a connection is the holonomy: a property that transporting a vector over different trajectories with the same starting point and destination results in different vectors. This is the manifestation of either curvature of the connection or a singularity that separates the trajectories into topological classes, so that the transportation results differ only if two trajectories belong to different classes.

In quantum mechanics, the connection is characterized by a gauge potential [8], and the unitary operators correspond to the path integrals involving the potential. They are called holonomic transformations. The advantage of using these transformations for wave function manipulation is that in adiabatic limit the result is determined by the trajectory only, rather then by details of the time dependence of the parameter evolution along the trajectory. This provides the robustness against parametric noise and other decoherence sources.

In quantum mechanics, the connection of a manifold can be either Abelian or non-Abelian. The Abelian connection has been studied by Berry [9] while Wilczek and Zee [8] addressed the general non-Abelian case specific for degenerate manifolds. In general, a holonomic transformation is assigned to any curve in the Hilbert manifold. The tasformations have been studied in the context of geometric phase [10], and nonadiabatic geometric computation [11–19]. For an Abelian connection, the unitary operators representing all trajectories with the same endpoints can be simultaneously diagonalized. Such diagonalization is not possible for a non-Abelian connection, and thus holonomy is irreducible. This in principle permits an implementation of a complete set of quantum gates to achieve universal holonomic quantum computation in a variety of systems [20]. However, the experimental realization of these schemes appeared difficult due to long execution times required to get rid of non-adiabatic corrections [11, 21, 22].

A particular example of holonomic manipulation involves a two-dimensional system of indistinguishable anyons. Changing the positions of the anyons provides a connection with a vanishing curvature [23]. The holonomic transformations are the same for all trajectories from the same homotopy class specified by number of windings around the anyons. This sets the paradigm of topological quantum computation [24]. Within the paradigm, a quantum manipulation is implemented as a braiding, a move of anyons along the trajectories whereby all anyons return to starting points making loops around each other. The holonomic transformations in this case are robust against the fluctuations of the trajectory shapes, this promises to implement manipulations of an exceptional fidelity [25]. These opportunities have raised interest in anyonic excitations in solid-state systems such as Majorana superconductor-semiconductor nanowires [26] and specific fractional quantum Hall effect setups [27, 28].

Many quantum systems exhibit topologically protected energy-level crossings in three-dimensional parameter space that are commonly called Weyl points [29]. In solid-state physics, the parameter space is a space of wave vectors confined to a Brillion zone of the crystal lattice. The Weyl points in solid-state band structures are a subject of active theoretical and experimental research [30]. Another realization of Weyl points concerns a multi-terminal superconducting nanostructure, where the Weyl points appear as the crossings of mirror-symmetric Andreev bond states at zero energy [31] in the parametric space of three independent superconducting phases.

It has been shown recently that the interaction effects can cause a substantial modification of Weyl points [32]. A generic interaction model combines soft confinement and fluctuations in the parameter space. In the quasiclassical limit, a *Weyl disk* is formed in the vicinity of a point: two quantum states are (almost) degenerate in a finite two-dimensional region of the three-dimensional parameter space. The residual level splitting is exponentially small in the quasiclassical parameter. This makes the degeneracy physically achievable for a variety of systems. For instance, in a multi-terminal superconducting junction, the Weyl disk can be realized by placing large inductances between each superconductor terminal and the nanostructure. This makes the phase differences at the nanostructure softly constrained by the phase differences at the terminals.

The degenerate manifold at Weyl disk may be used for holonomic quantum manipulation. We explore this opportunity in the present Article. Using the quasiclassical approximation, we compute the connection at the Weyl disk to show it is Abelian. A corresponding quantum gate (Fig. 3.1 a) is thus a phase gate in a proper basis. We show the relation of the phase shift and the Berry phase from the classic example of 1/2 spin in magnetic field [9]. To demonstrate richer opportunities for quantum manipulation, we augment the purely holonomic transformations by adiabatic passages to the exterior of the disk. (Fig. 3.1 b) We show that the crossing of the disk boundary corresponds to a Hadamard gate. With this, we provide a closed example of quantum manipulation that incudes an initialization in a superposition state, holonomic manipulation, and subsequent readout. The crossings of the disk boundary can occur in different points as well (Fig. 3.1 c). The resulting gates are equivalent if a trajectory in the disk is closed along the boundary of the disk (cf. Fig. 3.1 c and d). We investigate the work of these quantum gates beyond adiabatic approximation with a full numerical simulation at a finite and moderate value of the quasiclassical parameter. We evaluate the gate fidelity as functio n of execution time and provide analysis of the dominant nonadiabatic corrections.

The paper is organized as follows. In Section 3.2 we provide a Hamiltonian description a multiterminal superconducting junction with a Weyl point and discuss the soft constraints that enable the Weyl disk regime. In Section 3.3 we consider the Weyl disk

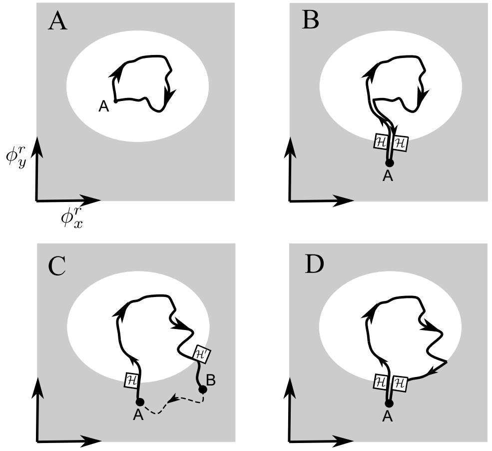

Figure 3.1: A Weyl disk (shown in white) is a 2D elliptic region in the parametric space where two quantum states are degenerate. A. A purely holonomic transformation is achieved by adiabatic change of parameters along a closed trajectory. B. To achieve more functionality, we consider adiabatic passages beyond the degenerate maniold. A Hadamard gate describes the crossing of the disk boundary. C. The crossings of the boundary do not have to be in the same point. D. The gate from (C) is equivalent to the gate where the trajectory in the disk is closed along the disk boundary.

manifold in quasiclassical approximation and supplement it with a numerical example at a finite and moderate quasiclassical parameter. The Section 3.4 is separated into subsections where we (A) recall the concept of holonomic transformations, (B)compute the connection in the quasiclassical limit, (C) consider the adiabatic passages beyond the disk, (D) evaluate the connection beyond the quasiclassical limit. In Section 3.5 we analyze the deviations from adiabatic approximation, and present the results of the full quantum dynamics simulation evaluating the fidelity of the swap gate as function of the gate execution time. We conclude in the Section 3.6.

3.2. THE SYSTEM

Weyl points in various physical systems have been a subject of an active research [29, 30, 33]. An important property of a Weyl point is its topological protection: the conservation of topological charge guarantees that small perturbations of the system just shift rather than destoy the point and associated conical singularity in energy spectrum.

Recently it was shown [31] that multiterminal superconducting junctions with the leads of ordinary topologically trivial material can host Weyl points. In other words, the lowest in energy Andreev bound state (ABS) can be tuned to zero energy (Fig. 3.2). The tuning parameters are the superconducting phases of the terminals. Owing to gauge invariance, only phase differences between terminals matter and thus at least four terminals are required to achieve Weyl points.

The Hamiltonian describing the conical spectrum in the vicinity of a Weyl point is a

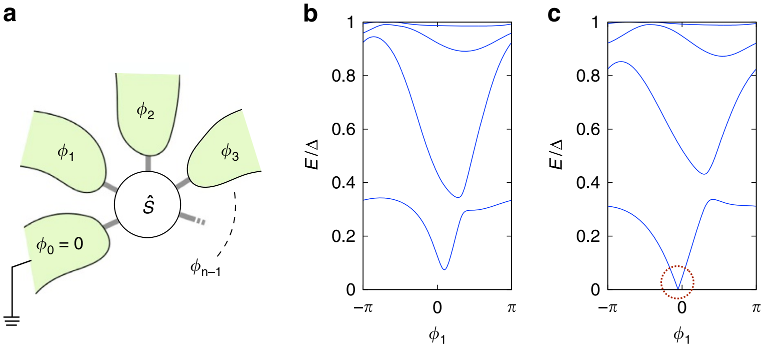

Figure 3.2: (Ref. [31]) *Left*: Multiterminal superconducting junction with superconducting phases ϕ_n. *Middle*: The Andreev bound state spectrum as a function of one of the supeconductor terminal phases ϕ_1 with the other phases at general settings. *Right*: The same spectrum for the choice of the other phases corresponding to a Weyl point.

2×2 matrix in the basis of two singlet degenerate ground states of the nanostructure [34],

$$H_{WP} = (\hbar/2e) \sum_{n=x,y,z} I_n \phi_n \hat{\sigma}_n. \tag{3.1}$$

here, $\hat{\sigma}_n$ are the Pauli matrices in the space of the singlet states, ϕ_n are the superconducting phases counted from the positions, and I_n are the coefficients defining the energy slopes of the spectrum. The corresponding energy levels are $E = \pm(\hbar/2e)\sqrt{\sum_n I_n^2 \phi_n^2}$.

In a realistic setup, the multiterminal superconducting junction is embedded in a linear circuit (Fig. 3.3), and thus the phases determining the Weyl point become dynamical variables rather than parameters, $\phi_n \to \hat{\phi}_n$, and can deviate from the external phases ϕ_n^r that play the role of parameters now. The linear circuit yet constrains softly the $\hat{\phi}_n$ to ϕ_n^r.

The constraint in general can be implemented as a quadratic addition to the energy. In particular, for our setup this is an inductive energy: each inductance L_n adds a term $(\hbar/2e)^2(\hat{\phi}_n - \phi_n^r)^2/2L_n$ constraining the corresponding phase. The quantum fluctuations of the phase around this point are determined by the corresponding capacitance of the system that produces charging energy $(2e\hat{N}_n)^2/2C_n$, $\hat{N}_n$ being a variable canonically conjugated to $\hat{\phi}_n$. The full Hamiltonian of the system with a soft constraint reads:

$$H(\vec{\phi}^r) = H_{WP} + \left(\frac{\hbar}{2e}\right)^2 \sum_n \frac{(\hat{\phi}_n - \phi_n^r)^2}{2L_n} + \sum_n \frac{(2e\hat{N}_n)^2}{2C_n} \tag{3.2}$$

where the middle term accounts for the soft constraint and the last term for the fluctuations. This is a minimum model of the embedding linear circuit, more complex models involve general frequency-dependent response functions of the circuit and do not change the qualitative conclusions.

The relevant scales in this Hamilonian can be understood when considering a single-dimension version of it,

$$H(\phi^r) = (\hbar/2e) I \phi \hat{\sigma}_z + \left(\frac{\hbar}{2e}\right)^2 \frac{(\hat{\phi} - \phi_n^r)^2}{2L} + \frac{(2e\hat{N})^2}{2C} \tag{3.3}$$

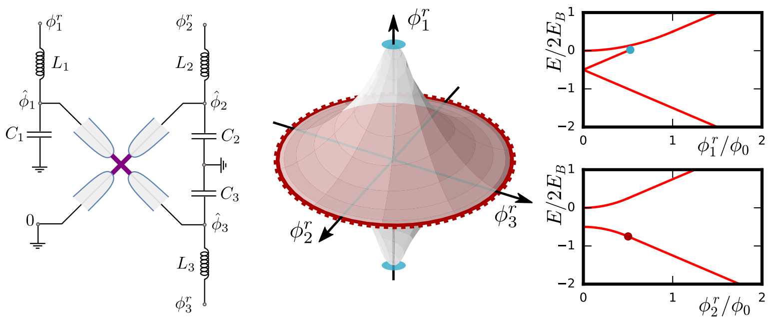

Figure 3.3: (Ref. [32]). Formation of the Weyl disk. *Left*: A four-terminal Josephson junction embedded in a linear circuit. The linear circuit represents the finite capacitances and inductances of the superconducting leads and the surrounding electromagnetic environment. *Middle* The 3D region where the two minima of quasiclassical potential are present. The two minima are of the same energy at a 2D region shown in red: the Weyl disk. *Right*: The energy spectrum along a line perpendicular to the disk (upper panel) and one in the disc plane (lower panel). In upper panel, the energies of two lowest minima split upon increasing the distance from the disk plane. In lower panel, two minima are degenerate and merge in one at the disk edge (red dot in the plot).

The diagonalization of this Hamiltonian is trivial since the quasi-spin and ϕ separate and we have an oscillator centered at the positions that depend on the eigenvalue of spin $\sigma = \pm 1$, $\phi = \phi^r - \sigma\phi_0$, $\phi_0 \equiv 2eIL/\hbar$. At $\phi^r = 0$ these two positions correspond to degenerate minina separated by energy barrier $E_B = LI^2/2$. The energy spectrum is given by (m being the number of quanta in the oscillator)

$$E_{m,\sigma} = \hbar\omega(m + 1/2) + \frac{\hbar}{2e} I\phi^r\sigma - E_B. \tag{3.4}$$

where $\omega = \sqrt{LC}$ is the oscillator frequency.

We assess the significance of quantum fluctuations by comparing the barrier height and the energy quantum in the oscillator. We introduce a quasiclassical parameter:

$$Q = \frac{E_B}{\hbar\omega} = \frac{1}{2}\left(\frac{LIe}{\hbar}\right)^2 \frac{\hbar}{e^2 Z}, \tag{3.5}$$

$Z = \sqrt{L/C}$ being the characteristic impedance of the oscillator. Since $Ze^2/\hbar \simeq 10^{-2}$ for typical circuits, the parameter can be large even for relatively small inductances. If $Q \gg 1$, the system is in the quasiclassical regime and the overlap of the states in two minima is exponentially small. In the opposite limit $Q \ll 1$ the overlap is big and the effect of soft confinement can be treated perturbatively.

We see that for one-dimensional version of the Hamiltonian the energy levels retain conical singularity as far as its dependence on $\vec{\phi}^r$ is concerned. Generally, one expects this to hold for 3D case as well: the confinement would just renormalize the "velocities" $\partial E/\partial\phi_n$ defining the singularity. It has been discovered in [32] that there is an important exception from this general rule: for one of the directions — we will call it an easy axis and take it for z direction — the velocity remains finite while vanishing in the limit of large $Q$for two perpendicular direction. The easy direction is defined by the biggest energy barrier: $E_B^z \equiv L^z I_z/2 > E_B^x, E_B^y$.

Thereby a Weyl point in the presence of confinement and in the quasiclassical limit becomes a Weyl disk (see Fig. 3.3): two energy levels remain degenerate within an ellipse in the $\phi_x^r - \phi_y^r$ plane, the semiaxes being given by $(n = x, y)$

$$A_n = \frac{4e}{\hbar I_n}(E_B^z - E_B^n). \tag{3.6}$$

This is related to the existence of two potential minima in the vicinity of the Weyl point corresponding to two spin directions. In quasiclassical approximation, the corresponding wavefunctions do not overlap being localized near the minima.

It has been shown that the residual level splitting is exponentially small in the quasiclassical parameter. The approximate degeneracy in the Weyl disk is potentially interesting for quantum manipilation: that could allow a superposition of two degenerate states to evolve in time very slowly and enables holomorphic manupulations of this superposition by changing ϕ_x^r, ϕ_y^r along a trajectory. In the next Section, we will discuss in detail the properties of the states at the Weyl disk.

3.3. PROPERTIES OF THE STATES AT THE WEYL DISK

In this Section, we complete and expand the analysis of the quantum states at the Weyl disk that was started in Ref. [32]. We present the numerical results and compare with the analytical ones in the quasiclassical limit. This analysis is crucial for understanding the available holonomic transformations and other manipulations at the manifold.

Let us first consider a numerical illustration (Fig. 3.4). We choose a moderate value of the quasiclassical parameter $Q = E_B^z/\hbar\omega_z = 5$ in the Hamiltonian (3.2). The barriers in x, y directions are lower and equal, $E_B^{x,y}/E_B = 1/3$. The corresponding oscillator frequencies are also the same, $\hbar\omega^{x,y} = E_B^{x,y}$, this suggest the circular symmetry of the setup with respect to rotations about z. The effective Q in this direction is thus $\simeq 1$. We will use this set of parameters for all numerical illustrations in the paper, since it proves the feasibility of holonomic manipulations at moderate values of the quasiclassical parameter.

In the left pane and inset of the Figure, we present the energies of the four lowest states. We will perform quantum manipulations in the basis of the two lowest states. As we will see later in dynamical simulations, the wave function from this basis mostly leaks to the 3rd and 4th state.

In the left pane, we plot the energies versus ϕ_x^r at $\phi_{z,y}^r = 0$, that is, in the disk plane. The energies of the two lowest states are apparently degenerate up to $\phi_x^r \simeq 0.5A_x$. Deep in quasiclassical limit, they remain degenerate up to $\phi_x^r = A_x$. The moderate value of Q results in the residual splitting that becomes comparable with the energy distance between the 3rd and the 2nd state at the edge of the disk.

It is important for further consideration to note a symmetry of the Hamiltonian at this choice of the parameters: it is invariant with respect to 180° rotation about x-axis. Owing two this, the splitting is diagonal in the basis of odd and even states with respect to the rotation. The 1st and the 4th state are even, while the 2nd and 3rd are odd.

If we change the phase in easy direction, ϕ_z^r, the degeneracy is immediately lifted (inset of the Figure), the splitting being proportional to ϕ_z^r. An instructive picture to

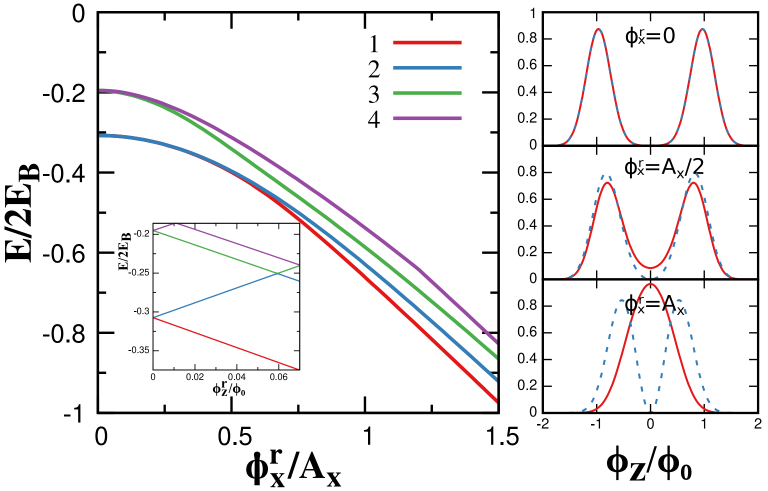

Figure 3.4: Numerical results for the energy spectrum and wave functions. For numerical illustrations in this Article, we choose a moderate value of the quasiclassical parameter $Q = E_B/\hbar\omega_z = 5$. ($E_B \equiv E_B^z$). Other parameters are $\hbar\omega_{x,y}/E_B = 1/3$, $E_B^{x,y}/E_B = 1/3$. Left pane: Four lowest energy levels of the Hamiltonian 3.2 in the disk plane $\phi_z^r = 0$ versus ϕ_x^r. The two lowest levels are degenerate deep in the disk. In the limit $Q \to \infty$ the degeneracy persists till the disk edge $(\phi_x^r)^2/A_x^2 + (\phi_y^r)^2/A_y^2 = 1$ with $A_{x,y}$ given by Eq. 3.6. Since $Q = 5$ is taken, the residual splitting at the disk edge is already comparable with $\omega_{x,y,z}$ which defines the energy distance to the higher levels. However, the splitting is not visible at $\phi_x^r < 0.5A_x$. Inset: Four lowest energy levels versus ϕ_z^r at $\phi_{x,y} = 0$. The splitting is lifted upon a shift ϕ_z^r in the easy direction and is proportional to the shift. Right pane: The probability density of ϕ_z, $p(\phi_z) = \sum_\sigma \int |\Psi_\sigma|^2 d\phi_x d\phi_y$ in the disk plane for even (solid line) and odd (dashed line) lowest energy states at several values of ϕ_x^r. The probability deep in the disk separates in two almost non-overlapping peaks corresponding to two degenerate minima in the effective potential. At the edge of the disk, the minima merge resulting in a single peak.

comprehend this is that of a two-well potential depending on ϕ_z. The energies of the distinct potential minima are aligned in the disk plane and are shifted by ϕ_z^r in opposite directions. The distance between the mimima reaches maximim at the center of the disk and decreases upon moving to the edge of the disk where two minima merge into one. In the quasiclassical limit, the wave function is localized at the minima. This is illustrated in the right pane of the Figure where we plot the probability density $p(\phi_z)$ for even and odd state. We observe two distinct peaks at the center, slightly overlapping peaks at $\phi_x^r \simeq 0.5A_x$ and a single peak at the disk edge.

To characterize the double-well potential, we resort to quasiclassical approximation. If we neglect the quantum fluctuations completely, the quantum states are localized in superconducting phase space. The states can be decomposed as follows:

$$|\Psi\rangle = |\vec{\phi}\rangle \otimes |S\rangle \tag{3.7}$$

where $|\vec{\phi}\rangle$ is a wave function with definite values of the superconducting phases and $|S\rangle$ is a 2-component wave function in the spin space. This decomposition allows us to determine $|S\rangle$ from the Hamiltonian (3.2). Since we are looking for the states of the minimum

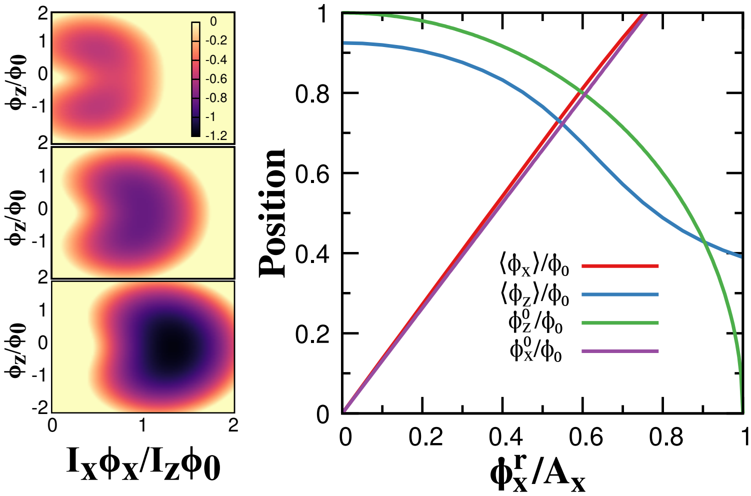

Figure 3.5: The effective potential (Eq. 3.10) and comparison with the numerical results. Left pane: colour contours of the quasiclassical effective potential in the $\phi_z - \phi_x$ plane for the parameters at the Weyl disk: $\phi^r_z, \phi^r_y = 0$ and $\phi^r_x / A_x = 0.5, 1, 1.5$ from the upper to lower plots. The minima of this double-well potential merge at the disk edge. Right pane: The locations of the potential minima $\phi^0_{x,z}$ given by Eq. 3.11 and the numerical averages $\langle \phi_{x,z} \rangle$. To compute the averages, we take the wave functions of the two lowest states and arrange their superposition corresponding to the state localized in the upper minimum. The locations and averages are in reasonable agreement even for the moderate Q chosen.

energy, we set the spin to be antiparallel to the effective "magnetic field" at the point $\vec{\phi}$,

$$\vec{W} \cdot \vec{\sigma} |S\rangle = -|S\rangle \tag{3.8}$$

$\vec{W}$ being the normalized vector in the direction of the "field",

$$W_n = \frac{I_n \phi_n}{\sqrt{\sum_n I_n^2 \hat{\phi}_n^2}}. \tag{3.9}$$

With this, we evaluate the effective potential for the state $|\psi\rangle$ averaging the Hamiltonian over the state 3.8 and neglecting the charging energy:

$$V(\vec{\phi}) = -\frac{\hbar}{2e}\sqrt{\sum_n I_n^2 \phi_n^2} + \left(\frac{\hbar}{2e}\right)^2 \sum_n \frac{(\phi_n - \phi^r_n)^2}{2L_n} \tag{3.10}$$

In Figure 3.5 (left) we plot the color contours of this effective potential in the $\phi_x - \phi_z$ plane at three values of ϕ^r_x at $\phi^r_z, \phi^r_y = 0$. We see the minima moving towards each other upon increasing of ϕ^r_x and eventually merging at $\phi^r_x = A_x$. We expect the wave functions to be localized in the minima. To check for this, we compare the positions of the quasiclassical mimima with the numerical averages $\langle \phi_{x,z} \rangle$ to find the reasonable correspondence even for the moderate Q.

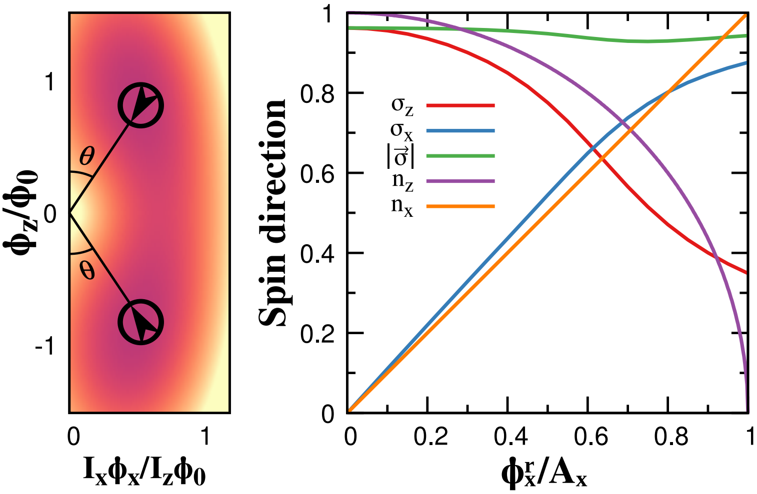

Figure 3.6: The spin directions of the localized states compared with the numerical averages. Left pane: The countours of the even wave function. The spin directions in the potential minima are shown by the arrows. We rescaled the axes by A_x, A_z so that the spin directions point towards the origin. Right pane: the quasiclassical predictions for σ_x, σ_z as compared with the numerical averages for the superposition of two lowest eigenfunctions corresponding to the localization in the upper minimum. we show the quasiclassical spin direction $\vec{n}$ with the spin direction obtained numerically. We normalize $\langle\vec{\sigma}\rangle$ to $\langle\vec{\sigma}\rangle^2 = 1$ to validate the decomposition given by Eq. 3.7. There is a good agreement even for the moderate Q taken.

The positions of the minima are given by [32]:

$$\langle\hat{\phi}_x\rangle = \frac{\phi_0 I_z}{A_x I_x}\phi^r_x \qquad \langle\hat{\phi}_y\rangle = \frac{\phi_0 I_z}{A_y I_y}\phi^r_y$$

$$\langle\hat{\phi}_z\rangle = \pm\phi_0\sqrt{1-\rho^2} \tag{3.11}$$

where $\phi_0 = (2e/\hbar)I_z L_z$, $\rho^2 = (\phi^r_x)^2/A_x^2 + (\phi^r_y)^2/A_y^2$ ($\rho^2 = 1$ corresponds to the disk edge).

The locations of the minima determine the spin of the localized states. With Eqs. 3.8 and 3.11 we evaluate the angle θ it makes with the easy direction: $\cos\theta = \pm\langle\hat{\phi}_z\rangle/\phi_0$. The spins of two localized states in the center of the disk are aligned with z and are antiparallel. At the disk we come closer to the disk boundary, the the spins align with the disk plane and are parallel. (See Fig. 3.6. The dependence of spin directions on $\vec{\phi}^r$ is essential for the holonomic transformations as discussed in the next Section. To veryfy this numerically, we compute numerically the average values of σ_x, σ_z for the superposition of the two lowest states that corresponds to the localization in the upper minimum. The results are presented in the right pane of Fig. 3.6. We see a reasonable agreement with the quasicalssical results that is expectedly gets worse near the edge of the disk where the overlap of the states localized in different minima is significant.

3.4. QUANTUM GATES

3.4.1. GEOMETRIC PHASE AND HOLOMONIC TRANSFORMATIONS

Let us recall here the basics of geometric phase and holonomic transformations. We consider a Hamiltonian $\hat{H}(\vec{x})$ that depends on a set of parameters $\vec{x}$. We change the parameters in time along a trajectory $\vec{x}(t)$, this results in the time-dependent Hamiltonian $\hat{H}(\vec{x})$. We introduce a local basis that diagonalizes $\hat{H}(\vec{x})$ in each point of parameter space,

$$E_n(\vec{x})|n\rangle = \hat{H}(\vec{x})|n\rangle \tag{3.12}$$

The Schrödinger equation in the local basis reads

$$i\hbar\dot{\psi}_n = E_n - \hbar\dot{x}_i M^i_{nm}\psi_m \tag{3.13}$$

where the effective vector potential $\hat{M}^i$

$$M^i_{nm} = -i\langle n|\partial_i(|m\rangle) \tag{3.14}$$

represents the connection of the bases. With this, an in general, the unitary transformation of the wave function can be separated into two parts [10]: the dynamical phase arising from the first term representing the time-dependent energies and a geometric phase arising from the second term that depends solely on the trajectory in the parametric space. The geometric phase is an attractive phenonemon to use in quantum information processing. There are setups where the dynamical phase can be neglected beyond the adiababic approximation. Such examples have been actively studied in the field of nonadiabatic geometric quantum manipulation [11–18]. Alternatively, the trajectory in the parameter space can be passed adiabatically. The resulting geometric phase then reduces to a holonomic phase and is a basis of actively studied holonomic quantum manipulation [6, 7].

The most common example of adiabatic manipulation is the Berry phase [9]. In this case, the energy levels are non-degenerate, and the adiabaticity implies that the frequencies associated with the parameter change are much smaller than the energy distances between the levels. One can neglect the non-diagonal elements of $\hat{M}^i$ so the Shrödinger equation reduces to

$$i\hbar\dot{\psi}_n = E_n(\vec{x}(t))\psi_n - \hbar\dot{x}_i M^i n\psi_n \tag{3.15}$$

The dymanical phase separates from geometric phase. The latter depends on the trajectory only and is given by the line integral over the trajectory, $\vec{x}_i, \vec{x}_f$ being the initial and final point of the trajectory,

$$\beta_n = \int_{\vec{x}_i}^{\vec{x}_f} \vec{M}_n \cdot d\vec{l} \tag{3.16}$$

The vector potential is not gauge invariant and changes upon a gauge transformaton $|n\rangle \rightarrow U(\vec{x})|n\rangle$, $|U|^2 = 1$,

$$M^i_n \rightarrow M^i_n + U^*\partial_i U \tag{3.17}$$

The guage-invariant Berry phase is defined for closed trajectories $\vec{x}_i = \vec{x}_f$ and, by virtue of Stoke's theorem, equals to the surface intergal of the curl of $\vec{M}$ over the surface enclosed by the trajectory.

A fascinating extension of this concept petrains the case where several levels of the Hamiltonian are degenerate in a subspace of $\vec{x}$. The adiabaticity implies that the frequencies of the change are much smaller than the energy distance between the degenerate and non-degenerate levels. The adiabatic motion along a trajectory results in a unitary transformation in the degenerate subspace $\hat{S}(\vec{x}_i, \vec{x}_f)$,

$$\hat{S} = \mathscr{P} \exp\left(i \int_{\vec{x}_i}^{\vec{x}_f} \vec{\hat{M}}(\vec{x}) \cdot d\vec{l} \right). \tag{3.18}$$

$\mathscr{P}$ stands here for the ordering of $\vec{\hat{M}}$along the trajectory. The operator vector potential is not invariant with respect to the unitary transformations of the basis, $|n\rangle \to U(\vec{x})|n\rangle$, $|U|^2 = 1$,

$$M_n^i \to \hat{U}^\dagger M_n^i \hat{U} + \hat{U}^\dagger \partial_i \hat{U}. \tag{3.19}$$

The gauge invariance is achieved for closed trajectories, and pertains the eigenvalues of $\hat{S}$.

The holonomic transformations can be Abelian and non-Abelian. They are Abelian if $\hat{M}^i(\vec{x})$ can be chosen to commute for all $\vec{x}$. As we will see soon, this will be the case under consideration. The non-Abelian connection permits to realize a universal set of quantum gates [6, 7] from holonomic transformations over different trajectories. However, the experimental implementation of them is difficult because of the nonadiabatic corrections [11, 21, 22].

3.4.2. PURE HOLONOMIC TRASFORMATION

Let us apply these general considerations to the manifold of nearly degenerate wave functions at the Weyl disk. The first step is the parametrization of the basis in the degenerate subspace. We restrict ourselfs to the deep quasiclassical limit. The natural basis choice are that of wave functions localized either in upper ($\phi_z > 0$) or lower ($\phi_z > 0$) minimum. As discussed, those can be decomposed into spin and orbital part,

$$|+\rangle = |S\rangle_+ |O\rangle_+; \; |+\rangle = |S\rangle_- |O\rangle_- \tag{3.20}$$

Here, $|O\rangle_\pm$ are the normalized wave functions in $\vec{\phi}$ space located at the minima positions $(\langle\hat{\phi}_x\rangle, \langle\hat{\phi}_y\rangle, \pm\sqrt{1-\rho^2})$ (see Eq. 3.11). The $|S\rangle_\pm$ are spinors representing the spin antiparallel to the corresponding $\vec{w}_\pm$ (see Eq. 3.9), $\vec{w}_- = (w_+^x, w_+^y, -w_+^z)$.

The best choice of the coordinates in the elliptic disk corresponds to an unambiguous mapping of (ϕ_x^r, ϕ_y^r) to the upper hermisphere of the vector $\vec{w}_+$. The two parametirzing angles θ, α, $0 < \theta < \pi/2, -\pi < \alpha < \pi$ are determined from

$$\sin\theta = \rho; \; e^{i\alpha} = \left(\frac{\phi_x^r}{A_x} + i \frac{\phi_y^r}{A_y} \right) \rho^{-1}; \tag{3.21}$$

while $\vec{w}_+ = (\cos\alpha \sin\theta, \sin\alpha \sin\theta, \cos\theta)$.

It is essential to choose $|S\rangle_\pm$ to insure the continuity over the hemishere and the absence of singularity. This is achieved by setting

$$|S\rangle_+ = \begin{bmatrix} -e^{-i\alpha} \sin\frac{\theta}{2} \\ \cos\frac{\theta}{2} \end{bmatrix}; \; |S\rangle_- = \begin{bmatrix} \cos\frac{\theta}{2} \\ -e^{i\alpha} \sin\frac{\theta}{2} \end{bmatrix}. \tag{3.22}$$

We compute the connection from Eq. 3.14. We may neglect the overlap between $|O\rangle_+$ and $|O\rangle_-$ in the quasiclassical limit, so the connection is diagonal in this basis and therefore Abelian. Moreover, the derivatives of $|O\rangle_\pm$ with respect to θ, α may be neglected as well. They give rise to the quantities proportional to the expectation values of the momentum and angular momentum for these states, those are zero since the states are localized. The connection is thus determined by the derivatives of $|S\rangle_+$ and reads:

$$\hat{M}^\alpha = -\hat{\tau}_z \sin^2\frac{\theta}{2};\ \hat{M}^\theta = 0 \tag{3.23}$$

Thereby we reduce the situation to the classic example of Berry phase for an electron spin in spin magnetic field of constant amplitude [9]. Any holonomic transformation has a form of $\exp(-i\tau_z\beta)$. This is a phase gate, whereby the states $|\pm\rangle$ acquire opposite phase shifts $\mp\beta$, β being the Berry phase from the example. For any closed trajectory, β is thus the half of a solid angle enclosed by the trajectory on the hemisphere,

$$\beta = \oint \mathrm{curl}\vec{M} dS = \frac{1}{2}\oint \sin\theta d\theta d\alpha. \tag{3.24}$$

In original coordinates, the connection and the curl read as follows:

$$M^x = \frac{\phi_y^r}{\rho^2 A_y A_x}(1-\sqrt{1-\rho^2}) \tag{3.25}$$

$$M^y = -\frac{\phi_x^r}{\rho^2 A_y A_x}(1-\sqrt{1-\rho^2}) \tag{3.26}$$

$$\mathrm{curl}\vec{M} = \frac{1}{2A_x A_y\sqrt{1-\rho^2}} \tag{3.27}$$

We will consider the deviations due to finite Q in the Subsection D. In the next Subsection, we will present quantum gates that enable measuring of the result of holonomic transformations.

3.4.3. BEYOND THE DISK

The initialization and measurement of a quantum state at the degenerate manifold is questionable if ever possible in principle. To check if holonomic transformations work as supposed, we need to extend the quantum manipilation schemes. A simple way to achieve this would be to depart from the disk in easy direction. This leads to energy splitting $|\pm\rangle$ and enables the measurement in this basis. However, with this measurement one cannot characterise the work of the phase gate predicted, since it does not alter the probabilities to be in $|\pm\rangle$. Besides, the states almost do not overlap: this makes it difficult to arrange their superposition. We need to do something different.

We propose to augment the purely holonomic transformations in the disk with adiabatic passages in the same plane that go beyond the degenerate manifold. (Fig. 3.1) This will bring us to the basis of the ground and first excited states that is continuous an unambiguous in the exterior of the disk. The adiabatic passages in the exterior change the phase difference between these basis states (mostly this is the effect of dynamical phase) not affecting the probabilities. Since the states are distinguishable (e.g. they correspond to different currents in the superconducting leads given by energy derivatives with respect to $\vec{\phi}$), these propabilities can be measured. Such measurements can be done with Andreev bound state spectroscopy[35–37]. The resonant quantum manipulation is also possible since the energies are spilt and the wave functions of the states overlap.

Let us find how the wave function is transformed between the interior and exterior bases upon crossing the disk boundary in the point $\theta = \pi/2, \alpha = \alpha_0$. We consider a transformation $R(\alpha_0)$: 180° rotation about the axis $(\cos\alpha_0, \sin\alpha_0, 0)$that is in the direction of the spin-orientation vectors $\vec{w}_\pm$ at this point. For a circular-symmetric disk $L_x = L_y, I_x = I_y, C_x = C_y$ this is a true symmetry transformation of the Hamiltonian. For an anisotropic disk, this symmetry holds approximately in quasiclassical limit where the wave functions are concentrated near a point in $\vec{\phi}$ space.

The transformation should be diagonal in exterior basis. The ground and excited state are respectively even and odd upon $R(\alpha_0)$. As to the interior states, let us note that $|0\rangle_\pm = R(\alpha_0)|0\rangle_\mp$, so that

$$R(\alpha_0)|\pm\rangle = e^{\mp i\alpha_0}|\mp\rangle \tag{3.28}$$

With this, we find that the wave functions in exterior and interior bases are related by a generalized Hadamard gate

$$\mathscr{H}(\alpha_0) \equiv \frac{1}{\sqrt{2}} \begin{bmatrix} 1 & e^{i\alpha_0} \\ e^{-i\alpha_0} & -1 \end{bmatrix} \tag{3.29}$$

Since $\mathscr{H}^2 = 1$, the same matrix relates the bases upon the reverse passage.

Let us consider the quantum gate given in Fig. 3.1 b. We initialize the wave function in a point A beyond the disk: we can wait for the relaxation that brings the system to the ground state. After this, we can bring it to a superposition of the ground and excited state with a pulse of an oscillating $\vec{\phi}$ with the frequency matching the level splitting in this point. The adiabatic trajectory enters the disk, makes a loop there for a holonimic manipulation, and returns to the same point. The resulting quantum gate reads

$$\hat{S} = \mathscr{H}(\alpha_0) e^{i\tau_z\beta} \mathscr{H}(\alpha_0) \tag{3.30}$$

β being the Berry phase accumulated on the loop. This does not include the phase shifts in the exterior basis that do not change the probability. If we start in the ground/excited state, we end up in the excited/ground state with the probability

$$\mathscr{T} = \sin^2\beta \tag{3.31}$$

Measuring these probabilities thus permits the characterization of the holonomic transformation. The answer for the probability, as expected, does not depend on the entrance point α_0.

To measure the wave function in the exterior basis, one does not have to return to the initial point (Fig. 3.1 c): the measurement can be performed upon leaving the disk at some other point $(\pi/2, \alpha_1)$. The resulting quantum gate upon the phase factors in exterior basis is given by

$$\hat{S} = \mathscr{H}(\alpha_0) e^{-i\tau_z\beta} \mathscr{H}(\alpha_1) \tag{3.32}$$

so the probability $\mathcal{T} = \sin^2(\beta^* + (\alpha_1 - \alpha_0)/2)$, β^* being the Berry phase acquired upon the part of the trajectory that connects the entrance and exit points. One may be surprised with the fact that β^* in principle is not guage invariant quantity. This is resolved if we note that in our gauge $(\alpha_1 - \alpha_0)/2$ is the Berry phase acquired upon a passage along the disk boundary from α_1 to α_0. So the gate in Fig. 3.1 c is equivalent to that in Fig. 3.1 d where the trajectory in the disk is closed. This restores the guage-invariant expression $\mathcal{T} = \sin^2\beta$, β being the Berry phase accumulated along the closed trajectory.

More sophisticated gates can be arranged by entering and leaving the disk repeatedly along an adiabatic passage. They are composed of Hadamard gates, holomonic phase shifts in interior basis and dynamical phase shifts in exterior basis.

3.4.4. CONNECTION BEYOND THE QUASICLASSICAL LIMIT

The simple expression for holonimic transformation obtained above is valid in the deep quasiclassical limit only and relies on the localization of the wave functions. One may wonder how accurate it is at finite values of Q. At first site, this problem is superfluous since finite values of Q give rise to the splitting of degenerate values in the disk, this formally invalidates the holonomic transformation. However, the splitting is exponentially small and may be neglected when the deviations from the deep quasiclassical limit are noticeable.

To investigate and illustrate this, in this Subsection we compute numerically the connection at finite Q. We restrict ourselves to a simple particular case when this computation is straightforward: we concentrate on the circular trajectories at a circular-symmetric disk.

The circular symmetry of the disk implies $I_{x,y} = I_r$, $L_{x,y} = L_r$, $C_{x,y} = C_r$. Let us concentrate on a family of the Hamiltonians $\hat{H}(\alpha)$ along a circular trajectory $\phi^r_x = r\cos\alpha, \phi^r_y = r\sin\alpha$, r being the radius. This family is obtained by rotations about z axis by α,

$$\hat{H}(\alpha) = R_z^{-1}(\alpha)\hat{H}R_z(\alpha); \tag{3.33}$$

where

$$R_z(\alpha) = \exp(-i\alpha\hat{J}_z) \tag{3.34}$$

and $\hat{J}_z$ is the angular momentum operator. R_z^α represent rotation around easy direction with an angle α. The rotation thus generates the family of the bases diagonalizing $\hat{H}(\alpha)$:

$$|n\rangle_\alpha = \exp(-i\alpha\hat{J}_z)|n\rangle_\alpha \tag{3.35}$$

The connection $\hat{M}^\alpha$ is thus determined through the matrix elements of $\hat{J}_z$ (see Eq. 3.14), is constant over the trajectory. One needs to diagonalize the Hamiltonian only once per trajectory to compute the connection.

We project $\hat{J}_z$ on the two lowest eigenstates $|e\rangle$,$|g\rangle$, of the Hamiltonian,

$$M^\alpha_{ab} = \langle a|\hat{J}_z|b\rangle \tag{3.36}$$

$a, b = g, e$.The half-difference of the eigenvalues of this matrix defines the holomic transformation phase accumulated over the circular trajectory $\beta = \pi(M_+ - M_))$.

One needs to take into account that the einvalues of $\hat{J}_z$ are half-integer and the basis given by Eq. 3.35 is discontinious. Owing to this, a formal calculation would give $\beta = \pi$

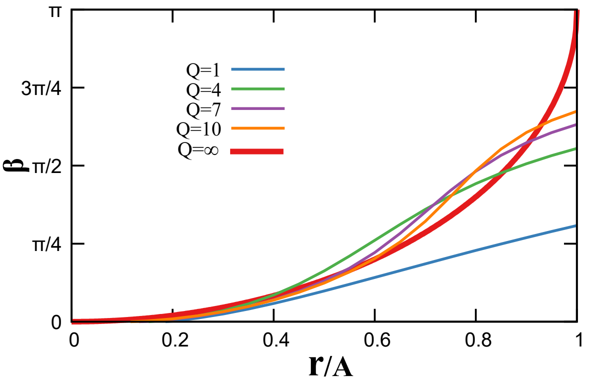

Figure 3.7: Holonomic phase at various finite values of Q for a circular trajectory of radius r at the circular-symmetric disk. We compare it with the quasiclassical result (Eq.3.37) in the limit $Q \to \infty$.

even at $r \to 0$ where no change of the Hamiltonian takes place. So one has to subtract π to make sure $\beta \to 0$ at $r \to 0$.

The results are plotted in Fig. 3.7. In the deep quasiclassical limit, the angular momentum operator can be replaced with $\sigma_z/2$ and the holonomic phase is given by

$$\beta = \pi \frac{1 - \langle \hat{\sigma}_z \rangle}{2} = \pi \left(1 - \sqrt{1 - (r/A)^2} \right), \tag{3.37}$$

A being the disk radius. We observe significant corrections to the quasiclassical limit at finite Q, those become bigger at the disk boundary and at the smaller Q. However, the overall dependence of $\beta(r)$ is preserved even at $Q = 4$.

3.5. QUANTUM DYNAMIC

In this Section, we discuss the deviations from the ideal results of the execution of the quantum gates described. The deviations come from the residual level splitting in the disk and from the non-adiabatic excitations to higher levels in the course of the execution at finite time. We illustrate these sources with the numerical examples of the quantum dynamics of the full Hamiltonian (3.2). The parameters of the Hamiltonian used for illustrations are the same as in the previous Sections corresponding to the moderate quasiclassical parameter Q and circular symmetry. We show that the gates work well even in this case.

We concentrate on the gate of the type given in Fig. 3.1c. We chose a simple family of the trajectories (Fig. 3.8) consisting of two straight passages ("arms") in radial direction and an arc around the origin. The initial and final points A, B are beyond the disk at the same distance $R > A$ from the origin, A being the disk radius. The radius and the angle of the arc are r, Θ respectively. We expect the holonomic phase β to accumulate upon the passage:

$$\beta = \frac{1}{2} \Theta \sqrt{1 - \left(\frac{r}{A} \right)^2}. \tag{3.38}$$

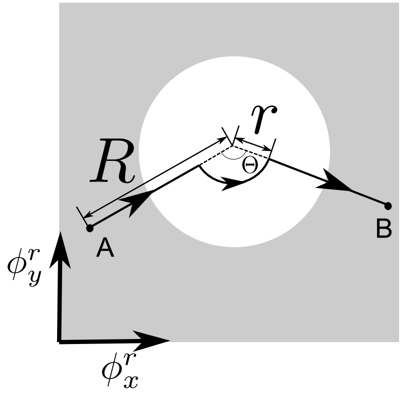

Figure 3.8: The concrete example trajectories investigated in Section 3.5.

The time dependence of $\vec{\phi}^r$ at the trajectory can be defined in terms of the angular velocity Ω at the arc part and the linear velocity $v \equiv A\dot{\rho}$ The overall execution time of the gate is thus $T = \Theta/\Omega + 2(R-r)/v$. In a realistic manipulation, it is easy to make these velocities time-dependent preserving the total execution time, this might be a possibility to reduce the non-adiabatic corrections and thus improve the gate performance. However, the qualitative analysis made and our attempts of such optimization did not show any substantial improvement. The optimal time dependence of the velocities is close to constant.

We consider the deviations at the arc part and at the arms separately, and conclude by combining both in an example of the gate fidelity versus the execution time T.

The Schrödinger equation at the arc part is best expressed in the local basis (3.35),

$$i\hbar\dot{\psi}_n = E_n\psi_n - \hbar\Omega(t)J^z_{nm}\psi_m \tag{3.39}$$

the effective Hamiltonian not depending on time if $\Omega(t) = \text{const}$. The initial condition corresponds to the wave function localized in the two lowest levels, $\psi_{1,2} \neq 0$, and the equation needs to be solved at the time interval $(0, \Theta/\Omega)$.

The first source of the deviations is the residual level splitting $E_2 - E_1$. The proper work of the holonomic gate requires this splitting to be smaller than the second term $\propto \Omega$, that is, $|E_2 - E_1| \ll \hbar\Omega$. If this condition is fulfilled, the deviations in probabilities are proportional to $((E_2 - E_1)/\hbar\Omega)^2$.

The second source are the non-adiabatic corrections corresponding to the excitations to higher levels $n > 2$. The probabilities of the excitations from the states $|1\rangle, |2\rangle$ can be estimated as

$$P_{1,2\to n} \approx |\langle n|\hat{J}_z|1,2\rangle|^2 \left(\frac{\hbar\Omega}{E_n - E_{1,2}}\right)^2 \tag{3.40}$$

The small probabilities thus require $\hbar\Omega \ll |E_n - E_{1,2}| \simeq \hbar\omega_{x,y,z}$. The execution time thus should be

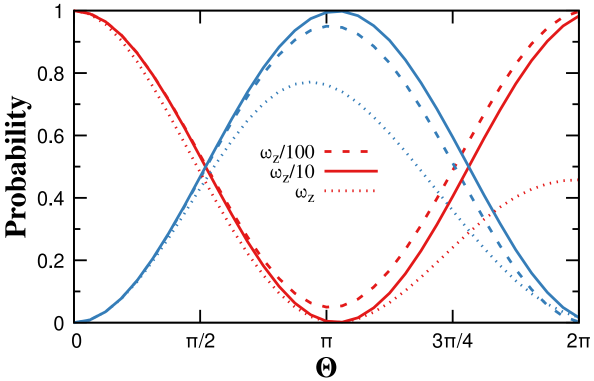

Figure 3.9: The deviations coming from the arc part. We assume the ideal work at the arms of the trajectory. The initial state is an excited state $|2\rangle$ in the exterior basis. We plot the probabilities $P_{1,2}$ (blue and red) versus Θ at three different angular velocities $\Omega = 10^{-3}, 10^{-2}, 10^{-1}\omega_z$ (dashed, solid and dotted lines). At the intermediate Ω, the results coincide with those for the ideal gate upon numerical accuracy. At the smallest Ω, the deviations are due to the residual level splitting in the disk interior. At the highest Ω, the deviations are due to non-adiabatic excitiation to the higher levels.

We illustrate this with the quantum dynamics simulation at the arc part of the trajectory. (Fig. reffig:arc). We simulate the work of the gate assuming its ideal execution at the arms. The initial state corresponds to the excited state in the exterior basis at the point A. We compute the probabilities $P_{1,2}$ to end up in the ground/excited state at the point B. For an ideal gate, those are given by $P_{1,2} = \sin^2\beta, \cos^2\beta$.

We plot the probabilities versus Θ for three different angular velocities $\Omega = 10^{-2}, 10^{-1}, 10^{0}\omega_z$. We choose $r = 0.25$ where the residual splitting $E_2 - E_1 = 0.002\omega_z$. At the smallest Ω, the deviation owing to the residual splitting is noticeable. There is no excitation to the higher levels, so that $P_1 + P_2 = 1$. At the intermediate Ω, the results follow those of the ideal gate with the numerical accuracy. The probabilities achieve minimum/maximum at $\Theta \approx \pi 1.03$ corresponding to $\beta = \pi/2$. At the highest Ω, the non-adiabatic correction become noticeable. The probability progressively leaks to higher levels, with only a half of it remaining in the computational subspace for the longest gate $\Theta = 2\pi$. Despite the significant deviations, the curves at the lowest and at the highest angular velocity still follow the oscillatory pattern. This demonstrates that the gate works in a wide range of the angular velocities.

Let us analyse the deviations coming from the radial arms of the trajectory. The residual splitting in this case only modifies the phase factor in the exterior basis and can be disregarded. To quantify the non-adiabatic corrections, we represent the Schrödinger equation in the instantaneous basis $H(t)|n(t)\rangle = E(t)|n(t)\rangle$ and compute the probabilities to be in the excited states $n > 2$ in the second order perturbation theory in terms of the non-diagonal elements of $\partial H \partial t$.

Owing to circular symmetry, the results do not depend on the direction of the arm. We can compute the amplitudes for the motion in x direction with the velocity depending on the actual value of ϕ^r_x, $\dot{\phi}^r_x(\phi^r_x)$ The amplitude in the excited state n accumulated in the

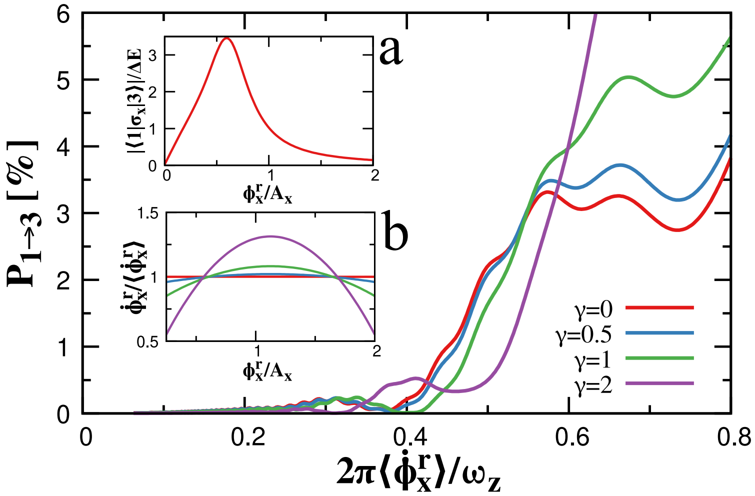

Figure 3.10: The deviations coming from the radial part of the trajectory. The probability of the dominant excitation $P_{1\to3}$. For this examle, the trajectory starts at $r = 0.25A$ and ends at $R = 2A$. a. The intensity of the matrix element energizing the transition versus the distance from the origin ϕ_x^r. b. The velocity profiles corresponding to Eq. 3.42. The curves correspond to various γ shown in the labels. Main figure: we plot the probability for various velocity profiles (γ is shown in the curve labels) as function of the average velocity. The probabilities are lower than 0.005 for lower velocities $< 0.06A\omega_z$ and increase rapidly at higher velocities. The slowest growth corresponds to the constant velocity profile $\gamma = 0$.

course of motion from r to R then reads:

$$\psi_n(R) = -\frac{\hbar I_x}{2e}\int_r^R ds_2 \frac{|\langle n(s_2)|\sigma_x|a(s_2)\rangle|}{E_n(s_2)-E_a(s_2)} \times \exp\left[\frac{i}{\hbar}\int_r^{s_2}\frac{1}{\dot{\phi}_x^r(s_1)}(E_n(s_1)-E_a(s_1))ds_1\right] \quad (3.41)$$

where $|a\rangle$ is a state from the computational subspace, either ground one or excited one.

To evaluate this integral numerically, we use instantaneous eigenstates obtained by diagonalization of the Hamiltonian at various ϕ_x^r. We summarize the results in Fig. 3.10 where we present the probability $1 \to 3$ versus the average velocity at the arm. The non-diagonal matrix element energizing the transition is plotted versus ϕ_x^r in Fig. 3.10 a. We try a family of ϕ_x^r dependencies of this velocity parametrized by γ:

$$\frac{\dot{\phi}_x^r(\phi_x^r)}{\langle\dot{\phi}_x^r\rangle} = \frac{\gamma}{2\tanh(\gamma/2)}(1-\rho^2\tanh^2(\gamma/2)) \quad (3.42)$$

where $\rho = (2\phi_x^r - R - r)/(R-r)$. These velocity profiles are plotted in Fig. 3.10 b for several values of γ. In the main Figure, we plot the excitation probability versus the average velocity for several γ. The overall dependence is qualitatively consistent with exponential suppression of the transitions at low velocities, $\ln P \simeq v^{-1}$. The detailed dependence is not smooth, the probabilities oscillate showing interference due to finite length of the arm. At all velocity profiles checked, the probabilities are $< 5\cdot10^3$ for $\dot{\phi}_x^r \approx A\omega_z/4\pi$ and

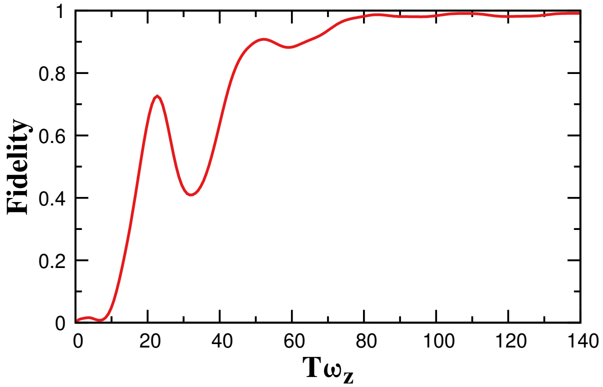

Figure 3.11: The fidelity of the holonomic swap gate as function of the execution time T. The gate corresponds to the trajectory with $r = 0.25A$, $R = 2A$, $\Theta = \pi$ and is executed with constant velocity along the trajectory.

grow rapidly at higher velocities. We find that the time-independent velocity profile $\gamma = 0$ eventually provides smaller probabilities and is thus advantageous for the gate design.

We illustrate the deviations on all parts of the trajectory by computing the fidelity of the swap gate versus the execution time. (Fig. 3.11). A swap gate implements the transformation $|1\rangle \to |2\rangle; |2\rangle \to |1\rangle$ in the exterior basis, that is, $\mathcal{T} = \infty$. The actual example differs a bit from the swap gate: the trajectory parameters are $r = 0.25A$, $R = 2A$, $\Theta = \pi$, this corresponds to $\beta \approx 1.5209$ that differs slightly from the swap gate value of $\pi/2$. However, $\mathcal{T} \approx 0.9975$ for this value of β so the difference with the ideal swap gate is negligible. The velocity in $\phi_x^r - \phi_y^r$ is constant along all parts of the trajectory. The fidelity is almost zero at $T\omega_z < 10$, increases non-monotonically till $T\omega_z < 80$ and is close to ideal value at bigger T. We thus expect the gate to work good at $T\omega_z \simeq 100$ and longer. This looks parametrically bigger than a naive ad-hoc estimation $T\omega_z \simeq 1$. However, we have to take into account that the typical energy differences along the path are $\simeq 0.2\omega_z$ and the better estimation for time is a period rather than the inverse frequency. So that $T\omega_z \simeq 100$ corresponds to $3-4$ typical oscillation periods. Eventually, this corresponds to the number of peaks seen in the time dependence of the fidelity.

In the figure, we show a full numerical simulation of the swap gate for different runtimes. As expected from small runtimes, the execution is diabatic and thus all state probabilities after execution are close to zero. On the other hand, at long runtime limit, we see that the gate is relatively stable a desirable property for holonomic computation.

3.6. Conclusions

In conclusion, we have investigated holonomic manipulations that can be performed utilizing approximate degeneracy at the Weyl disk: a rather counter-intuitive example of 2D finite degenerate manifold in 3D parameter space. The Weyl disks can be realized by soft confinement of parameters in the superconducting nanostructures hosting the Weyl points in the spectrum of Andreev bound states, which is the example considered here. The resulting Hamiltonian is however generic and can be realized in many quantum systems with the Weyl like crossings in the spectrum of discrete energy states, so our results are of general nature.

We have computed the connection in the Weyl disk manifold in quasi-classical limit and found it Abelian: it realizes a phase gate, the phase difference being related to the Berry phase in its classic example. This may seem a rather discouraging result. However, we propose to augment the purely holonomic transformations with the adiabatic passages beyond the degenerate manifold. With this, we can propose the realization of more sophisticated gates and practical measurement of the results of the holonomic transformations.

We did quantum dynamic simulation of the gates proposed for realistic Hamiltonians and find they can work properly at rather short execution times. We did not consider decoherence in this respect: the point is that our exemplary setup provides no projection against the fluctuations of the parameter along the easy axis that can cause the decoherence in the degenerate 2D subspace.

A natural continuation of this research line would include the consideration of several Weyl points brought into soft confinement and interaction with each other. They would give rise to degenerate manifolds of higher dimensions with richer holonomic transformations and perhaps provide the protection against decoherence.

To support open science and open software initiatives and to comply with institutional policies, we have published all relevant code and instructions for running it on the Zenodo repository [38].

REFERENCES

[1] D. Wecker, B. Bauer, B. K. Clark, M. B. Hastings, and M. Troyer, *Gate-count estimates for performing quantum chemistry on small quantum computers*, Physical Review A **90**, 022305 (2014).

[2] P. W. Shor, *Polynomial-time algorithms for prime factorization and discrete logarithms on a quantum computer*, SIAM Review **41**, 303 (1999).

[3] C. H. Bennett and D. P. DiVincenzo, *Quantum information and computation*, Nature **404**, 247 (2000).

[4] M. A. Nielsen and I. L. Chuang, *Quantum computation and quantum information*, in *Quantum computation and quantum information* (Cambridge University Press, Cambridge, 2009).

[5] P. Zanardi and M. Rasetti, *Holonomic quantum computation*, Physics Letters A **264**, 94 (1999).

[6] A. C. M. Carollo and V. Vedral, *Holonomic quantum computation*, in *Holonomic Quantum Computation* (Wiley, 2016) pp. 475–482.

[7] L.-A. Wu, P. Zanardi, and D. A. Lidar, *Holonomic quantum computation in decoherence-free subspaces*, Physical Review Letters **95**, 130501 (2005).

[8] F. Wilczek and A. Zee, *Appearance of gauge structure in simple dynamical systems*, Physical Review Letters **52**, 2111 (1984).

[9] M. V. Berry, *Quantal phase factors accompanying adiabatic changes*, Proceedings of the Royal Society of London. A. Mathematical and Physical Sciences **392**, 45 (1984).

[10] Y. Aharonov and J. Anandan, *Phase change during a cyclic quantum evolution*, Physical Review Letters **58**, 1593 (1987).

[11] E. Sjöqvist, D. M. Tong, L. M. Andersson, B. Hessmo, M. Johansson, and K. Singh, *Non-adiabatic holonomic quantum computation*, New Journal of Physics **14**, 103035 (2012).

[12] R. Leone, *On the parallel transport in quantum mechanics with an application to three-state systems*, arXiv: Mathematical Physics (2019).

[13] A. A. A. Jr, J. M. Fink, K. Juliusson, M. Pechal, S. Berger, A. Wallraff, and S. Filipp, *Experimental realization of non-abelian non-adiabatic geometric gates*, Nature **496**, 482 (2013).

[14] S. E. Economou and T. L. Reinecke, *Theory of fast optical spin rotation in a quantum dot based on geometric phases and trapped states*, Physical Review Letters **99**, 217401 (2007).

[15] H. Li, Y. Liu, and G. Long, *Experimental realization of single-shot nonadiabatic holonomic gates in nuclear spins*, Science China Physics, Mechanics & Astronomy **60**, 60 (2017).

[16] S.-L. Zhu and Z. D. Wang, *Implementation of universal quantum gates based on nonadiabatic geometric phases*, Physical Review Letters **89**, 097902 (2002).

[17] K. Nagata, K. Kuramitani, Y. Sekiguchi, and H. Kosaka, *Universal holonomic quantum gates over geometric spin qubits with polarised microwaves*, Nature Communications **9**, 9 (2018).

[18] L.-M. Duan, *Geometric manipulation of trapped ions for quantum computation*, Science **292**, 1695 (2001).

[19] P. Solinas, P. Zanardi, N. Zanghì, and F. Rossi, *Semiconductor-based geometrical quantum gates*, Physical Review B **67**, 121307 (2003).

[20] L. Faoro, J. Siewert, and R. Fazio, *Non-abelian holonomies, charge pumping, and quantum computation with josephson junctions*, Physical Review Letters **90**, 028301 (2003).

[21] D. Parodi, M. Sassetti, P. Solinas, P. Zanardi, and N. Zanghì, *Fidelity optimization for holonomic quantum gates in dissipative environments*, Physical Review A **73**, 052304 (2006).

[22] K. Toyoda, K. Uchida, A. Noguchi, S. Haze, and S. Urabe, *Realization of holonomic single-qubit operations*, Physical Review A **87**, 052307 (2013).

[23] J. M. Leinaas and J. Myrheim, *On the theory of identical particles*, Il Nuovo Cimento B Series 11 **37**, 1 (1977).

[24] A. Y. Kitaev, *Fault-tolerant quantum computation by anyons*, Annals of Physics **303**, 2 (2003).

[25] G. P. Collins, *Computing with quantum knots*, Scientific American **294**, 56 (2006).

[26] J. D. Bommer, H. Zhang, Önder Gül, B. Nijholt, M. Wimmer, F. N. Rybakov, J. Garaud, D. Rodic, E. Babaev, M. Troyer, D. Car, S. R. Plissard, E. P. Bakkers, K. Watanabe, T. Taniguchi, and L. P. Kouwenhoven, *Spin-orbit protection of induced superconductivity in majorana nanowires*, Physical Review Letters **122**, 187702 (2019).

[27] D. E. Feldman, *The smallest particle collider*, Science **368**, 131 (2020).

[28] J. Nakamura, S. Liang, G. C. Gardner, and M. J. Manfra, *Direct observation of anyonic braiding statistics*, Nature Physics **16**, 931 (2020).

[29] C. Herring, *Accidental degeneracy in the energy bands of crystals*, Physical Review **52**, 365 (1937).

[30] B. Yau and C. Felser, *Topological materials: Weyl semimetals*, Annu. Rev. Condensed Matter Phys. **2017.8**, 337 (2017).

[31] R.-P. Riwar, M. Houzet, J. S. Meyer, and Y. V. Nazarov, *Multi-terminal josephson junctions as topological matter*, Nature Communications **7**, 11167 (2016).

[32] J. Erdmanis, A. Lukacs, and Y. V. Nazarov, *Weyl discs: theoretical prediction – Supplementary material*, (2018).

[33] T. O'brien, *Applications of topology to weyl semimetals and quantum computing*, (2019).

[34] T. Yokoyama and Y. V. Nazarov, *Singularities in the andreev spectrum of a multiterminal josephson junction*, Physical Review B **92**, 155437 (2015).

[35] A. Zazunov, V. S. Shumeiko, E. N. Bratus', J. Lantz, and G. Wendin, *Andreev level qubit*, Physical Review Letters **90**, 087003 (2003).

[36] S. Shafranjuk, I. Nevirkovets, and J. Ketterson, *A qubit device based on manipulations of andreev bound states in double-barrier josephson junctions*, Solid State Communications **121**, 457 (2002).

[37] C. Janvier, L. Tosi, L. Bretheau, Ç. Ö. Girit, M. Stern, P. Bertet, P. Joyez, D. Vion, D. Esteve, M. F. Goffman, H. Pothier, and C. Urbina, *Coherent manipulation of andreev states in superconducting atomic contacts*, Science **349**, 1199 (2015).

[38] J. Erdmanis, *See for code used for the numerical calculations.* (2021).

4

DRASTIC EFFECT OF WEAK INTERACTION NEAR SPECIAL POINTS

A generic semiclassical superconducting nanostructure connected to multiple superconducting terminals hosts a quasi-continuous spectrum of Andreev states. The spectrum is sensitive to the superconducting phases of the terminals. It can be either gapped or gapless depending on the point in the multi-dimensional parametric space of these phases. Special points in this space correspond to setting some terminals to the phase 0 and the rest to the phase of π. For a generic nanostructure, three distint spectra come together in the vicinity of a special point: two gapped phases of different topology and a gapless phase separating the two by virtue of topological protection.

In this paper, we show that a weak interaction manifesting as quantum fluctuations of superconducting phases drastically changes the spectrum in a narrow vicinity of a special point. We develop an interaction model and derive a universal generic quantum action that describes this situation. The action is complicatesd incorporating a non-local in time matrix order parameter, and its full analysis is beyond the scope of the present paper. Here, we identify and address two limits: the semiclassical one and the quantum one, concentrating on the first-order interaction correction in the last case.

In both cases, we find that the interaction squeezes the domain of the gapless phase in the narrow vicinity of the point so the gapped phases tend to contact each other immediately defying the topological protection. We identify the domains of strong coupling where the perturbation theory does not work. In the gapless phase, we find the logarithmic divergence of the first-order corrections. This leads us to an interesting hypothesis: weak interaction might induce an exponentially small gap in the formerly gapless phase.

This chapter is submitted to PRB as **Janis Erdmanis**, Árpád Lukács, Yuli Nazarov, *Drastic effect of weak interaction near special points in semiclassical multiterminal superconducting nanostructures*, https://arxiv.org/abs/2107.14105 (2021). For supplementary code see https://zenodo.org/record/5146125.

4.1. INTRODUCTION

Superconducting nanostructures and nanodevices are in focus of the condensed matter research community for almost six decades starting from the discovery of Josephson effect [1]. Quantum properties of Josephson-based devices enable sophisticated quantum information technologies [2–4]. The practical realization of the topological quantum computing paradigm [5] is seen in semiconductor-superconductor nanowire-based nanostructures hosting Majorana states [6, 7]. The superconducting nanostructures vary much in material realization, size, and properties yet can be universally understood in terms of the spectrum of Andreev bound states that depends on phase difference between the superconducting electrodes [8, 9]. There are well-established theoretical tools for analysis and prediction of this spectrum [8, 9]. In this paper, we concentrate on the semiclassical nanostructures with a typical size that is larger then the electron wave length. They involve many transport channels so that their dimensionless (in units of conductance quantum $G_Q \equiv e^2/\pi\hbar$)conductance $g \gg 1$. The Andreev spectrum is quasi-continuous with a small level spacing $\Delta/g \ll \Delta$, Δ being the superconducting energy gap.

Most superconducting nanostructures have two terminals like Josephson junctions do. In recent years, there is a considerable increase of interest to multi-terminal superconducting nanostructures, both from theoretical [10–22] and experimental [23–27], side. Partly, this interest was provoked by the idea that the Andreev levels in N-terminal nanostructures simulate a bandstructure of (N-1)-dimensional material, including its topological properties, and the prediction of quantized transconductance.[13, 17] Much research addresses the Weyl points that appear for $N \geq 4$ as topological singularities in the parameter space. [15, 16, 22, 28–30]

As to semiclassical nanostructures, it has been discovered that, in distinction from most two-terminal ones, the quasi-continuous spectrum may be gapped or gapless depending on a point on parameter space [11]. It has been recognized that the gapped phases in a semiclassical structure can be classified with topological numbers [31, 32]. In this case, the presence of gapless phase is readily understood: the domains of the gapless phase should separate the domains of gapped phases of incompatible topology. That has been confirmed experimentally [31, 32]. An extensive investigation of various topologies of this kind is presented in Ref. [33].

It has been shown that in a wide class of the nanostructures two phases of distinct topology come together in a special point being separated by a domain of gapless phase that becomes infinitesimally thin at the point but yet provides the topological protection [19]. (Fig. 4.1 a). Each multi-terminal nanostructure can be made effectively two-terminal by setting all terminals to two distinct values of the phase. A special point in N-dimensional parameter space occurs when these phases are 0 and π, that is, the nanostructure is spanned between the opposite values of superconducting order parameter. There are $2^{N-1}-1$ distinct special points in a N-terminal nanostructure. It has been also shown [19] that for the nanostructures containing tunnel barriers the topological protection may cease so that the domains of topologically distinct phases can come to direct contact: The topological protection is removed in the course of a protection-unprotection transition (PUT). In this paper, we concentrate on a close vicinity of a special point and consider the effect of weak interaction. We prove that even a weak interaction provides a drastic effect on the spectrum of Andreev bound states and other characteristics of the nanostructure at a certain scale in

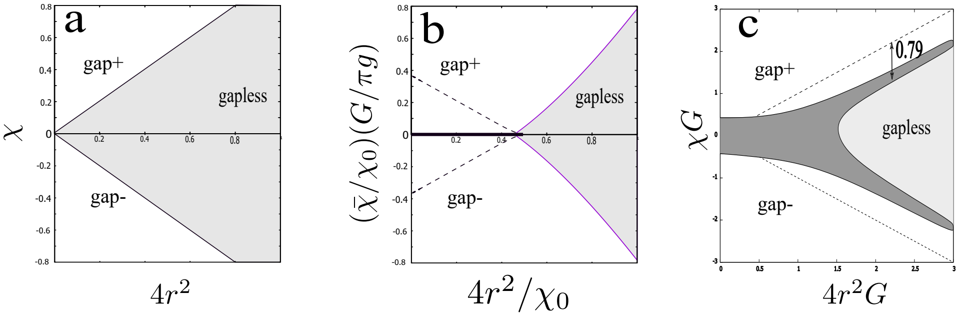

Figure 4.1: The effect of weak interaction in the vicinity of special point is drastic on a small interaction-defined scale. Diagrams are in parameter space coordinates, χ is in the direction of main axis, r is the distance from the special point in perpendicular direction. a. No interaction. Two gapped phases of distinct topologies separated by the gapless phase. b. Interaction, semiclassical limit. First-order transition (thick line) between gapped phases. Dashed lines bound the domain of metastable states. The gappless phase domain is squeezed and shifted from the point. c. Interaction, quantum limit. The gapless phase domain is squeezed, the transition lines are shifted (as indicated by arrow). Dark grey: the domain of strong coupling where the pertubation theory is not applicable.

parameter space that is determined by interaction and is small if the interaction is weak. We develop an interaction model that encompasses soft confinement and quantum fluctuations in parameter space. Importantly, we derive a universal effective action that provides the adequate description of the situation. The action is compact consisting of four terms only. However, it is hard to analyse involving a non-local order parameter depending on two times, eventually, a matrix in this space. The value of the action is obtained by minimization over this order parameter.

Owing to this complexity, we are not able to provide in this paper the complete analysis of the action. However, we identify and address two limits: the semi-classical one where the quantum fluctuations do not play a crucial role and the opposite and more interesting limit where the modification of the spectrum is due to quantum fluctuations of the most relevant phase. In the semiclassical limit, we get the exact phase diagram. In the quantum limit, we derive and analyse the first-order quantum correction that permits to draw qualitative conclusions about the phase diagram and formulate two interesting hypotheses.

Let us already here shortly present the main results obtained (Fig. 4.1). The phase diagram without interaction is given in Fig. 4.1 a. It gives the domains of the gapped and gapless phase in N-dimensional parametric space in the vicinity of the point. There is a single axis - main axis - in this space that is orthogonal to the $N-1$-dimensional separation plane between the phases. There is an approximate axial symmetry at the point so $2d$ plot suffucies to present this phase diagram: The coordinate $\xi$is along the main axis while r gives the distance from the special point in all $N-1$ dimensions orthogonal to the main axis. As promised, we see in the Figure two phases of distinct topology separated by a domain of the gapless phase thinning out at the point.

The interaction is characterized by a dimensionless conductance $G \gg g$, weaker interaction corresponding to larger G. The semiclassical limit of the action holds for $G \gg g \gg G/\ln G$. A new exponentially small scale of χ emerges, $\chi_0 = \exp(-G/g)$. The resulting phase diagram at this scale is presented in Fig. 4.1 b. We see that the two gapped phases are separated by a first order transition at sufficiently small r, and the gap remains finite at the point. The domain of the gapless phase is squeezed and shifted from the point. This implies the absence of topological protection like in the tunnel-junction nanostructures discussed in [19].

Fig. 4.1 c presents the results in the quantum limit where $g \ll G/\ln G$. We also see the squeezing of the gapless domain: its boundaries are shifted by the value of $1/G$ in vertical direction. This defines a new small scale of χ. The blacked region in the Figure gives the domain of strong coupling where the perturbation theory does not work: at the boundaries between the gapless and gapped phases and around the special point. We also find that in the gapless phase the first-order correction logarithmically diverges at small energies.

This inspires us to put forward two hypotheses that should be proved or disproved in the course of further analysis of the strong coupling case. The first hypothesis is that there is no gapless phase and topological protection in the vicinity of the special point: we draw this from continuity with the semiclassical limit. The second hypothesis is motivated by the logarithmic divergence. The divergence may lead to the formation of the interaction-induced exponentially small *gap* in the gapless phase. In this way, the gapped-gapless boundaries are crossovers rather than transitions, and the gapless phase is formally an artefact of the non-interacting approximation.

The structure of the paper is as follows. In Section 4.2 we introduce and motivate the interaction model in use. We will sketch the derivation of the total action from the quantum circuit theory in Section 4.3. In Section 4.4 we will give several representations of the resulting universal action, discuss the scales and define the limits. In Section 4.5 we shortly summarize the results for the spectrum near the special point in the absence of interaction. We study the quasiclassical limit in Section 4.6. More interesting quantum limit is considered in Section 4.7 where we address the first-order interaction corrections. We elaborate on a simplified action that describes the gapped-gapless phase transition in Section 4.8. In Section 4.9 we formulate hypotheses to be confirmed in the course of future research and finally conclude.

4.2. INTERACTION MODEL

In superconducting nanostructures, the electromagnetic interaction is usually manifested and described as quantum fluctuations of superconducting phase. [8, 34] The scale of the fluctuations is determined by a typical impedance Z of the electromagnetic environment, $\langle(\Delta\phi)^2\rangle \simeq G_Q Z$. A usual estimation for this impedance is the impedance of free space, with this $\langle(\Delta\phi)^2\rangle \simeq \alpha$, α being the fine structure constant. This is why the electromagnetic interaction in superconducting nanostructures is usually weak and therefore irrelevant.

Thus motivated, we set the interaction model by embedding the nanostructure into a linear circuit (Fig. 4.2). The phases of the superconducting terminals are allowed to fluctuate while the circuit *softly confines* these values to time-independent $\bar{\varphi}_i$ that play the role of external parameters set in the experiment. We employ Matsubara temperature technique (see e.g. [35]), so the phases at the terminals are the functions of imaginary time, $\varphi_i(\tau)$, and the partition function is a path integral over these functions ($\hbar = 1$ in our

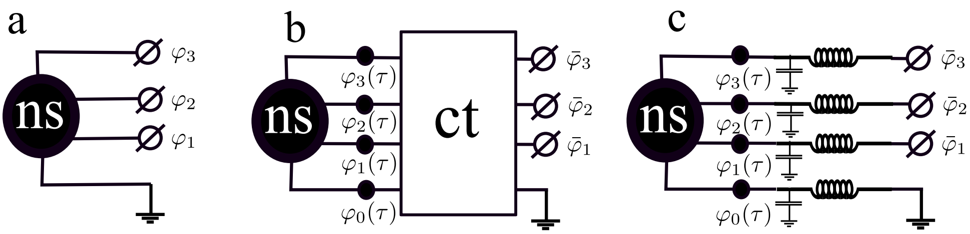

Figure 4.2: Interaction model in use. a. A multi-ternimal nanostructure biased by ideal superconducting terminals with the phases $0, \varphi_{1-3}$. b. Embedding it to a linear circuit makes the terminal phases subject to fluctuations,$\varphi_{0-3}(\tau)$, and provides the interaction. The circuit confines these quantum variables to $0, \bar\varphi_{1-3}$. c. At low freqencies/energies, the curcuit can be presented with inductances and capacitances. Crossinductances(capacitances) are not shown.

system of units),

$$Z = \int \prod_{i,\tau} d\varphi_i(\tau) e^{-\mathscr{S}}; \tag{4.1}$$

$$\mathscr{S} = \mathscr{S}_{\text{ns}}(\{\varphi_i(\tau)\}) + \mathscr{S}_{\text{ct}}(\{\varphi_i(\tau) - \bar\varphi_i\}); \tag{4.2}$$

$$\mathscr{S}_{\text{ct}} = \frac{1}{2} \int d\tau d\tau' A_{ij}(\tau - \tau') \delta\varphi_i(\tau) \delta\varphi_j(\tau') \tag{4.3}$$

where $A_{ij}(\tau)$ is related to the frequency-dependent admittance of the embedding circuit. The circuit action thus confines the fluctuations $\delta\varphi_i(\tau) \equiv \varphi_i(\tau) - \bar\varphi_i$We are interested in low frequencies where the circuit action is readily expressed in terms of the inverse conductance and capacitance matrices of the circuit,

$$\mathscr{S}_{\text{ct}} = \int d\tau \left(\frac{\hbar^2}{4e^2} (\check{L})^{-1}_{ij} \delta\varphi_i(\tau) \delta\varphi_j(\tau) + \frac{4e^2}{\hbar^2} C_{ij} \dot\varphi_i(\tau) \dot\varphi_j(\tau) \right), \tag{4.4}$$

where we denote with "check" the matrices in the space of the terminals. We have implemented a very similar model to describe interaction effect on Weyl points in superconducting nanostructures [28].

For a generic point in the parameter space one expects a smooth dependence of the nanostructure action on $\varphi_i(\tau)$ so it can be expanded up to the second order in $\delta\varphi^i$,

$$\mathscr{S}_{\text{ns}} = \mathscr{S}^{(0)}_{\text{ns}} + + \frac{\hbar}{2ek_BT} I_i \delta\varphi^i + \frac{1}{2} \sum_\omega A^{ij}_{\text{ns}}(\omega) \delta\varphi_\omega \delta\varphi_{-\omega}. \tag{4.5}$$

The first-order derivatives are proportional to the superconducting currents I_i in the terminals while the second-order terms are related to the frequency-dependent admittance of the nanostructure. Combining this with the circuit action, we readily obtain two rather trivial and dull corrections to the total action. One is classical and accounts for inductive energy induced by the nanostructure currents in the external circuit,

$$\delta\mathscr{S}_{cl} = \frac{1}{2} I_i I_j L_{ij} \tag{4.6}$$

Another one is the renormalization of the nanostructure action by the quantum fluctuations

$$\delta\mathscr{S}_q = \frac{1}{2}\sum_{\omega} A^{ij}_{\mathrm{ns}}(\omega)\langle\langle\delta\varphi^i_\omega\delta\varphi^j_{-\omega}\rangle\rangle, \tag{4.7}$$

with

$$\langle\langle\delta\varphi^i_\omega\delta\varphi^j_{-\omega}\rangle\rangle = \frac{4e^2}{\hbar^2}\left[\check{L}^{-1}+\omega^2\check{C}\right]^{-1}_{ij} \tag{4.8}$$

For estimations, it is instructive to take the superconductive energy scale and represent $\frac{\hbar^2}{4e^2}(\check{L})^{-1} \simeq G\Delta$, $G \gg 1$ can be regarded as dimensionless conductance characterizing the external circuit rather than the nanostructure. With this, the action of the nanostructure is estimated as $g\Delta$, the relative semiclassical correction as g/G, and the relative quantum correction as $1/G$. The interaction is weak provided $G \gg g \gg 1$.

In a special point, the properties of the nanostructure can be drastically changed by a small variation of the phases and the expansion (4.5) does not make sense. In the next Section, we will address the derivation of the appropriate action $\mathscr{S}_{\mathrm{ns}}$ in the vicinity of the special point.

4.3. DERIVATION OF THE ACTION NEAR A SPECIAL POINT

In general, the nanostructure action is computed from the Nambu-structured electron Green functions $\hat{G}(\tau,\tau';\mathbf{r},\mathbf{r})$ defined in each point $\mathbf{r}$ of the structure that are subject to time-dependent superconducting order parameters $\Delta_i e^{i\varphi_i(t)}$ in the adjacent superconducting leads. We will use the method of quantum circuit theory [8] which is a finite-element approximation to the actual coordinate-dependent Green functions that is suitable for semiclassical nanostructures. The line of derivation is similar to that of [19] yet it is adjusted to time-dependent fields.

4.3.1. QUANTUM CIRCUIT THEORY

In quantum circuit theory, the nanostructure is represented as a set of nodes connected by connectors: the scatterers characterized by a set of transmission coefficients T_p. In each node, the Green function is represented as a matrix $\hat{G}$ that incorporates Nambu structure and two time indices. The matrix satisfies

$$\hat{G}^2 = \hat{1} \qquad\qquad \mathrm{Tr}\,\hat{G} = 0 \tag{4.9}$$

The total action is a sum of contributions of the connectors. A contribution of a connector is expressed in terms of the Green functions at its ends, $\hat{G}_{A,B}$

$$S = \frac{1}{2}\sum_{p}\mathrm{Tr}\left\{\log\left[1+\frac{T_p}{4}\left(\hat{G}_A\hat{G}_B+\hat{G}_B\hat{G}_A-2\right)\right]\right\}. \tag{4.10}$$

Here, the trace incorporates imaginary time, $\mathrm{Tr}[A] = \int_0^\beta \mathrm{Tr}_{\mathrm{Nambu}}[A(\tau,\tau)]d\tau$, with $\beta = 1/k_B T$.

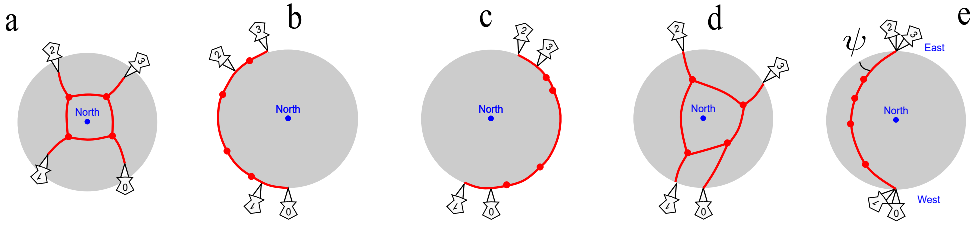

Figure 4.3: Rubber thread representation of quantum circuit theory. a. Four-terminal, four-node, eight-connector network. Finite ε, the terminals are above the equator. b. Zero energy, terminals are at the equator, the network spanned along the equator. Gapped phase. c. Gapped phase of different topology. d. Gapped phase: the nodes are spanned over the hemisphere, while the terminals are pinned at the equator. e. Special point. The terminals are located at opposite points of the sphere (West and East pole). The network is spanned along the arc, the action is degenerate with respect to ψ.

It is convenient to incorporate the information about the transmission distribution to the characteristic function of a connector $\mathscr{F}(x)$ defined as:

$$\mathscr{F}(x) = \sum_p \log\left[1 - \frac{T_p}{2}(1-x)\right] \tag{4.11}$$

where the sum is over all transmission eigenvalues. For a tunnel junction $\mathscr{F}_T(x) = -(G_T/2G_Q)(1-x)$, for a ballistic contact $\mathscr{F}_B(x) = (G_B/G_Q)\log\left[\frac{1+x}{2}\right]$ and for diffusive connector $\mathscr{F}_D(x) = (G_D/8G_Q)\,\mathrm{arccos}(x)^2$.

With this, a connector action reads

$$S = \frac{1}{2}\mathrm{Tr}\left\{\mathscr{F}((\hat{G}_A\hat{G}_B + \hat{G}_B\hat{G}_A)/2)\right\}. \tag{4.12}$$

A subset of nodes are terminals where the Green functions are fixed to (η_z is a Pauli matrix in Nambu space)

$$\hat{G}_i(\tau,\tau') = e^{-i\eta_z\varphi_i(\tau)/2} G_i^{(0)}(t-t') e^{i\eta_z\varphi_i(\tau')/2} \tag{4.13}$$

with $G_i^{(0)}$ to be given in energy representation as

$$G_i^{(0)}(\varepsilon) = \frac{1}{\sqrt{\Delta_i^2+\varepsilon^2}}\begin{bmatrix} \varepsilon & \Delta_i \\ \Delta_i & -\varepsilon \end{bmatrix} \tag{4.14}$$

Importantly, the overall action has to be minimized with respect to $\hat{G}$ in all nodes. The result of the minimization will give the actual $\mathscr{S}_{\mathrm{ns}}(\{\varphi_i(\tau)\})$.

4.3.2. RUBBER THREAD REPRESENTATION

Let us here recall the representation of the quantum circuit theory that looks naive but is in fact very instructive energizing common intuition. In this subsection, we restrict ourselves to time-independent φ_i.

In this case, the Green functions in the nodes can be minimized separately at each energy and are 2×2 Hermitian matrices to be represented with real vectors $\hat{G}(\varepsilon) \to \vec{g}\cdot\vec{\eta}$. The vectors are associated with points on a sphere, since $\hat{G}^2 = 1$ implies $\vec{g}^2 = 1$. Eventually, $\vec{g}$ are either in upper or lower hemisphere depending on the sign of ε.

The connectors are associated with rubber threads connecting the nodes, and the action with the elastic energy of the threads that depends on the angle between the vectors $\vec{g}_{A,B}$ at the ends of a thread. The elastic energy tries to bring all nodes to one point. However, the vectors $\vec{g}$ are fixed in the terminals, and the whole nanostructure is associated with a rubber thread network pinned at the terminals and spanned over the hemisphere to minimize the elastic energy (Fig. 4.3 a).

The case $\varepsilon = 0$ is special. In this case, the pins are exactly at the equator. The z-coordinate of a node is associated with the density of states at this node, the superconductivity vanishing at the North pole. Depending on the positions of the pins, the network can be either spanned over the equator (gapped phases, Fig. 4.3 b and c) or over the whole hemisphere (gapless phase, Fig. 4.3 d).

4.3.3. THE SPECIAL SYMMETRY AT A SPECIAL POINT

In general, the minimization of the action unambiguously determines $\hat{G}$ as functions of the terminal $\hat{G}_i$. However, there is an ambiguity precisely at a special point and zero energy. The rubber thread representation helps to understand why. In a special point, all pins are at precisely opposite positions at the equator: let us call them West and East poles. The network is spanned over an arc connecting the poles. Elastic energy does not fix the position of the arc given by the angle ψ (Fig. 4.3 e). There is an extra rotational symmetry about the axis that does through the poles.

We fix the Green functions of the terminals to the y axis, $\hat{G}_i = \zeta_i \eta_y$ where $\zeta_i = \pm 1$ gives if a given terminal is at the West or East pole. We parametrize the ambiguous Green functions in the nodes as follows:

$$\vec{g}_a = (-\sin\theta_a \cos\hat{\psi}, \cos\theta_a, -\sin\theta_a \sin\psi). \tag{4.15}$$

Here and in the following, we index the terminals with $i, k, l...$ and the nodes with the letters from the beginning of the alphabet: a, b, c. The total action is a sum over connectors and does not depend on ψ,

$$S = \sum_{i,a} \mathscr{F}_{ia}(\zeta_i \cos\theta_a) + \sum_{a>b} \mathscr{F}_{ab}(\cos(\theta_a - \theta_b)) \tag{4.16}$$

while θ_a are specific for a nanostructure and are determined from the minimization of above action. Here, $\mathscr{F}_{ab}$ refers to a connector connecting the nodes a and b,$\mathscr{F}_{ia}$ to a connector connecting node a and a terminal i.

Now we come to an important step: in the limit of low energies, that is relevant near a special point, the rotational angle is not a number, it can be an arbitraty matrix in two times, $\phi \to \hat{\phi} \equiv \psi(\tau, \tau')$. This matrix parametrizes the whole set of degenerate solutions for time-dependent Green functions at the special point:

$$\hat{G}_a = e^{i\eta_y \hat{\psi}/2} \begin{bmatrix} 0 & ie^{i\theta_a} \\ -ie^{-i\theta_a} & 0 \end{bmatrix} e^{-i\eta_y \hat{\psi}/2} \tag{4.17}$$

This high degeneracy, either for a number ψ or for the whole matrix $p\hat{s}i$ implies that in order to describe the situation in the vicinity of a special point, we have to consider the terms that break the special symmetry described and actually fix $\hat{\psi}$. This $\hat{\psi}$ can be regarded a specific order parameter for the vicinity of the special point.

4.3.4. SYMMETRY-BREAKING TERMS

As discussed in REF, there are actually three distinct terms of this sort. The first term corresponds to deviations of the terminals from the equator at non-zero energy: energy term. The second one describes the first-order corrections owing to the shift of the terminals along the equator: the shift of the phases in N-dimensional parameter space from the special point. Since it is linear in phase deviations, it is sensitive to the shift along a single direction in the N-dimensional parameter space, that we call the main axis. The third term describes the influence of the shift in the direction perpendicular to the main axis: it has to be the second-order term.

To compute the first term, we expand the Green functions of the terminals as

$$\hat{G}_T = \zeta_T \eta_y + \frac{\varepsilon}{\Delta_i}\eta_z \tag{4.18}$$

and collect first-order corrections induced in the connectors adjacent to the nodes. This gives

$$\mathcal{S}_1 = -\tilde{g}\,\mathrm{Tr}\left[\hat{\varepsilon}\sin\hat{\psi}\right] \tag{4.19}$$

$$\tilde{g} = \sum_{i,a} \frac{1}{\Delta_i}\mathcal{F}'_{ia}(\cos\theta_a)\sin\theta_a \tag{4.20}$$

The constant $\tilde{g}$ has a meaning of the maximum inverse level splitting of Andreev states. The above expression is for the case of short nanostructure $\Delta \ll E_{\mathrm{Th}}$, E_{Th} being the Thouless energy. In general case, we need to take into account at the circuit theory level the so-called "leakage" terminals [8] that account for finite volume of the nodes. This gives an addition to $\tilde{g}$ in terms of inverse level spacings δ^a_S in all nodes,

$$\tilde{g} \to \tilde{g} + \sum_a \frac{1}{\delta^a}. \tag{4.21}$$

Thus in the opposite limit $\Delta \gg E_{\mathrm{Th}}$ $\tilde{g}$ is the inverse level spacing for normal electron states in the whole structure.

Next, we consider the effect of phase deviations $\chi_i(\tau)$ from the special point, $\varphi_i(\tau) = \pi/2 + \pi\zeta_i + \chi_i(\tau)$ The expansion of the terminal Green functions read

$$\hat{G}_i = \zeta_i \eta_y - \zeta_i \hat{\chi}_i \eta_x \tag{4.22}$$

where $\hat{\chi}_i \equiv \chi(\tau)\delta(\tau - \tau')$. Collecting the first-order corrections to the action of adjacent connectors gives

$$\mathcal{S}_2 = \sum_i F_i\,\mathrm{Tr}\left[\hat{\chi}_i \cos\hat{\psi}\right]; \tag{4.23}$$

$$F_i = \zeta_i \sum_a \mathcal{F}'_{ia}(\cos\theta_a)\sin\theta_a \tag{4.24}$$

F_i is a dimensionless vector in the space of the terminals with the amplitude proportional to the dimensionless conductance g of the structure.

The computation of the third term is more involved since it concerns the second order corrections. It is contributed by the first-order terms coming from the second-order deviations of the terminal Green functions and the quadratic reaction of the network on the first-order deviations of those. To find the latter, we expand the Green functions in all nodes till quadratic terms in their deviations $\hat{w}$, find the terms coupling these deviations and first-order deviations of the terminal Green functions, and minimize with respect to w. The result reads ($\hat{U} \equiv e^{i\hat{\psi}}$)

$$\mathscr{S}_3 = \frac{1}{2}\sum_{i,j} H_{ij}\,\mathrm{Tr}[\hat{U}\hat{\chi}_i\hat{U}\hat{\chi}_j + \hat{U}^{-1}\hat{\chi}_i\hat{U}^{-1}\hat{\chi}_j] \tag{4.25}$$

$\check{H}$ being the matrix in the space of the terminals. It is dimensionless and also scales as the dimensionless conductance g of the nanostructure. Eventually, the vector χ_i in this expression has to be orthogonal to F_i, since the second corrections in these direction are negligible in comparison with the first order term taken into account in Eq. 4.23.

Its concrete expression is rather clumsy,

$$\check{H} = 2 + \frac{1}{2}\check{B}^T\check{Q}^{-1}\check{B} + \frac{1}{2}\check{A}^T\check{P}^{-1}\check{A}; \tag{4.26}$$

Where the matrices $\check{A}$, $\check{B}$ connect the terminals and nodes,

$$A_{ai} = \frac{1}{2}(\mathscr{F}''_{ai}\sin^2\theta_a + \zeta_i\mathscr{F}'_{ai}\cos\theta_a), \tag{4.27}$$

$$\check{B}_{ai} = \frac{1}{2}\zeta_i\mathscr{F}'_{ai}\cos(\theta_a) \tag{4.28}$$

and $\check{Q}, \check{P}$ are matrices in the space of the nodes,

$$\begin{aligned} P_{ab} = \frac{1}{2}\delta_{ab}&\left[-\sum_i A_{ai} - \sum_c(\mathscr{F}'_{ac}\cos(\theta_a-\theta_c) - \mathscr{F}''_{ac}\sin^2(\theta_a-\theta_c))\right] \\ &- \mathscr{F}'_{ab}\cos(\theta_a-\theta_b) + \mathscr{F}''_{ab}\sin^2(\theta_a-\theta_b) \end{aligned} \tag{4.29}$$

$$Q_{ab} = -\delta_{ab}(\sum_i B_{ai} + \frac{1}{2}\sum_c \mathscr{F}'_{ac}\cos(\theta_a-\theta_c)) + \mathscr{F}'_{ab}. \tag{4.30}$$

In all above expressions, $\mathscr{F}'_{ab} \equiv \mathscr{F}'_{ab}(\cos(\theta_a-\theta_b)$, $\mathscr{F}'_{ai} \equiv \mathscr{F}'_{ab}(\cos(\theta_a)$ and similar for $\mathscr{F}''$.

The actual $\hat{\phi}$ as a functional of $\chi(\tau)$ is found by minimization of all three symmetry-breaking terms. Therefore the answer for the relevant part of the nanostructure action reads

$$\mathscr{S}_{\mathrm{ns}} = \min_{\hat{\psi}}[\mathscr{S}_1 + \mathscr{S}_2 + \mathscr{S}_3]. \tag{4.31}$$

4.4. THE ACTION

In this Section, we will present the resulting action in several equivalent forms, discuss the energy and parametric space distance scales, and establish the relevant simpler limits. We collect the results of the previous Sections into the following form:

$$\mathscr{S} = \min_{\hat{\psi}} \mathrm{Tr}[-\tilde{g}\hat{\varepsilon}\sin\hat{\phi} + F_i\hat{\chi}_i\cos\hat{\psi} + \frac{1}{2}H_{ij}(\hat{U}\hat{\chi}_i\hat{U}\hat{\chi}_j + \hat{U}^{-1}\hat{\chi}_i\hat{U}^{-1}\hat{\chi}_j)] + \\ \int d\tau\left(\frac{\hbar^2}{4e^2}(\hat{L})^{-1}_{ij}\delta\chi_i(\tau)\delta\chi_j(\tau) + \frac{4e^2}{\hbar^2}C_{ij}\dot{\chi}_i(\tau)\dot{\chi}_j(\tau)\right), \quad (4.32)$$

$\delta\chi \equiv \chi(\tau) - \bar{\chi}$. Let us do the following rescalings and coordinate changes. First of all, we make the energy dimensionless measuring it in units of Δ: $\epsilon = \varepsilon/\Delta$. Here Δ is the superconducting energy gap if it is the same in all leads or the maximum of Δ_i. Its precise value is not important since near the special point the relevant energy scale is much smaller than Δ. We define $g \equiv \tilde{g}\Delta$ as the measure for dimensionless conductance of the nanostructure. Next, we change the coordinates in the phase parametric space. The coordinate in the direction of the main axis is defined as $\chi = F_i\chi_i/g$, χ being dimensionless and small as far as we are in close vicinity of the special point. We project the matrix H_{ij}/g into $N-2$ directions orthogonal to the main axis, diagonalize it and introduce the dimensionless coordinates $r_k = \sqrt{H_k}h_j^{(k)}\chi_j$, H_k, $h_j^{(k)}$ being the eigenvalues and corresponding eigenstates of this matrix. We disregard the capacitance terms in the circuit action assuming that the frequency scale of the relevant quantum fluctuations is much smaller than $1/\sqrt{LC}$. With this, we rewrite the action as follows:

$$\mathscr{S} = -\frac{g}{2}\min_{\hat{\psi}}[\mathrm{Tr}[\hat{U}^\dagger\hat{A} - \hat{U}\hat{r}_k\hat{U}\hat{r}_k + h.c.]] + \frac{G}{2}\mathrm{Tr}[(\delta\hat{\chi}^2) + \frac{G^k}{G}\delta\hat{\chi}\delta\hat{r}_k + \frac{G^{kl}}{G}\delta\hat{r}_k\delta\hat{r}_l] \quad (4.33)$$

with

$$A, A^\dagger = \hat{\chi} \pm i\epsilon. \quad (4.34)$$

Here, we rewrote the inverse inductance matrix in new coordinates in the parameter space. The nanostructure is characterized by dimensionless conductance g, and the circuit by the dimensionless conductance $G \gg g$, the larger value G corresponding to smaller interaction. Two dimensionless energy scales are defined by $|\bar{\chi}|$, $\sum_k \bar{r}_k^2 \equiv r^2$. Without interactions, $|\chi| > 4r^2$ corresponds to the gapped phase, $|\chi| < 4r^2$ to the gapless one.

It may seem that the most pronounced interaction effect comes from the fluctuations of r_k. Naively, the coefficient r^2 in front of the third term would be replaced by $\langle\langle r^2\rangle\rangle$ and would remain finite even at $\bar{r} = 0$ resulting in a finite width of the separating gapless phase domain. More careful analysis shows that this does not happen. Owing to the ordering of the operators $\hat{r}$ and $\hat{U}$ the fluctuations of r eventually lead for insignificant corrections $\simeq G^{-1}$ to the second term. This inspires us to disregard the fluctuations of $\hat{r}$. Indeed, except the crucial point mentioned, their fluctuations should provide lesser effect than those of χ that enter the action in the first order. So in further analysis, we disregard the fluctuations of r_k skipping the last two terms in the action (4.33).

With these assumptions, let us look at the limits. To start with this, let us assume no fluctuations of χ as well and replace it with a time-independent value. It may seem that this would lead to a trivial correction like the one given by Eq. 4.6 and would not modify the spectrum significantly. However, the inverse inductance of the nanostructure logarithmically diverges at $r^2 \to 0$, $\partial E/\partial\chi = -(g/\pi)\chi\ln(1/|\chi|)$ so it successfully competes with the formally larger confining term at an exponentially small scale of χ, $\chi_0 \equiv \exp(-\pi G/g)$. This scale defines an interesting quasi-classical limit detailed in Section 4.6.

Let us understand the significance of quantum fluctuations in this limit. The quantum fluctuation of χ can be generally estimated as

$$\langle\langle \chi^2 \rangle\rangle \simeq \frac{\epsilon_s}{G}, \tag{4.35}$$

ϵ_s being the relevant frequency scale. In semi-classical regime this scale is defined by χ_0. Comparing the fluctuation and χ_0 itself, $\langle\langle \chi^2 \rangle\rangle \leftrightarrow \chi_0^2$ we obtain that the quantum fluctuations can be neglected if $\chi_0 \gg 1/G$, that is, if $g \gg G/\pi \ln G$. Since $g \ll G$, this sets a rather narrow but relevant range of g.

If $g \ll G/\pi \ln G$, the quantum fluctuations destroy the logarithmic divergence and the nanostructure contribution to the action does not compete with that of the circuit, $\mathscr{S}_{\text{ns}} \ll \mathscr{S}_{\text{ct}}$. The way to proceed in this case is to expand $e^{-\mathscr{S}}$ in terms of $\mathscr{S}_{\text{ns}}$ keeping the first term of the expansion. The nanostructure is thus characterized by $\mathscr{S}_{\text{ns}}$ averaged over Gaussian quantum fluctuations produced by the circuit,

$$\overline{\mathscr{S}_{\text{ns}}} = \int \prod_{\tau} d\chi_\tau \mathscr{S}_{\text{ns}}(\{\chi(\tau)\}) \exp\left(-\frac{G}{2}\int d\tau (\chi(\tau)-\bar{\chi})^2\right) \tag{4.36}$$

We compute the first-order ($\propto G^{-1}$) interaction correction in Section 4.7. To estimate where it becomes significant, we compare $\langle\langle \chi^2 \rangle\rangle$ with χ taking χ as the relevant frequency scale. With this, the interaction leads to significant modification of the spectrum at small scale $\chi \simeq 1/G$. (Fig. 4.1 c)

If we depart from the special point in the orthogonal direction at distances $r^2 \gg 1/G$, the interaction is significant in a narrow strip at the boundary between the gapped and gapless phase, that is shifted by $\simeq G$, $\chi_c = 4r^2 - 0.79/G$ (as computed in the next Section). To estimate the width of strip $\delta\chi_c$, we compare it with the quantum fluctuation (Eq. 4.35) taking into account that the relevant frequency scale is defined by $\delta\chi_c$ itself, $\epsilon_s \simeq \chi_c(\delta\chi_c/\chi_c)^{3/2}$ (see Section 4.8 for details). This gives $\delta\chi_c \simeq G^{-1}(\chi_c G)^{-1}$. (Fig. 4.1 c)

Let us complete this Section with giving several equivalent forms of the action that are convenient for concrete calculations. If we neglect the fluctuations of r_k, we can rescale the action measuring frequency in units of $4r^2$ and introducing rescaled $X \equiv \chi/(4r^2)$. In this form, the action reads:

$$\mathscr{S} = -\frac{4r^2 g}{2} \min_{\hat{\psi}} \left[\mathrm{Tr}\left[\hat{U}^\dagger \hat{A} - \frac{\hat{U}^2}{4} + h.c\right]\right] + \frac{1}{2\lambda}\mathrm{Tr}[(\hat{X}-\bar{X})] \tag{4.37}$$

with $\lambda = (4r^2 G)^{-1}$, $\hat{A} = \hat{X} + i\hat{\epsilon}$.

Apart from an insignificant constant, the third term containing two $\hat{U}$ matrices can be presented as a minimum over an additional Hermitian operator $\hat{p}$,

$$\frac{1}{2}\mathrm{Tr}[\hat{U}\hat{r}_k\hat{U}\hat{r}_k + \hat{U}^\dagger\hat{r}_k\hat{U}^\dagger\hat{r}_k] = \min_{\hat{p}_k}\mathrm{Tr}[\frac{\hat{p}^2}{2} + i\hat{p}(\hat{U}\hat{r}_k - \hat{r}_k\hat{U}^\dagger)] \tag{4.38}$$

This suggests the following form of the action:

$$\mathscr{S} = -\frac{g}{2}\min_{\hat{\phi},\hat{p}_k}[\mathrm{Tr}[\hat{U}^\dagger\hat{A} - \sum_k \hat{p}_k^2/2 + h.c.] + \frac{G}{2}\mathrm{Tr}[(\hat{\chi}-\bar{\chi})^2] \tag{4.39}$$

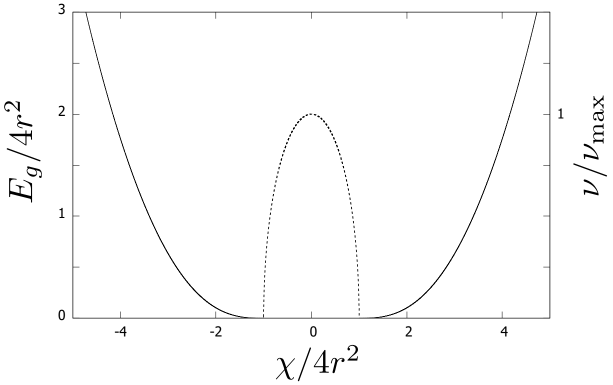

Figure 4.4: The spectrum of the nanostructure without interaction. We plot the gap in the gapped phases (solid line) and the density of states in the gapped phase $|\chi| < 4r^2$

with $A = \hat\chi - i2\hat p_k \hat r_k + i\hat\epsilon$.

The latter trick can be also applied to the rescaled form of the action (Eq. 4.37). In this case, we may use a single auxiliary operator $\hat p$ that can be regarded as an addition to $\hat\epsilon$. So it is convenient to rewrite the action as

$$\mathscr{S} = -\frac{4r^2 g}{2}\min_{\hat\psi,\tilde\epsilon}[\mathrm{Tr}[\hat U^\dagger \hat A + \hat A^\dagger \hat U - (\hat\epsilon - \hat{\tilde\epsilon})^2] + \frac{1}{2\lambda}\mathrm{Tr}[(\hat X - \bar X)] \tag{4.40}$$

with $A = \hat X + i\hat{\tilde\epsilon}$.

4.5. NON-INTERACTING SPECTRUM

Let us reproduce the results without interaction obtained in [19] and extend those for the needs of the present paper. In this case, we can replace fluctuating $\hat\chi$ with a constant χ regarding it as a parameter. We will use the rescaled action given by Eq. 4.40. All operators involved are diagonal in energy representation so we replace them by the corresponding eigenvalues. The minimization with respect to $\hat\psi$ gives

$$U \equiv e^{i\psi} = \frac{X + i\tilde\epsilon}{\sqrt{\tilde\epsilon^2 + X^2}} \tag{4.41}$$

and that with respect to $\tilde\epsilon$ gives $\tilde\epsilon(\epsilon)$ in the following implicit form:

$$\epsilon = \tilde\epsilon\left(1 - \frac{1}{\sqrt{X^2 + \tilde\epsilon^2}}\right). \tag{4.42}$$

Let us first solve these equations at zero energy. If $|X| > 1$, the only solution of Eq. 4.42 is $\tilde\epsilon(0) = 0$. With this, $U(0) = \mathrm{sgn}(X)$, $\psi = \pi/2(1 - \mathrm{sgn}(X))$ and the density of states $\simeq \sin\psi$ is zero. We are in a gapped phase, topologically distinct phases being realized at positive/negative X. If $|X| < 1$, another solution is realized, $\epsilon(0) = \sqrt{1 - X^2}$. This gives a non-zero density of states at zero energy :

$$\frac{\nu}{\nu_{max}} = \sqrt{1-X^2}. \tag{4.43}$$

We are in the gapless phase separating the gapped ones.

To find the gap in the gapped phases, we look at the solutions at imaginary ϵ and find the root of $\partial\epsilon/\partial\tilde{\epsilon} = 0$. This gives

$$E_g = \left(|X|^{2/3} - 1\right)^{3/2}, \tag{4.44}$$

so the gap closes at $|X| = 1$ and approaches $|X|$ at $|X| \gg 1$. We plot these results in Fig. 4.4.

We can also compute the energy of the nanostructure. For our purposes, we only need its derivative with respect to X, that is given by

$$\frac{\partial E}{\partial X} = -4r^2 g \int \frac{d\epsilon}{2\pi} \cos\psi = -4r^2 g \frac{d\epsilon}{2\pi} \frac{X}{\sqrt{X^2+\tilde{\epsilon}^2}}. \tag{4.45}$$

This integral can be easily evaluated by transforming the integration variable with the help of Eq. 4.42. Note the logarithmic divergence at $\epsilon \to \infty$, that we cut at $|\epsilon| \approx |\tilde{\epsilon}| = \omega_D \gg |X|$. With this, the result in the gapped phase reads

$$\frac{\partial E}{\partial X} = -\frac{4r^2 g}{2\pi} X \left(\ln\left(\frac{2\omega_D}{|X|}\right) + Z(X)\right); \tag{4.46}$$

$$Z(X) \equiv -\frac{\pi}{4|X|} + \frac{\Theta(1-|X|)}{2}\left(\sqrt{1-X^2} + X \arctan\left(\frac{\sqrt{1-X^2}}{X}\right)\right) \tag{4.47}$$

Thus, in the gapless phase, $Z(X)$ acquires an addition given by the second term in Eq. 4.47.

4.6. QUASICLASSICAL LIMIT

In this Section, we concentrate on the quasiclassical limit of the interacting problem. As outlined in Section 4.4, it is realized at $G \gg g \gg G/\ln G$. We can disregard the fluctuations of $\chi(\tau)$ treating it as a time-independent variable χ. However, in a close vicinity of the special point the external circuit fails to confine χ to the parameter $\bar{\chi}$, as expected in the non-interacting limit $G \gg 1$. The reason for this is the logarithmic divergence of the inverse inductance of the nanostructure that was just quantified in the previous Section. The actual value of χ has to be determined from the minimization of the action given by Eq. 4.33 or Eq. 4.40,

$$\frac{\partial E(\chi)}{\partial \chi} + G(\chi - \bar{\chi}) = 0. \tag{4.48}$$

We will use the rescaled action. With Eq. 4.46, the above self-consistency equation reads

$$X(\ln\left(\frac{2\omega_D}{|X|} + Z(X))\right) = \frac{G}{\pi g}(X - \bar{X}) \tag{4.49}$$

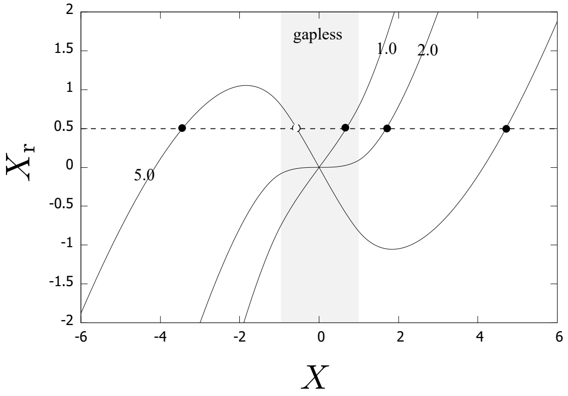

Figure 4.5: Quasiclassical limit. Solving the self-consistency Eq. 4.51. The curves $X_r(X)$ resembling van der Waals isotherms are plotted for several values of χ_0 given in the curve labels. Stable solutions for $X_r = 0.5$ are given by black dots. The solutions within the grey strip correspond to gapless phase.

Actually, it resembles a well-known BCS self-consistency equation (see, e.g. [36]) for the superconducting order parameter Δ , X playing the role of Δ, that relies on a similar logarithmic divergence of a response function. We will get rid of the explicit cut-off ω_D by very same method as in BSC theory: We substute $(G/\pi g)$ with $\ln(2\omega_D/\chi_0)$, which defines new exponentially small scale

$$\chi_0 = 2\omega_D \exp\left(-\frac{\pi G}{g}\right), \tag{4.50}$$

and also rescale the external parameter $X_r = \bar{X}(G/\pi g)$. With this, the self-consistency equation becomes an expression for X_r in terms of X,

$$X_r = -X(\ln(\chi_0/X) + Z(X)). \tag{4.51}$$

This is the rescaled equation so $r^2 \to 0$ corresponds to $\chi_0 \gg 1$. In this limit, one can neglect $Z(X)$. At $X_r = 0$, that is, precisely at the special point we encounter two solutions $X = \pm\chi_0$ corresponding to two gapped phases with the gap χ_0. These two solutions coexist up to $|X| = \chi_0/e$. Their energies differ except at $X_r = 0$, where we encounter the line of first order transition (Fig. 4.1. a). For further qualitative analysis, it is instructive to plot Eq. 4.51 for several values of χ_0(Fig. 4.5)where the resemblence to van der Waals isothermes becomes apparent. We see that the line of constant X_r gives either one (at $\chi_0 < 2$) or three solutions (at $\chi_0 > 2$) for X, two of them being stable. The first-order transition line thus ends at $\chi_0 = 2$ (This corresponds to the critical distance $4r^2 = 0.5\chi_0$ in non-rescaled units). The lines where the stable solutions dissapear (dashed lines in Fig. 4.1 b) are defined from the positions of the extrema of the curves drawn in Fig. 4.5 and were obtained by the implicit plot

$$X_r = X^2 Z'(X) - 1 \tag{4.52}$$

$$\ln\chi_0 = \ln|X| - Z(X) - XZ'(X) + 1 \tag{4.53}$$

The solutions with $|X| < 1$ correspond to the gapless phase. Substituting $X = \pm 1$ to Eq. 4.51 gives the lines of phase transitions between the gapless and gapped phases $X_r = \pm(\pi/4 - \ln\chi_0)$. We note that the gap disappears already at the first order transition line, at $\chi_0 = \exp(\pi/4) \approx 2.19$ (in non-rescaled coordinates, this corresponds to $4r^2 = 0.46\chi_0$.

The full phase diagramm is presented in Fig. 4.1 b in coordinates $4r^2/\chi_0$, X_r/χ_0.

We expect the quantum fluctuations to provide tunnel coupling between the distinct minimums of the action. This will result in a non-degenerate ground state even at $X_\mathrm{r} = 0$ that is a quantum superposition of two topologically distinct gapped states.

4.7. QUANTUM CORRECTIONS

In this Section, we consider the limit of $g \ll G/\ln G$ where we can average the nanostructure action and all quantities involved over the Gaussian fluctuations of χ produced by the external circuit (see Eq. 4.36). Such averaging is impossible to do in general owing to the complexity of the resulting non-linear action. We restrict ourselves to the evaluation of the first-order correction.

A most straightforward way to proceed is to take the nanostructure action given by Eq. 4.37, regard the time-dependent part of X, $x(\tau)$ as a perturbation entering the minimization equations for $\hat{U}$, solve those by subsequent iterations to the second order in $\delta\chi$,

$$\hat{U} = \hat{U}^{(0)} + \hat{U}^{(1)} + \hat{U}^{(1)}; \tag{4.54}$$

$$\hat{U}^{(1)} = \hat{A}\hat{x}\hat{B}; \tag{4.55}$$

$$\hat{U}^{(2)} = \hat{C}\hat{x}\hat{D}\hat{x}\hat{E}, \tag{4.56}$$

$\hat{U}^{(0)}, \hat{A} - \hat{E}$ being the operators diagonal in energy representation, average this over the fluctuations employing $\langle\langle x(\tau)x(\tau')\rangle\rangle = \lambda\delta(\tau - \tau')$. That results in correction

$$\delta U(\tau - \tau') = \lambda \int d\tau_1 C(\tau - \tau_1) D(0) E(\tau_1 - \tau') \tag{4.57}$$

to be compared with $U^{(0)}(\tau - \tau')$.

We proceed in an equivalent, slightly more difficult but more instructive way. We take the nanostructure action given by Eq. 4.40 and substitute there the operators $\hat{U}, \hat{\tilde{\epsilon}}$ in a diagonal form plus non-diagonal deviations. We expand the action up to the second order in these deviations thereby accounting for the fluctuations of X in this order, minimize the resulting quadratic action, and average over the fluctuations. This results in an additional $\propto \lambda$ term in the action, that is a functional in diagonal elements of the operators. Subsequent minimization over the diagonal elements permits to find the interaction correction to those.

To start, we rewrite the action employing the Lagrange multiplier $\hat{M}$ to ensure unitarity of U,

$$\mathscr{S}_\mathrm{ns} = -\frac{4r^2 g}{2} \min_{\hat{U}, \hat{M}, \tilde{\epsilon}} [\mathrm{Tr}[\hat{U}^\dagger \hat{A} + \hat{A}^\dagger \hat{U} - (\hat{\epsilon} - \hat{\tilde{\epsilon}})^2 - \hat{M}(\hat{U}\hat{U}^\dagger - 1)] \tag{4.58}$$

We separate the operators into diagonal and non-diagonal parts (we skip hats for diagonal operators) : $\hat{A} = A + \hat{a}$, $\hat{M} = M + \hat{M}$, $\hat{U} = U + \hat{u}$, $\hat{a} = \hat{x} + i\hat{p}$. The action up to the terms quadratic in diagonal elements reads:

$$\mathscr{S}_{\rm qd} = -\frac{4r^2 g}{2}\mathrm{Tr}[\hat{u}^\dagger \hat{a} + \hat{a}^\dagger \hat{u} - \hat{p}^2 - \hat{m}(uU^\dagger + U\hat{u}^\dagger) - M\hat{u}\hat{u}^\dagger] \tag{4.59}$$

The minimization of this part with respect to all variables except $\hat{x}$ gives

$$\mathscr{S}_{\rm qd} = -\frac{4r^2 g}{2}\sum_{k,l}\frac{|U_l - U_k^*|}{2D_{kl}}|x_{kl}|^2, \tag{4.60}$$

$$D_{kl} \equiv (M_k - 1)|U_k|^2 + (M_l - 1)|U_l|^2 + \frac{1}{2}|U_l - U_k^*|^2 \tag{4.61}$$

where k, l index the discrete Matsubara energies. Here, $|U_k|^2 \neq 1$: although the matrix $\hat{U}$ is unitary, it also contains non-diagonal elements. The averaging over the quantum fluctuations yields the quantum correction to the action,

$$\mathscr{S}_{\rm q} = -\frac{4r^2 g}{2}\lambda(k_B T)\sum_{k,l}\frac{|U_l - U_k^*|}{2D_{kl}} \equiv -\frac{4r^2 g}{2}S_{\rm q} \tag{4.62}$$

To obtain the quantum corrections to the quantities, one has to minimize it with the diagonal part of the action,

$$\mathscr{S}_0 = -\frac{4r^2 g}{2}\sum_k [U_k^* A_k + A_k^* U_k - (\epsilon_k - \tilde{\epsilon}_k)^2 + M_k(|U_k|^2 - 1). \tag{4.63}$$

The resulting minimization equations read ($U \equiv R + iY$ with real R, Y)

$$X - MR + \frac{1}{2}\frac{\partial S_{\rm q}}{\partial R} = 0 \tag{4.64}$$

$$1 - R^2 - Y^2 + \frac{1}{2}\frac{\partial S_{\rm q}}{\partial M} = 0 \tag{4.65}$$

$$Y(1 - M) + \epsilon + \frac{1}{2}\frac{\partial S_{\rm q}}{\partial Y} = 0 \tag{4.66}$$

with $\tilde{\epsilon} - \epsilon = Y$.

To give an example of practical calculation, let us evaluate a "correction to unitarity" given by Eq. 4.65 that quantifies the importance of fluctuation-induced non-diagonal matrix elements in U. We compute $\partial S_{\rm M}$,

$$\frac{\partial S_{\rm q}}{\partial M_l} = \frac{2(-Y_l Y_k + R_l R_k - 1)}{(M_l + M_k - 1 - R_k R_l + Y_l Y_l)^2} \tag{4.67}$$

We concentrate on zero energy and gapped phase, so we substitute $M_l = X, R_l = 1, Y_l = 0$ and $M_k = \sqrt{\tilde{\epsilon}^2 + X^2}$, $R_k = X/\sqrt{\tilde{\epsilon}^2 + X^2}$, $Y_k = \tilde{\epsilon}/\sqrt{\tilde{\epsilon}^2 + X^2}$ and change integration variable to $\tilde{\epsilon}$ as we did to derive Eq. 4.46. This gives (see Fig. 4.6 for the plot)

$$\frac{|U_0|^2 - 1}{\lambda} = \sqrt{\frac{X-1}{X+1}}\frac{2X(X+3)}{(1+X)^2}\left(1 - \frac{\arctan(\sqrt{X^2 - 1})}{\pi}\right) + \frac{8(2-X)}{3\pi(1+X)^2} - 1 \tag{4.68}$$

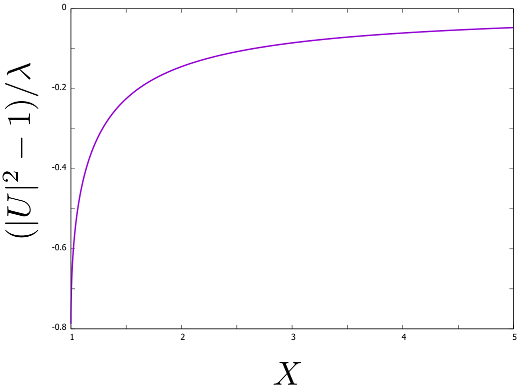

Figure 4.6: Interaction correction to "unitarity" of the Green function matrix versus X. The gapped phase, zero energy. The correction is of the order of λ and remains finite at the critical point $X = 1$.

The correction remains finite at the critical point, $|U|^2 - 1 = \lambda(2/3\pi - 1)$, although there is a square-root singularity in this point. At $X \to \infty (r \to 0)$ $|U|^2 - 1 = -\lambda(2/3\pi)/X$ In non-rescaled units, this implies that the correction amounts to 50 % at $r = 0$, $\chi = 4/3\pi G$, as shown in Fig 4.1 b.

Let us compute the interaction-induced shift of the critical point that is located at $X = 1$ for $\lambda = 0$. We regard the total action as a function of four real parameters $y_a = (R, Y, M, \tilde{\epsilon})$ at zero energy. The critical point is determined from the condition $\det \partial_a \partial_b \mathscr{S} = 0$ under constraint $\partial_a \mathscr{S} = 0$. We find the matrix $\partial_a \partial_b \mathscr{S}_0$, diagonalize it at the critical point $\lambda = 0$ and bring in as small perturbations the shift of the parameters and the interaction correction action $\mathscr{S}_q$. The condition of zero eigenvalue then reads

$$\delta M = \frac{1}{2} \frac{\partial^2 S_{\mathrm{q}}}{\partial Y^2} \tag{4.69}$$

where δM is contributed by δX and the first-order correction computed from Eqs. 4.64, 4.65, 4.66. With this, the shift of the critical point

$$\delta X = \frac{1}{2} \left(\frac{\partial^2 S_{\mathrm{q}}}{\partial Y^2} - \frac{\partial S_{\mathrm{q}}}{\partial R} + \frac{\partial S_{\mathrm{q}}}{\partial M} \right) \tag{4.70}$$

Substituting the values at the critical point to the derivatives of S_{q} and performing integration over $\tilde{\epsilon}$ yields

$$\delta X = -\lambda \left(\frac{2}{3\pi} - 1 \right) \approx -0.79\lambda. \tag{4.71}$$

In non-rescaled coordinates, it corresponds to the shift of the phase boundary in the main axis direction by $\Delta\chi = \pm 0.79/G$.

It is important to notice that the denominator in the expression for $\mathscr{S}_{\mathrm{q}}$, Eq. 4.62, vanishes at low energies in the gapless phase,

$$D_{kl} \propto |\epsilon_k| + |\epsilon_l|, \tag{4.72}$$

provided the energies are of opposite sign, $\mathrm{sgn}(\epsilon_k)\mathrm{sgn}(\epsilon_l) = -1$. This form of the denominator manifests the existence of low-energy modes. The presence of low-energy modes might seem surprising: however, in the next Section we reveal that the gapless phase may be related to a breaking of a continuous symmetry, so this is just a manifestation of the Goldstone mechanism. This feature in the denominator might lead to low-energy divergences in the first-order interaction corrections under consideration. However, it does not: rather, the correction exhibit specific non-analytical terms in their low-energy expansion,

$$A(\epsilon) = A(0) + \epsilon \ln(\epsilon_D/|\epsilon|) \tag{4.73}$$

while this dependence is analytical in non-interacting quantities.

To illustrate, we compute the correction to Y given by

$$Y^{(1)} = \frac{2}{M - R^2}\left(MY\frac{\partial S_\mathrm{q}}{\partial M} - RY\frac{\partial S_\mathrm{q}}{\partial R} + R^2\frac{\partial S_\mathrm{q}}{\partial Y}\right) \tag{4.74}$$

At low energies of the opposite sign, the integrand takes the following form

$$Y^{(1)}(\epsilon) = \lambda\frac{X^2}{2(1-X^2)^{3/2}}\int_0^\infty \frac{d\epsilon'}{2\pi}\left[2\frac{\epsilon-\epsilon'}{\epsilon+\epsilon'} - \frac{(\epsilon-\epsilon')^2}{(\epsilon+\epsilon')^2}\right] \tag{4.75}$$

This yields

$$Y^{(1)}(\epsilon) = \mathrm{const} + \frac{3\lambda X^2}{4\pi(1-X^2)^{3/2}}\epsilon \ln\left[\frac{\epsilon_D}{|\epsilon|}\right], \tag{4.76}$$

$\epsilon_D \simeq 1$ being the cut-off energy. We shall compare this with the low-energy dependence of Y without interaction

$$Y(\epsilon) = \sqrt{1-X^2} + \epsilon\frac{X^2}{1-X^2}. \tag{4.77}$$

This signals the break-down of the perturbation theory at arbitrary weak interaction: the energy dependence is dominated by correction at an exponentially small energy scale

$$\epsilon^\star \simeq \epsilon_D \exp\left(-\frac{\sqrt{1-X^2}}{3\lambda}\right). \tag{4.78}$$

This energy scale increases upon approaching the critical point, see the discussion in the following Section.

4.8. NEAR THE BOUNDARY

In this Section, we derive a simplified action valid near the phase transition line separating the gapped and gapless phases. This action resembles the Landau Hamiltonian commonly incorporated for the description of the second-order phase transitions. However, the order parameter is a matrix with two time indices. We derive the proper scaling of the action.

It is convenient to start from the action in the form given by Eq. 4.37. We note that at $X > 0$ in the gapped phase and near the phase transition $\hat\phi \ll 1$ so we can expand U in powers of $\hat\phi$. With this,

$$\mathscr{S}_\mathrm{ns} = \frac{4r^2 g}{2}\min_{\hat\psi}\mathrm{Tr}[-2\epsilon\psi + (a+\hat a)\frac{\psi^2}{2} + \frac{\psi^4}{4}] \tag{4.79}$$

Here, $a \equiv (X-1)/2$ is the critical parameter of the second-order phase transition. If we neglect the fluctuations $\hat{\tilde{a}}$ and the term with ϵ, the action describes the transition between the symmetric phase $\hat{\phi} = 0$ at $a > 0$ and the symmetry-broken phase $\hat{\psi}^2 = -a$. The symmetry-broken solution is highly degenerate if the eigenvalues of $\hat{\psi}$, $\pm\sqrt{-a}$, are of different sign: any unitary transformation $\hat{psi} \to U^{-1}\hat{\psi}\hat{U}$ would produce a distinct solution of the same energy. The term with ϵ plays the role of a peculiar anisotropy term that breaks the degeracy and makes the solutions for ψ unique on both sides of the transition. Without fluctuations, ψ is diagonal in energy, and $\psi(\epsilon) = -\psi(\epsilon)$. Its equilibrium value is computed from $2\epsilon = a\psi + \psi^3$. At $a > 0$ $\psi(\epsilon)$ is an analytical function of ϵ at $\epsilon \to 0$. This comforts the fact that it describes the gapped phase: the gap may be defined as the energy of the lowest singularity of $\psi(\epsilon)$ in the complex plane of ϵ. Correspondinly, $\psi(\epsilon)$ is non-analytical in the gapless phase: $\psi(\epsilon) = \mathrm{sgn}(\epsilon)\sqrt{-a}$ at small energies.

We consider here the quantum limit where we can just average the action and ψ over Gaussian fluctuations of $\tilde{a}$, $\langle\langle \tilde{a}(\tau)\tilde{a}(\tau')\rangle\rangle = (\lambda/4)\delta(\tau-\tau')$. The avegared $\langle\psi(\epsilon)\rangle$ become complex functions of energy, yet the transition point is defined in the same way, $\langle\psi(\epsilon)\rangle$ is an analytical function above the transition point and non-analytical otherwise.

Let us determine the scale of a at which the fluctuations become important, the perturbation theory does not work, and deviations of $\langle\psi(\epsilon)\rangle$ form non-interacting limit are significant. Equating the scales of three terms in Eq. 4.79, we see that the scale a_s determines the scale of ψ, $\psi_s = (a_s)^{1/2}$, and the energy, $\epsilon_s = a_s\psi_s = a_s^{3/2}$. The fluctuation of a is estimated as $(\Delta a)^2 = \lambda\epsilon_s$. Equating this to a, we obtain $a_s = \lambda^2$. In non-rescaled coorditates, this reproduces the estimation $\delta\chi_s/\delta\chi_s = G^{-2}$ from the previous Section (see also Fig. 4.1 c.)

The scaling implies that

$$\langle\psi(\epsilon)\rangle = a_s^{1/2} F(a/a_s, \epsilon/a_s^{3/2}) \tag{4.80}$$

The non-interacting values are reproduced at large values of the arguments of this scaling function. For practical applications, one also needs to account for the shift of the transition point (Eq. 4.71) that comes from the higher-energy fluctuations and does not conform this scaling which takes place in a small vicinity of the $shifted$ transition point.

Let us note that the exponentially small low-energy scale $\epsilon^\star$ found in the previous Section (Eq. 4.78) also conforms to this scaling. Near the critical point, but at $|a| \gg a_s$ it can be expessed as

$$\epsilon^\star \simeq a_s^{3/2}(a/a_s)^{3/2}\exp\left(-\frac{2}{3}\left(\frac{|a|}{a_s}\right)^{1/2}\right). \tag{4.81}$$

So it becomes of the order of all other scales at $a \simeq a_s$. This provokes a hypothesis that we formulate in the concluding Section.

4.9. CONCLUSIONS AND HYPOTHESES

There are few examples of condensed matter models where an arbitrary weak interaction qualitatively changes the fermionic spectrum, the superconductivity is the most famous one. In this paper, we predict a drastic effect of weak interaction on the Andreev spectrum near the special points in multi-terminal semiclassical superconducting nanostructures.

This is a generic effect to arise in any nanostructure. Our approach is valid for normal nanostructures but also for superconducting ones, provided they are smaller than the superconducting coherence length. It can be experimentally observed by studying the tunnelling to these nanostructures at low energies.

We have developed a general interaction model and came up with a simple universal action describing the situation. This is a complex non-local and non-linear quantum field theory that cannot be analytically treated by existing methods. Its numerical study is plausible but requires a significant effort in view of the matrix nature of the order parameter. In this paper, we analytically studied a semiclassical limit and the first-order interaction correction in the quantum limit.

In both limits, our results indicate that the effect on the spectrum is drastic in the close vicinity of the special point at the scale defined by interaction. The domain of the gapless phase is squeezed. In semiclassical limit, we see the failure of the topological protection: two gapped phases of distinct topology come to contact not being separated by a gapless phase.

We would like to put forward two hypotheses to be confirmed or disproved in the course of further research. First hypothesis is that the gapped phases are in direct contact at the special point also in the quantum limit. This hypothesis is based on continuity: one can go from semiclassical to quantum limit by changing the parameter g. An alternative would be a phase transition upon this change.

The second hypothesis is provoked by an exponentially small low-energy scale $\epsilon^\star$ found in the gapless phase. It may be that a gap develops at this energy scale, and the gapless phase without interaction always becomes gapped in the presence of an arbitrary weak interaction, even far from the special point. In this case, the phase transition between gapped and gapless phase would become a crossover not separating distinct phases. The fact that $\epsilon^\star$ conforms to the critical scaling supports this hypothesis.

REFERENCES

[1] B. D. Josephson, *The discovery of tunnelling supercurrents*, Rev. Mod. Phys. **46**, 251 (1974).

[2] Z.-L. Xiang, S. Ashhab, J. Q. You, and F. Nori, *Hybrid quantum circuits: Superconducting circuits interacting with other quantum systems*, Rev. Mod. Phys. **85**, 623 (2013).

[3] A. Blais, A. L. Grimsmo, S. M. Girvin, and A. Wallraff, *Circuit quantum electrodynamics*, Rev. Mod. Phys. **93**, 025005 (2021).

[4] M. Kjaergaard, M. E. Schwartz, J. Braumüller, P. Krantz, J. I.-J. Wang, S. Gustavsson, and W. D. Oliver, *Superconducting qubits: Current state of play*, Annual Review of Condensed Matter Physics **11**, 369 (2020), https://doi.org/10.1146/annurev-conmatphys-031119-050605 .

[5] A. Y. Kitaev, *Fault-tolerant quantum computation by anyons*, Annals of Physics **303**, 2 (2003).

[6] R. M. Lutchyn, E. P. A. M. Bakkers, L. P. Kouwenhoven, P. Krogstrup, C. M. Marcus, and Y. Oreg, *Majorana zero modes in superconductor–semiconductor heterostructures*, Nature Reviews Materials **3**, 52 (2018).

[7] E. Prada, P. San-Jose, M. W. A. de Moor, A. Geresdi, E. J. H. Lee, J. Klinovaja, D. Loss, J. Nygård, R. Aguado, and L. P. Kouwenhoven, *From andreev to majorana bound states in hybrid superconductor–semiconductor nanowires*, Nature Reviews Physics **2**, 575 (2020).

[8] Y. V. Nazarov and Y. M. Blanter, *Quantum Transport* (Cambridge University Press, Cambridge, 2009).

[9] C. W. J. Beenakker, *Random-matrix theory of quantum transport*, Rev. Mod. Phys. **69**, 731 (1997).

[10] B. van Heck, S. Mi, and A. R. Akhmerov, *Single fermion manipulation via superconducting phase differences in multiterminal josephson junctions*, Phys. Rev. B **90**, 155450 (2014).

[11] C. Padurariu, T. Jonckheere, J. Rech, R. Mélin, D. Feinberg, T. Martin, and Y. V. Nazarov, *Closing the proximity gap in a metallic josephson junction between three superconductors*, Phys. Rev. B **92**, 205409 (2015).

[12] T. Yokoyama and Y. V. Nazarov, *Singularities in the andreev spectrum of a multiterminal josephson junction*, Physical Review B **92**, 155437 (2015).

[13] R.-P. Riwar, M. Houzet, J. S. Meyer, and Y. V. Nazarov, *Multi-terminal josephson junctions as topological matter*, Nature Communications **7**, 11167 (2016).

[14] R. L. Klees, G. Rastelli, J. C. Cuevas, and W. Belzig, *Microwave Spectroscopy Reveals the Quantum Geometric Tensor of Topological Josephson Matter*, Physical Review Letters **124** (2020), 10.1103/PhysRevLett.124.197002.

[15] E. Repin, V, Y. Chen, and Y. Nazarov, V, *Topological properties of multiterminal superconducting nanostructures: Effect of a continuous spectrum*, Physical Review B **99** (2019), 10.1103/PhysRevB.99.165414.

[16] J. S. Meyer and M. Houzet, *Non-trivial Chern numbers in three-terminal Josephson junctions*, Phys. Rev. Lett. **119**, 136807 (2017).

[17] E. Eriksson, R.-P. Riwar, M. Houzet, J. S. Meyer, and Y. V. Nazarov, *Topological transconductance quantization in a four-terminal Josephson junction*, Phys. Rev. **B95**, 075417 (2017).

[18] H.-Y. Xie, M. G. Vavilov, and A. Levchenko, *Topological andreev bands in three-terminal josephson junctions*, Phys. Rev. B **96**, 161406 (2017).

[19] X.-L. Huang and Y. V. Nazarov, *Topology protection–unprotection transition: Example from multiterminal superconducting nanostructures*, Phys. Rev. B **100**, 085408 (2019).

[20] H.-Y. Xie and A. Levchenko, *Topological supercurrents interaction and fluctuations in the multiterminal josephson effect*, Phys. Rev. B **99**, 094519 (2019).

[21] H.-Y. Xie, J. Hasan, and A. Levchenko, *Non-abelian monopoles in the multiterminal josephson effect*, (2021), arXiv:2107.03435 [cond-mat.supr-con] .

[22] V. Fatemi, A. R. Akhmerov, and L. Bretheau, *Weyl josephson circuits*, Phys. Rev. Research **3**, 013288 (2021).

[23] N. Pankratova, H. Lee, R. Kuzmin, K. Wickramasinghe, W. Mayer, J. Yuan, M. G. Vavilov, J. Shabani, and V. E. Manucharyan, *Multiterminal Josephson Effect*, Physical Review X **10** (2020), 10.1103/PhysRevX.10.031051.

[24] G. Graziano, V, J. S. Lee, M. Pendharkar, C. Palmstrom, and V. S. Pribiag, *Transport studies in a gate-tunable three-terminal Josephson junction*, Physical Review B **101** (2020), 10.1103/PhysRevB.101.054510.

[25] A. W. Draelos, M.-T. Wei, A. Seredinski, H. Li, Y. Mehta, K. Watanabe, T. Taniguchi, I. V. Borzenets, F. Amet, and G. Finkelstein, *Supercurrent Flow in Multiterminal Graphene Josephson Junctions*, Nano Letters **19**, 1039 (2019).

[26] A. H. Pfeffer, J. E. Duvauchelle, H. Courtois, R. Mélin, D. Feinberg, and F. Lefloch, *Subgap structure in the conductance of a three-terminal josephson junction*, Phys. Rev. B **90**, 075401 (2014).

[27] E. M. T. Fadaly, H. Zhang, S. Conesa-Boj, D. Car, Önder Gül, S. R. Plissard, R. L. M. O. het Veld, S. Kölling, L. P. Kouwenhoven, and E. P. A. M. Bakkers, *Observation of conductance quantization in insb nanowire networks*, Nano Letters **17**, 6511 (2017), pMID: 28665621, https://doi.org/10.1021/acs.nanolett.7b00797 .

[28] J. Erdmanis, Á. Lukács, and Y. V. Nazarov, *Weyl disks: Theoretical prediction*, Physical Review B **98**, 241105 (2018).

[29] Y. Chen and Y. V. Nazarov, *Spin weyl quantum unit: A theoretical proposal*, Phys. Rev. B **103**, 045410 (2021).

[30] Y. Chen and Y. V. Nazarov, *Spintronics with a weyl point in superconducting nanostructures*, Phys. Rev. B **103**, 165424 (2021).

[31] E. Strambini, S. D'Ambrosio, F. Vischi, F. S. Bergeret, Y. V. Nazarov, and F. Giazotto, *The ω-squipt as a tool to phase-engineer josephson topological materials*, Nature Nanotechnology **11**, 1055 EP (2016).

[32] F. Vischi, M. Carrega, E. Strambini, S. D'Ambrosio, F. S. Bergeret, Y. V. Nazarov, and F. Giazotto, *Coherent transport properties of a three-terminal hybrid superconducting interferometer*, Phys. Rev. B **95**, 054504 (2017).

[33] T. Yokoyama, J. Reutlinger, W. Belzig, and Y. V. Nazarov, *Order, disorder, and tunable gaps in the spectrum of andreev bound states in a multiterminal superconducting device*, Phys. Rev. B **95**, 045411 (2017).

[34] G. Schön and A. Zaikin, *Quantum coherent effects, phase transitions, and the dissipative dynamics of ultra small tunnel junctions*, Physics Reports **198**, 90156 (1990).

[35] A. Altland and B. D. Simons, *Condensed matter field theory* (Cambridge University Press, 2010).

[36] P. G. de Gennes, *Superconductivity of Metals and Alloys* (W. A. Benjamin, New York, 1966).

5

SYNCHRONIZATION OF BLOCH OSCILLATIONS BY GATE VOLTAGE MODULATION

We propose to synchronize Bloch oscillations in a double phase-slip junction by modulating the gate voltage rather than the bias voltage. We show this is advantageous and the relatively small a.c. modulation of the gate voltage gives rise to the pronounced plateaux of quantized current of the width of the order of Coulomb blockade threshold.

We theoretically investigate the setup distinguishing three regimes of the strong, weak, and intermediate coupling defined by the ratio of the gate capacitance C and the effective capacitance of the phase-slip junctions. An important feature of the intermediate coupling regime is the occurrence of the fractional plateaux of the quantized current. We investigate the finite temperature effects finding an empirical scaling for the smoothing of integer plateaux.

This chapter is submitted to PRB as **Janis Erdmanis**, Yuli Nazarov, *Synchronization of Bloch oscillations by gate voltage modulation*, https://arxiv.org/abs/2107.10565 (2021). For numerical code and data see https://doi.org/10.5281/zenodo.5120790

5.1. INTRODUCTION

An elementary process giving rise to resistance in a quasi-one-dimensional superconducting wire is a phase-slip: an event where the magnitude of the superconducting order parameter locally and momentarily reaches to zero, allowing the phase difference of the superconducting order parameters on the left and on the right to slip by 2π [1, 2]. See [3] for review. This corresponds to a magnetic flux quantum Φ_0 moving across the wire, or, equivalently, a voltage pulse with $\int dtV(t) = \Phi_0$. The phase slips due to thermal and quantum fluctuations have been observed and identified in course of thorough and difficult experiments [4–6].

The quantum coherence between individual phase slip events results in modification of the ground state of superconducting systems that become a superposition of the states [7] that differ in flux quanta. Quantum coherent phase-slip states have been observed in superconducting nanowires [8, 9] and the chains of Josephson junctions that in many respects are similar to the superconducting nanowires [10]. There is a remarkable duality between the coherent tunnelling of flux quanta due to the phase slips and the coherent tunnelling of Cooper pairs transferring charge $2e$ that is the base of Josephson effect [11], so that each Josephson electronic circuit has a dual counterpart made from phase-slip junctions, and vice versa. This gave rise to many theoretical suggestions and experimental work [3, 12–21].

A phase-slip junction in a high resistive environment gives rise to a Coulomb blockade of the current up to a voltage threshold, that is dual to a zero-voltage state up to a current threshold in a Josephson junction.

It has been predicted [22–24] that this should give rise to an effect that is potentially indispensable for applications: synchronization of Bloch oscillations. Biasing a phase-slip junction with combination of d.c. and a.c. bias should give rise to current plateaux with the value corresponding to the a.c. frequency ω: $I = (e/\pi)\omega$. This may enable a high-precision current standard that is dual to the Josephson voltage standard [11]. However, it is much more difficult to realize a high-impedance environment than the low-impedance one, and prevent overheating of such environment by power dissipation. Although the phase-slip Coulomb blockade feature has been reliably observed, (e.g. [25, 26]), the attempts to achieve the synchronization of Bloch oscillations [18, 27–29] have not yet demonstrated a precision even remotely comparable to a Josephson voltage standard [30, 31].

Recently, much experimental and theoretical interest was received by a double phase-slip junction [14, 32, 33]. The total phase-slip amplitude there is a result of interference of the phase-slips in constituent junctions, this interference being affected by a gate voltage supplied via a capacitive coupling. The gate charge dependence has been successfully demonstrated in spectroscopy measurements of the phase-slip qubit level positions [34] and in the measurements of the Coulomb blockade threshold [32, 34, 35].

In this Article, we propose synchronization of Bloch oscillations in a double phase-slip junction by the a.c. gate voltage and theoretically investigate this phenomenon in a variety of regimes.

Let us explain here why, in our opinion, the gate voltage synchronization is advantageous in comparison with the standard bias synchronization. The reason is general although rather technical, at least from the theoretical point of view. A phase-slip junction should be embedded to a high-impedance environment with substantial capacitance. While this capacitance is irrelevant for d.c. bias, there is an overwhelming RC filtering of the a.c. signal. To get a substantial a.c. signal at the junction, one needs to increase a.c. bias by orders of magnitude to compensate for the filtering. This a.c. bias leads to substantial dissipation in the environment, its overheating and destruction of the synchronization by the thermal noise generated by this overheating. This is likely explanation of the fact that a prominent Coulomb blockade feature at d.c. bias does not give rise to high-quality synchronization if a.c. bias is applied. In contrast to this, the a.c. gate voltage signal propagates in low-resistance environment and should provide much less dissipation.

In this Article, we systematically analyse the phenomenon in the quasiclassical limit corresponding to the limit of high impedance mostly concentrating on the peculiarities of current plateaux. We distinguish three regimes. (i) A strong coupling regime corresponds to the limit of small gate capacitance C as compared to effective phase-slip junction capacitances. Most experimental setups are in this regime [32, 34, 35]. The harmonic gate voltage modulation gives rise to multiple *integer* plateaux. We show that in this regime the width of the plateau can be made comparable with the Coulomb blockade threshold voltage even for very asymmetric junctions at sufficiently large modulation amplitudes. (ii) An intermediate coupling regime where the effects of finite gate capacitance are essential. We demonstrate the appearance of *fractional* plateaux with the width $\propto C$. This is a dual of half-integer Shapiro steps observed in Josephson SQUIDS [36].(ii) A weak coupling regime of big C_g where the gate capacitor plays the role of an effective d.c. voltage source and efficiently decouples.

For all three regimes, we analyze the effect of the thermal noise on the plateaux. We demonstrate that that integer plateaux vanish at the temperature $k_B T \approx 0.06e\Delta V$, ΔV being the plateau width in the absence of noise.

The paper is organized as follows. In the Section 5.2 we give the description of the setup and the system of equations governing its dynamics. We address the stationary regime in Section 5.3. We discuss the emergence of current plateaux in strong (Section 5.4), intermediate (Section 5.5), and weak (Section 5.6) coupling regimes. In Section 5.7 we address the finite temperature effects in all three regimes. We conclude in Section 5.8.

5.2. THE SETUP

In this Article, we address a double phase-slip junction setup (Fig. 5.1). We require two phase slip junctions in series: those can be realized lithographically as short nanowire-type constrictions in a superconducting film of a high normal-state resistance [8] (Fig.5.1b). We do not have to impose any stringent conditions on homogeneity and regularity of the materials in use: we only need the phase slip tunnelling amplitudes via the narrow parts of the setup. The tunnelling amplitudes may be due to phase slips arising uniformly in the wires, or they can be dominated by the slips in the most narrow place of the wire, or even occur in a tunnel-type Josephson junction that is formed in the wire: this is not important, as explained in [12] in more detail. Eventually, the nanowire could be a Josephson junction chain with the phase slip occurring at the weakest junction. Experimentally, the amplitude in a single junction, either left or right one, is determined from the observation of the Coulomb blockade threshold voltage, $V_{L,R}$ being the threshold voltages for the junctions of the setup. The junctions are embedded in the high-impedance environment. We took the simplest and most frequently used model of such environment: the frequency-independent

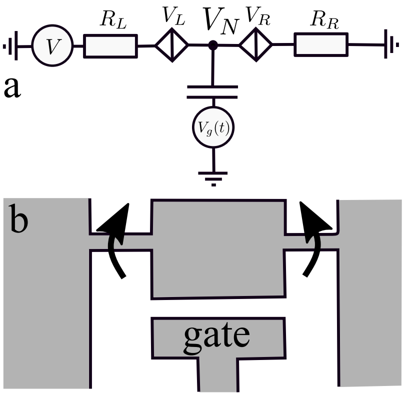

Figure 5.1: Two phase slip junctions in series in resistive environment coupled to a capacitor in between where the gate voltage is applied.

resistors $R_{L,R}$ on both sides of the double junction. The important part of the setup is the gate electrode coupled via the capacitance C to the node between the junctions.

We consider here the quasi-classical limit that is justified when the resistance exceeds by far the quantum unit, $R_{L,R}G_Q \gg 1$, $G_Q \equiv e^2/(\pi\hbar)$. In this case, the charge passed though a junction is a good classical variable subject to little quantum fluctuations. We will use a dimensionless charge $q = Q\pi/e$. In these notations, each junction can be regarded as a non-linear capacitor with the voltage drop depending on q, $V(q) = V_{L,R}\sin q_{L,R}$.

The voltage drops at the resistors are given by corresponding currents, $\frac{e}{\pi}R_{L,R}\dot{q}_{L,R}$. We assume the system is biased from the left with the voltage V. Introducing the voltage $V_N(t)$ at the node between the junctions, we equate the voltage drops as follows:

$$V_N(t) = V_R \sin q_R + \frac{e}{\pi}R_R\dot{q}_R \tag{5.1}$$

$$V - V_N(t) = V_L \sin q_L + \frac{e}{\pi}R_L\dot{q}_L \tag{5.2}$$

Each of these two equations is equivalent to a standard voltage-biased single-junction equation. The coupling between the junctions comes about the fact that the voltage at the node $V_N(t)$ also depends on the charge accumulated at the capacitor C . It is also contributed by the gate voltage,

$$V_N(t) = \frac{e}{\pi}\frac{q_L - q_R}{C} + V_g(t) \tag{5.3}$$

In the weak coupling limit $C \to \infty$ the capacitor efficiently uncouples the phase-slip junctions 5.6. In the opposite limit of strong coupling (5.4), the two phase-slip junctions effectively work as one with an amplitude that is the some of the two. The interference of two amplitudes can be tuned by gate voltage.

Now we can account for the voltage noise coming from the thermal fluctuations in the large resistors. The noise gives a stochastic addition $\xi(t)$ to the voltage drop at a resistor satisfying $\langle\xi(t)\xi(t')\rangle = 2k_B TR\delta(t-t')$. The resulting system of equations which we analyze in Article thus reads:

$$\begin{cases} \frac{e}{\pi} R_L \dot{q}_L = V - V_L \sin q_L - V_N(t) + \xi_L(t) \\ \frac{e}{\pi} R_R \dot{q}_R = V_N(t) - V_R \sin q_R + \xi_R(t) \\ V_N(t) = \frac{e}{\pi} \frac{q_L - q_R}{C} + V_g(t) \end{cases} \tag{5.4}$$

These are the stochastic evolution equations for two variables q_R, q_L.

Owing to the duality mentioned, a similar set of equations describes a Josephson junction system in a low-impedance environment. This system is a d.c. current-biased two-junction SQUID with an extra inductance in the loop subject to a time-dependent flux penetrating the loop (a dual of the time-dependent gate voltage). Such Josephson circuits have been studied in [36, 37] but, to our knowledge, have not been put into practice.

5.3. STATIONARY REGIME

In this Section, we shortly describe and illustrate the stationary regime where both bias and gate voltage do not depend on time. Let us start with Colomb blockade when (in the absence of noise) no current is flowing till the bias voltage V reaches a certain threshold value V_{th}. In Coulomb blockade regime, $V = V_L \sin q_L + V_R \sin q_R$, and the charges $q_{L,R}$ are related by

$$q_L - q_R = -q_g + \frac{\pi C V_R}{e} \sin q_R \tag{5.5}$$

where we have introduced the gate-induced charge $q_g \equiv \pi C V_g / e$. The periodicity of $\sin q_{L,R}$ implies the periodicity of the results for V_{th} in q_g, that is, in gate voltage.

These results also depend on the ratio between the gate capacitance and effective capacitance of the phase-slip junctions. We will use the dimensionless parameter

$$\tilde{C} = \frac{\pi C (V_L + V_R)}{2e} \tag{5.6}$$

to characterize the ratio and distinguish the regimes.

The strong coupling regime corresponds to small $\tilde{C}$. In this case, two phase-slip junctions are equivalent to a single junction. The difference $q_R - q_L$ is set to q_g, and the overall phase-slip amplitude is a sum of two amplitudes corresponding to tunneling in the junctions,

$$Am = V_L e^{iq_L} + V_R e^{iq_L + iq_g} \tag{5.7}$$

The gate voltage controls the relative phase shift and thus the interference of two amplitudes. The threshold voltage is determined by the maximum modulus of this amplitude,

$$V_{\mathrm{th}} = \sqrt{V_R^2 + V_L^2 + 2 V_R V_L \cos q_g} \tag{5.8}$$

The threshold vanishes at $V_L = V_R$, $q_g \mathrm{mod} 2\pi = \pi$ as the result of destructive interference.

The large capacitance effectively decouples the phase slips in the junctions, so in the opposite regime of weak coupling $\tilde{C} \gg 1$ the threshold voltage is thus a sum of two thresholds plus a a small periodic correction:

$$\frac{V_{\mathrm{th}}}{V_L + V_R} = 1 - \frac{\bar{q}_g}{2\tilde{C}}, \tag{5.9}$$

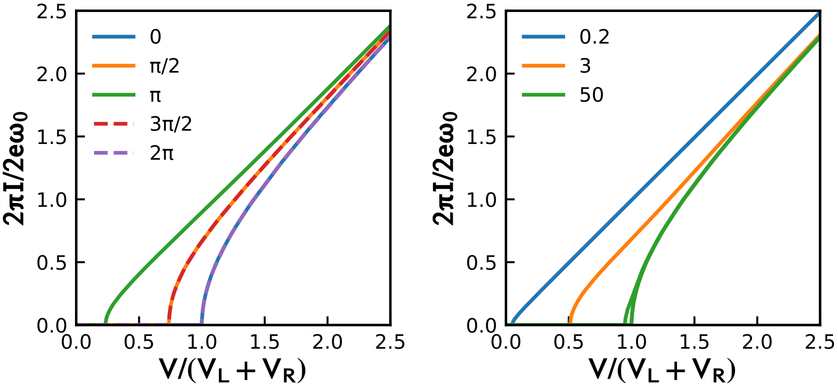

Figure 5.2: I-V characteristics in stationary regime. Symmetric setup, $R_L = R_R$, $V_L = V_R$. Left: Intermediate coupling, $\tilde{C} = 1$. The labels give the gate-induced charge q_0. The Coulomb blockade threshold is modulated by q_0, but does not vanish at $q_0 = \pi$ owing to finite $\tilde{C}$. Right: I-V characteristics for $q_0 = 0, \pi$ and three different $\tilde{C}$ shown in the labels. The curves collapse at q_0, which is the peculiarity of the symmetric setup. The minimum threshold approaches the maximum one upon increasing $\tilde{C}$ manifesting the weak coupling regime.

$\bar{q}_g \equiv (\pi C V_R/e - q_g)\text{mod}2\pi$.

If the bias voltage exceeds the threshold, a d.c. current I flows in the circuit. It is accompanied by a.c. (Bloch) oscillations with the frequency $\omega_B = \pi I/e$ corresponding to the d.c. current. We obtain the I-V characteristics by solving the system 5.4 at given V, V_g at a long time interval $(0, t)$ and calculating the time-averaged current from $I = (q_{L,R}(t) - q_{L,R}(0))/t$. The characteristics evaluated are shown in the Figure 5.2.

We see that I-V curves qualitatively follow the same shape typical for a single junction: a sharp square-root rise immediately after threshold and Ohmic behaviour $I = V/(R_R + R_L)$ at $V \gg V_{L,R}$. The threshold is however modulated by the gate voltage. We measure the current in units of $2e\omega_0$, ω_0 being the frequency scale determined by the phase slips,

$$\omega_0 = \frac{\pi}{e}\frac{V_L + V_R}{R_L + R_R} \tag{5.10}$$

and change the definition of q_g to compensate for the average V_N in Ohmic regime,

$$q_0 = \frac{\pi C}{e}\left(\frac{R_R}{R_L + R_R} V - V_g\right) \tag{5.11}$$

In the left pane of the Figure 5.2 we plot the $I - V$ characteristics for the intermediate coupling $\tilde{C}$ at several q_0. The threshold is modulated by the gate voltage but does not vanish even for the symmetric case considered since the finite capacitance effects suppress the destructive interference, its minimum value being $\approx 0.2(V_L + V_R)$. In the right pane of the Figure 5.2 we plot the $I - V$ curves at various $\tilde{C}$ at $q_0 = 0, \pi$. At $q_0 = 0$ maximizing the threshold all characteristics are the same: this is a peculiarity of the symmetric case. At $q_0 = \pi$ the threshold changes from almost zero to almost maximum value upon decreasing the capacitance and thus decoupling the junctions.

5.4. PLATEAUX IN STRONG COUPLING REGIME

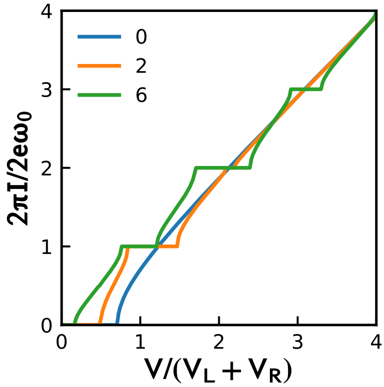

Figure 5.3: I-V characteristics in the strong coupling regime, $\tilde{C} = 0.2$, for the different gate voltage amplitudes A shown in the labels. The setup is symmetric, $q_0 = \pi/2$, and $\omega = \omega_0$. Upon increasing the amplitude, the current plateaux develop at the multiples of the modulation frequency $I_k = ke\omega/\pi$.

The most important application of the circuit is the synchronization of Bloch oscillations with an extra external a.c. signal of frequency ω. Without such signal, the solutions of the dynamical equations are degenerate with respect to the phase of the oscillations owing to time translation symmetry. The a.c. signal breaks the symmetry and the phase locks with that of the signal. In the d.c. measurement this is manifested as a current plateau: the d.c. current does not depend on the bias voltage in a certain interval of the voltages of the width ΔV, and the value of the current is determined by the frequency only. In this Section and two following ones we explore the current plateaux in strong, intermediate and weak coupling regimes respectively. We consider the periodic modulation of the gate voltage, concentrating on harmonic one: $q_g(t) = q_0 + A\sin(\omega t)$.

Some examples of $I - V$ characteristics are shown in Fig. 5.3. We observe the current plateaux at multiples of the modulation frequency $I_k = ke\omega/\pi$. The width of the plateau $\simeq (V_L + V_R)$ at $A \simeq 1$. At small A, the width of the k-th plateau scales as A^k. The width is a non-monotonous function of A.

Let us derive an analytical expression for the width of the plateaux in the limit of $k\omega \gg \omega$). It follows from Eq. 5.3 that the limit $C \to 0$ $q_R = q_L + q_g(t)$. Let us separate q_g into time-independent and oscillating part, $q_g(t) = q_0 + \tilde{q}_g(t)$. Let us introduce a convenient variable

$$q = r_L q_L + r_R q_R + q_0(r_R - r_L - 1/2) \tag{5.12}$$

where $r^{R,L} = R_{R,L}/R_\Sigma$, Summing up Eqs. 5.1, we obtain a convenient equation for this variable,

$$\frac{e}{\pi} R_\Sigma \dot{q} + \mathrm{Im}\left[e^{iq} Am(t)\right] = V \tag{5.13}$$

where the effective phase-slip amplitude $Am(t)$ reads

$$V_L e^{-iq_0/2} e^{-i\tilde{q}^R(t)} + V_R e^{iq_0/2} e^{i\tilde{q}^L(t)}; \tag{5.14}$$

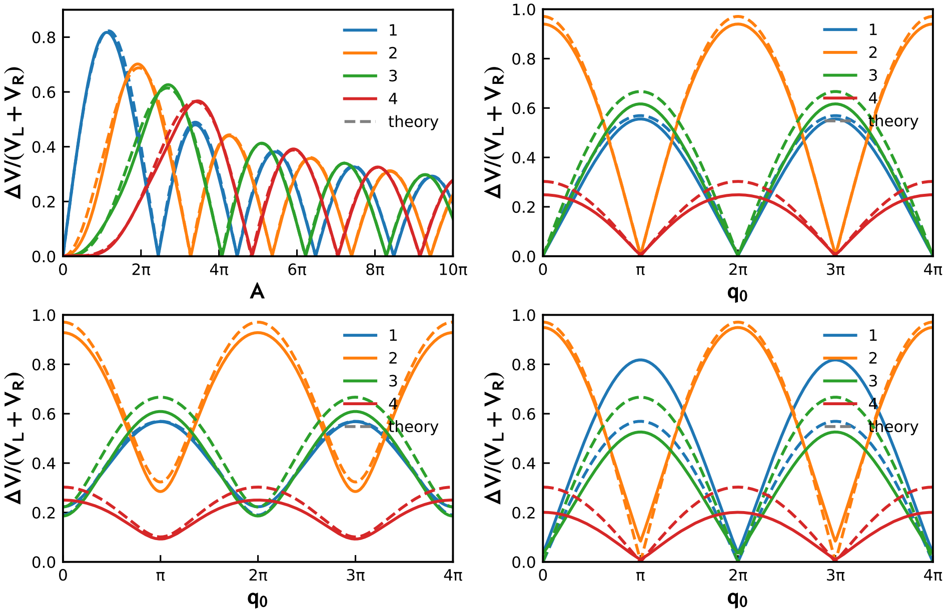

Figure 5.4: Strong coupling limit. The width of the current plateaux at $\omega = 2\omega_0$. The Figures a, b, d are for symmetric setup. For Figures a, b, c $\tilde{C} = 0.05$. The high-frequency Bessel approximation (Eqs. 5.18,5.60) given by dashed lines. a. Width of several integer plateaus in symmetric case versus the driving amplitude at $q_0 = \pi/2$. The curves are close to the high-frequency Bessel approximation. b. The widths versus q_0 for the constant amplitude $A = 2\pi$. The destructive interference in the symmetric setup manifests as zero width and a cusp at the values $q_0 = 0, \pi$ for odd and even plateaux respectively. c. Same as in b. for a slightly asymmetric setup, $V_R = 2V_L$. d. Same as in b., the capacitance is increased to $\tilde{C} = 1$.

$\tilde{q}_g^{R,L} \equiv r_{R,L}\tilde{q}_g$.

We concentrate on $V \gg (V_L + V_R)$ and $\pi V/eR_\Sigma$ close to $k\omega$. We will search for the solution in the form (see e.g. [38])

$$q = k\omega t + \psi(t) \tag{5.15}$$

assuming the separation of time scales (see e.g. [38]), that is, the phase ψ to change slowly on the scale of ω. Substituting Eq. 5.15 to Eq. 5.13 and averaging over the short time scale, we obtain an evolution equation for this slow phase

$$\frac{e}{\pi} R_\Sigma \dot{\psi} + \mathrm{Im}\left[e^{i\psi}\overline{Am_k}\right] = \delta V, \tag{5.16}$$

$\delta V = V - (e/\pi) R_\Sigma k\omega$, and $\overline{Am_k}$ is the result of averaging the amplitude over the oscillation period,

$$\overline{Am_k} = \int_0^{2\pi/\omega} dt Am(t) e^{ik\omega t}. \tag{5.17}$$

The Eq. 5.16 has stationary solution for ψ provided $|\delta V| < |\overline{Am_k}|$. This implies that the frequency of the oscillations in this voltage interval does not change being locked to $k\omega$.

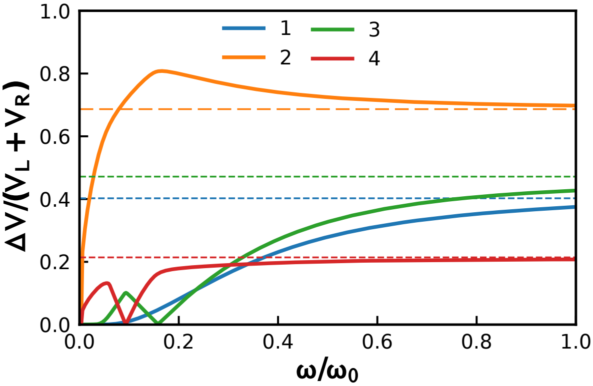

Figure 5.5: The frequency dependence of the plateau width for several integer platueax(see the labels). Strong coupling regime $\tilde{C} = 0.2$, $q_0 = \pi/2$, symmetric setup, the gate charge amplitude $A = 2\pi$. The high-frequency limits (Eq.5.18,5.60) are given by dashed lines. The high-frequency approximation given (formula 5.18) is given by dashed lines. We see that the limit is achieved at $\omega \approx \omega_0$ for all pleateaux. The width is the high-frequency approximation is valid for all steps. The width decreases to zero at lower frequencies, with some non-monotonous Bessel-like dependence.

The width of the plateau is thus given by

$$\Delta V_k = 2|\overline{Am}_k| = 2|V_L e^{-iq_0/2} J_k(A_R) + V_R e^{iq_0/2} J_k(-A_L)| \tag{5.18}$$

where in the last equation we have specified to the harmonic gate voltage signal,$A_{R,L} \equiv r^{R,L}A$, J_k being the Bessel function of the order k. For symmetric case $R_R = R_L$, $V_L = V_R = V_\Sigma/2$, this becomes

$$\Delta V_k = 2V_\Sigma J_k(A/2) \begin{cases} |\cos(q_0/2)|, & \text{if } k \text{ is even} \\ |\sin(q_0/2)|, & \text{if } k \text{ is odd} \end{cases} \tag{5.19}$$

We thus have selection rules in this case: no odd plateaux at q_0, no even plateaux at $q_0 = \pi$.

Although the expression (5.18) is formally valid only in the limit $k\omega \gg \omega_0$, we find numerically that it gives qualitatively good estimations for all $\omega \simeq \omega_0$. We extract the plateau widths from numerical data finding the voltages at which the relative deviation of the current from the quantized value amounts to 10^{-3} and associating those with the endpoints of the locking interval.

We present the numerical results for $\omega = 2\omega_0$ in Fig. 5.4 in comparison with Eqs. 5.60, 5.18. Fig. 5.4a gives the widths versus the driving amplitude A for the symmetric setup at $q_0 = \pi/2$ so that the plateaux of both parities are developed. As we see, the actual widths coincide with Bessel function prediction with the accuracy of several per cent. In Fig. 5.4 b, we plot the widths versus q_0 at constant driving amplitude. We observe the selection rules mentioned: the width drops to 0 with the plotting accuracy for $q = 0$ and odd plateaux, and for $q_0 = \pi$ and even plateaux, manifesting the descructive interference of the phase slips. The curves make a cusp at this values of q. As we see in Fig. 5.4c, the curves are smooth and do not reach 0 if we depart from the symmetric case ($V_L/V_R = 2$ in this Figure). It is interesting to note that if we decrease the capacitance moving towards the intermediate coupling regime, ($\tilde{C} = 1.0$ for Fig. 5.4 d), the cusps in the symmetric case do not dissapear but visibly depart from 0. Thus the small decoupling of the phase slips supresses the destructive interference. This is consistent with the results for the Coulomb blockade threshold voltage described in the previous Section.

The analytical expressions for widths given by Eqs. 5.18, 5.60 do not depend on frequency. This should not be valid for sufficiently small frequency. Indeed, we see that the plateaux disappear in the limit of $\omega \ll \omega_0$. in the limit of small frequency. (Fig. 5.5) We also see that the high-frequency limit is achieved already at $\omega \approx \omega_0$ for all plateaux and the frequency dependence is generally non-monotonous resembling the Bessel-like dependence on the amplitude.

5.5. FRACTIONAL PLATEAUX IN INTERMEDIATE COUPLING REGIME

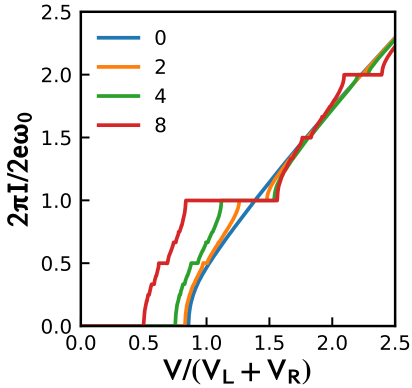

Figure 5.6: Indermediate coupling regime $\tilde{C} = 5$. Symmetric setup. I-V characteristics for $q_0 = \pi/2$ and several different driving amplitudes A given in the labels. In addition to the integer plateaux, we see the emergence of smaller fractional plateaux at $I_{MN} = (e/\pi)\omega \frac{M}{N}$.

In this Section, we will discuss the intermediate coupling regime $\tilde{C} \simeq 1$. Typical I-V characteristics with driving are presented in Fig. 5.6. A striking difference from the strong coupling regime is the appearance of smaller current plateaux at integer fractions of $e\omega/\pi$. In principle, we expect a plateau at any rational fraction $I_{MN} = (e\omega/\pi)M/N$, M, N being integer, so that the actual I-V characteristics resemble Cantor function and is an example of devil's staircase [39]. In practice, the plateau widths become exponentially small upon increasing N so only several fractional plateaux are visible. In our numerics, we were able to detect the features up to $N = 7$. The fractional plateaux are best visible for $\tilde{C} \simeq 5 - 10$ and will gradually disappear upon further increase of capacitance, see the next Section.

To understand the emergence of fractional plateaux analytically, we will develop a perturbation theory in terms of small $\tilde{C}$. To simplify the derivations, we resort to the fully symmetric setup ($R_L = R_R = R_\Sigma/2$, $V_L = V_R = V_\Sigma/2$).

It follows from Eqs. 5.3, 5.1 that the first-order correction in $\tilde{C}$ to Eq. 5.13 can be presented as a small change of the gate charge

$$q_g(t) \to q_g(t) - \frac{\pi C}{2e}\left(\frac{e}{2\pi}R_\Sigma \dot{q}_g(t) + V_\Sigma \sin\frac{q_g(t)}{2}\cos q\right) \tag{5.20}$$

The first term in the addition is an insignificant modification of the signal while the second term brings higher harmonics of e^{iq} into the Eq. 5.13 that becomes

$$\frac{e}{\pi}R_\Sigma \dot{q} = V - V_\Sigma \cos\frac{q_g(t)}{2}\sin q - V_F \sin^2\frac{q_g(t)}{2}\sin 2q. \tag{5.21}$$

Here $V_F \equiv \pi C V_\Sigma^2/8e$, $V_F \ll V_\Sigma$, and the third term represents a relevant correction responsible for emergence of the half-integer plateaux. A similar equation has been studied in the context of fractional Shapiro steps. [36] Further orders in $\tilde{C}$ would provide the terms $\propto e^{iNq}$ with $N > 2$ that will account for the plateaux at higher fractions.

We analyze this in the limit of high frequencies searching for the solutions in the form (c.f. Eq.5.15)

$$q = (k+1/2)\omega + \psi(t) \tag{5.22}$$

$\psi(t)$ being the slow-varying phase. We can neglect the second term in Eq. 5.5 since it averages out over the period. The resulting equation for the phase is contributed by the third term,

$$\frac{e}{\pi}R_\Sigma \dot{\psi} + \mathrm{Im}\left[e^{2i\psi}\overline{Am}_k^{(2)}\right] = \delta V \tag{5.23}$$

where

$$\overline{Am}_k^{(2)} \equiv \frac{V_F\omega}{2\pi}\int_0^{\frac{2\pi}{\omega}} dt \sin^2\frac{q_g(t)}{2} e^{i(2k+1)\omega t}. \tag{5.24}$$

This gives the width of the half-integer plateau

$$\Delta V_{k+1/2} = V_F |J_{2k+1}(A)||\sin q_0| \tag{5.25}$$

which is parametrically smaller than V_Σ in the limit $\tilde{C} \to 0$ and is of the order of V_F in the intermediate coupling regime.

This gives an accurate prediction at high frequencies $\omega \gg \omega_0$. To investigate the half-integer phase-slips at lower frequencies, we build up a more complex perturbation theory in $\tilde{C}$. This relies on a heuristic assumption, however, it accurately and adequately describes complex numerical data (see Fig. 5.7).

To start with the low-frequency perturbation theory, we would need to solve the unperturbed equation

$$\frac{e}{\pi}R_\Sigma \dot{q} = V - V_\Sigma \cos\frac{q_g(t)}{2}\sin q \tag{5.26}$$

We cannot find an explicit analytical solution. Instead, we use a solution $q_\star(t)$ of an *autonomous* equation obtained by the averaging of $\cos(q_g(t)/2)$ over the period,

$$\frac{e}{\pi}R_\Sigma \dot{q}_\star = V - V_\Sigma \bar{f}\sin q_\star, \tag{5.27}$$

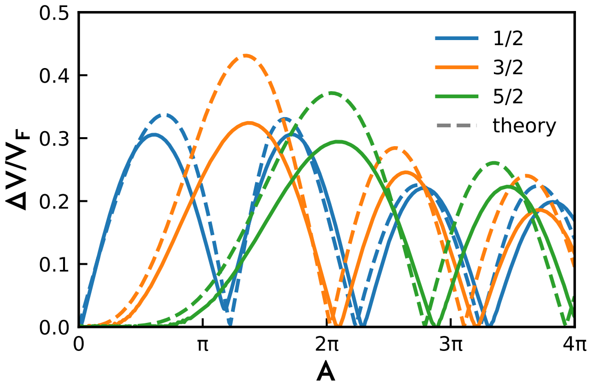

Figure 5.7: The widths of the half-integer plateaux 1/2, 3/2, and 5/2 versus the driving amplitude. Symmetric setup, $\omega = 2\omega_0$, $q_0 = \pi/2$, $\tilde{C} = 0.2$. The numerical results (solid lines) are in good correspondence with the semi-analytical prediction (Eq.5.30, dashed lines)

$\bar{f} = J_0(A/2)\cos(q_0/2)$.This equation can eventually be solved [38] and we write the solution in the form

$$\frac{dt}{dq_\star} = \frac{V - V_\Sigma \cos(\Omega t + \psi)}{\Omega^2 \pi R/e} \tag{5.28}$$

where the frequency of autonomous oscillations

$$\Omega = \pi \frac{\sqrt{V^2 - V_\Sigma^2 \bar{f}^2}}{eR} \tag{5.29}$$

. We are interested in Ω close to $M\omega/2$, M being odd. We substitute the expression 5.28 to Eq.5.5 and derive an equation for the slow-varying phase that is similar to Eq. 5.23. This finally gives a semi-analytical expression for the plateau width:

$$\frac{\Delta V_{M/2}}{V_F} = \frac{(\pi R/e) M^2}{V \omega_0 \bar{f}^2} (\max_{\phi} - \min_{\phi}) \left\{ M \frac{\omega}{\omega_0} \sin\frac{q_0}{2} \sum_{kM \in odd} J_{kM}(A) \left(\frac{\bar{f}}{y}\right)^{2k} \sin(2k\phi) \right.$$
$$\left. - M \frac{\omega}{\omega_0} \cos\frac{q_0}{2} \sum_{kM \in even} J_{kM}(A) \left(\frac{\bar{f}}{y}\right)^{2k} \cos(2k\phi) - \frac{\kappa}{2}(1 - J_0(A)\cos\frac{q_0}{2}) J_M(A) \cos\frac{q_0}{4} \sin\phi \right\} \tag{5.30}$$

where

$$y = \sqrt{V/V_\Sigma - \bar{f}^2} + V/V_\Sigma;\ w = \Omega/\omega_0;\ v = V/V_\Sigma$$
$$\kappa = \bar{f}\left(\frac{v^2}{w^3} - 4\frac{w}{y^2}\right) - \bar{f}^3 \left(\frac{2v}{3y^2 w} + \frac{v(w+y)}{w^3 y^2}\right)$$

This coincides with Eq. 5.25 in the limit of high frequencies and diverges at $\omega \to 0$ invalidating the perturbation theory in this limit.

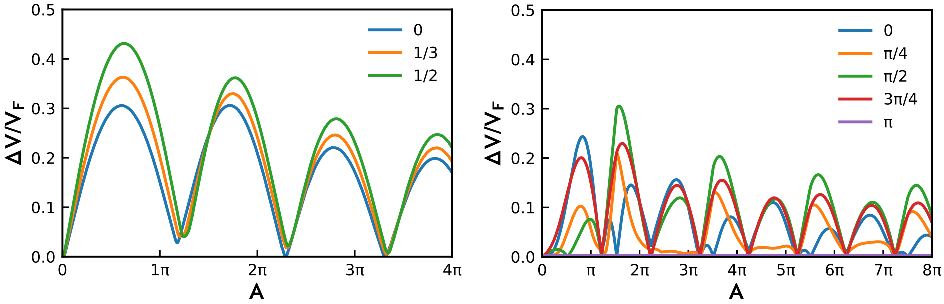

Figure 5.8: The widths of 1/2 plateau in dependence on asymmetry of the junctions and q_0, $\omega = 2\omega_0$, $\tilde{C} = 0.2$. Upper pane: The width at $q_0 = \pi/2$ versus the driving amplitude for several values of the asymmetry parameter $(V_L - V_R)/(V_L + V_R)$ shown in the labels. Lower pane: The width at $\omega = \omega_0$ versus the driving amplitude for several values of q_0 given in the labels. The setup is symmetric. We observe a rather complex dependence coming from the contributions of various Bessel functions. The data are obtained from Eq. 5.30. No plateaux persist at $q_0 = \pi$.

In Fig. 5.7, we plot the widths of the half-integer plateux for a small capacitance $\tilde{C} = 0.1$ so we can compare them with the semi-analytical prediction obtained, Eq.5.30. The deviations such as the shift of position of the cusps, the finite width at the cusp, and the heights of maxima, arise from the higher-order terms in $\tilde{C}$.

More details about the width of the half-integer plateaux illustrating the effects of junction asymmetry and q_0 are presented in Fig.5.8.

5.6. PLATEAUX IN THE WEAK COUPLING REGIME

The weak coupling regime occurs at sufficiently big capacitances, $\tilde{C} \gg 1$. In this limit, the capacitor can be regarded as a voltage source that completely decouples the junctions with respect to a.c. voltage. Of course, the d.c. coupling still persist so the same d.c. current flows through the junctions, but all interference effects characterized by q_0 dependence eventually disappear in this limit as well as the fractional current plateaux. Perhaps unexpectedly, the absence of q_0 dependence does not suppress the synchronization of Bloch oscillations by the gate voltage: we see in Fig. 5.9 well-developed integer current plateaux.

To obtain the dynamical equations in this regime, we notice that the big capacitors effectively short-cuts $V_N(t)$ except zero frequency. So in this limit $V_N(t) = \tilde{V}_g(t) + \bar{V}$, $\bar{V}$ not depending on time, $\tilde{V}_g(t)$ has no d.c. component. With this, Eqs. 5.1 become :

$$\bar{V} + \tilde{V}_g(t) = V_R \sin q_R + \frac{e}{\pi} R_R \dot{q}_R \tag{5.31}$$

$$V - \bar{V} - \tilde{V}_g(t) = V_L \sin q_L + \frac{e}{\pi} R_L \dot{q}_L \tag{5.32}$$

So the equations for left and right junctions separate, each is for a single junction biased by a d.c and a.c. voltage. The only coupling is provided by $\bar{V}$ that is determined from the d.c. current conservation:

$$\bar{I}_L(V - \bar{V}) = \bar{I}_R(\bar{V}). \tag{5.33}$$

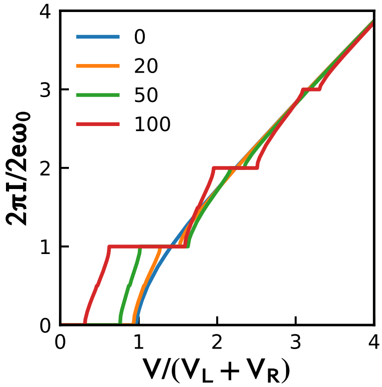

Figure 5.9: Plateaux in the weak coupling regime. Symmetric setup, $\tilde{C}=50$,$\omega=\omega_0$, $q_0=\pi/2$. The fractional plateaux are hardly visible for such values of $\tilde{C}$ while the integer plateaux remain pronounced. The labels give the induced charge modulation amplitude A as in the previous Sections. We see however the change of the scaling: the plateaux become of the order of V_L+V_R at $A\simeq\tilde{C}^{-1}$, that is, at the gate voltage modulation amplitude $\tilde{V}_g\simeq V_L+V_R$. In distinction from the strong coupling regime, the plateau width at a given amplitude is decreasing upon increasing frequency or voltage, $\Delta V\propto\omega^{-1}$.

In general situation, the solution $\bar{V}$ of this equation is formally ambiguous right at a current plateau, since at the plateau the currents do not depend on voltages. This ambiguity, however, is readily resolved if voltage noise is taken into account. As we discuss in the next Section, this results in finite differential conductance at the plateaux and unambiguous solution. In any case, the total width of a plateau is just the sum of the widths for constituent junctions,

$$\Delta V=\Delta V^L+\Delta V^R. \tag{5.34}$$

For a symmetric setup, this gives $\bar{V}=V/2$ and the $I-V$ characteristic is the same as for a single junction at half voltage and $\tilde{V}_g$ added to the bias voltage,

$$I(V)=I_{\text{single}}(V/2). \tag{5.35}$$

Let us obtain the analytical prediction for the plateau width in the limit of big frequency. We concentrate on the left junction and chose a harmonic drive:

$$\frac{e}{\pi}R_L\dot{q}=V-\bar{V}-V_L\sin q-\tilde{V}_g\sin(\omega t) \tag{5.36}$$

Near the k-th integer plateau, we neglect V_L and search the solution in the form

$$q(t)=k\omega+\frac{\pi\tilde{V}_g}{eR_L}\cos\omega t+\psi(t). \tag{5.37}$$

The resulting equation for the slow phase is very similar to Eq. 5.16:

$$\frac{e}{\pi}R_\Sigma\dot{\psi}+\text{Im}\left[e^{i\psi}\overline{Am_k}\right]=\delta V, \tag{5.38}$$

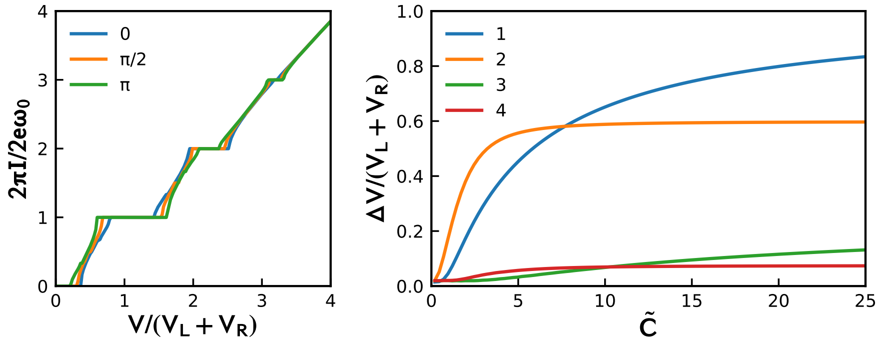

Figure 5.10: Approachig the weak coupling regime. Symmetric setup. Left: I-V characteristics at $\tilde{C} = 10$, $A = 20$ and several values of q_0 given in the labels compared with the I-V characteristic of the single junction with $\tilde{V}_g$ added to bias voltage (Eq. 5.35). All these curves should coincide in the limit $\tilde{C} \to \infty$. For finite $\tilde{C}$, we see some residual deviations modulated by q_0 and even small fractional plateaux. Right: The plateau width (in units of $V_L + V_R$ of several integer plateaux at fixed a.c amplitude $\tilde{V}_g$ (same as that on the left) versus the capacitance $\tilde{C}$. The saturation indicates the weak coupling regime, and occurs at different $\tilde{C}$ for different plateaux.

where

$$\overline{Am}_k = \frac{V_L \omega}{2\pi} \int_0^{\frac{2\pi}{\omega}} dt \exp\left(ik\omega t + i\frac{\pi \tilde{V}_g}{eR_L} \cos\omega t \right) \tag{5.39}$$

This gives the plateau width for the left junction

$$\Delta V^L = 2V_L \left| J_k\left(\frac{\pi \tilde{V}_g}{e\omega R_L} \right) \right| \tag{5.40}$$

and the overall width

$$\Delta V^L = 2V_L \left| J_k\left(\frac{\tilde{V}_g}{e\omega R_L} \right) \right| + 2V_R \left| J_k\left(\frac{\tilde{V}_g}{e\omega R_R} \right) \right| \tag{5.41}$$

This result is somewhat similar to that for the strong coupling regime (Eq. 5.41): the maximum width is restricted by $V_L + V_R$ and exhibit the Bessel-like dependence on the driving amplitude. We note however the disappearance of interference and renormalization of the arguments in the Bessel functions. The arguments are inversely proportional to ω, this reduces the widths upon increasing ω. However, much smaller amplitudes $\tilde{V}_g$ are required for the argument of the Bessel functions to be of the order of 1: if $\omega \simeq \omega_0$, $\tilde{V}_g \simeq V_{L,R}$ as opposed to $\tilde{V}_g \simeq V_{L,R}/\tilde{C} \gg V_{L,R}$ in the strong coupling regime.

The weak coupling limit described corresponds to $\tilde{C} \to \infty$, and at any finite capacitance up to $\tilde{C} \simeq 10^2$ there are still noticeable deviations. We illustrate this in Fig. 5.10. In the left pane, we plot $I - V$ characteristics at different q_0 for $\tilde{C} = 10$. The q_0 dependence should be absent in the weak coupling limit, and the curves should collapse on the single-junction $I - V$ characteristic. We see, however, sizeable deviations and even small fractional plateaux. In the right pane, we plot the widths of the integer plateaux at fixed gate voltage modulation amplitude $\tilde{V}_g$ (since $A \propto \tilde{C}$, the widths vanish at $\tilde{C} \to 0$. The widths should saturate in the weak coupling limit. We see that the saturation is slow and also different for different plateaux.

5.7. FINITE TEMPERATURE EFFECTS

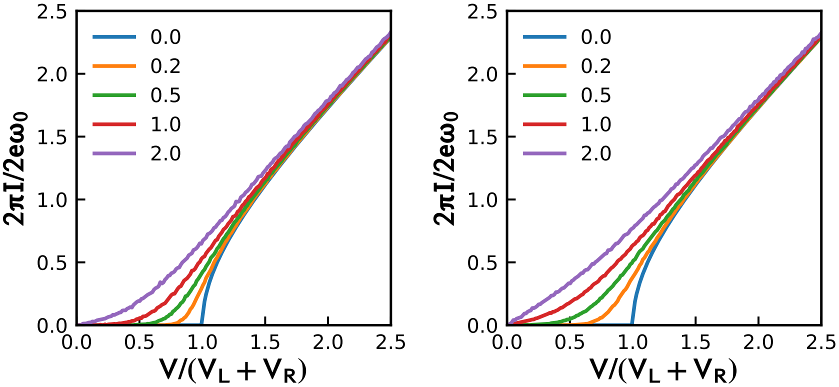

Figure 5.11: Smoothing of the Coulomb blockade feature by finite temperature. I-V characteristics for several dimensionless temperatures $\tilde{T} = 8\pi k_B T/eV_\Sigma$. Symmetric setup, $q_0 = 0$. Left: $\tilde{C} = 0.1$, strong coupling regime. Right: $\tilde{C} = 50$, weak coupling regime. Upon increasing the temperature, we see first the rounding of the sharp feature at the threshold, them finite conductance at zero voltage and finally a linear I-V characteristic. The same degree of smoothening in the weak coupling regime occurs at approximately half of the temperature at which it occurs in the strong coupling regime.

In the previous Sections, we neglected the finite temperature that in our semiclassical model is manifested as a white voltage noise. This permitted us to concentrate on ideal synchronization, sharp Coulomb blockade and plateau features. In this Section, we investigate how the synchronization is gradually destroyed by noise. This is manifested as gradual smoothing eventual disappearance of blockade and plateau features. This study is especially relevant in the setups including large resistors in view of the dissipation and resulting overheating of the resistors. We numerically solve the Eqs. 5.4at large time intervals to obtain the I-V characteristics with and without modulation. The main goal of this study is to come up with approximate but practical estimations of the temperatures at which the plateaux are still observable. With this, we can also draw semi-quantitative predictions beyond semi-classics using the correspondence between the thermal and quantum noise at a plateau developed by modulation with the frequency ω [15] : $k_B T = \hbar\omega$.

We present first the finite temperature effect on the Coulomb blockade feature in the absence of the a.c. modulation (Fig. 5.11). The temperature scale at which Coulomb blockade deteriorates should correspond to the Coulomb energy eV_Σ. We incorporate this introducing a dimensionless temperature $\tilde{T} \equiv 8\pi k_B T/eV_\Sigma$. The smoothing of the Coulomb blockade for our setup is qualitatively similar to the smoothing of I-V characteristics in common Coulomb blockade: at low temperatures, the sharp corner at the threshold is rounded at the scale of this low temperature while the differential conductance remains strongly suppressed; at medium temperatures, the low-voltage conductance becomes a fraction of R^{-1}; at higher temperatures, the Coulomb blockade feature disappears and the I-V characteristics is almost linear. In Fig. 5.11, we compare the results for strong and weak coupling regimes choosing $q_0 = 0$ where the Coulomb blockade thresholds are maximized and equal in both limits. We see that for the symmetric setup the

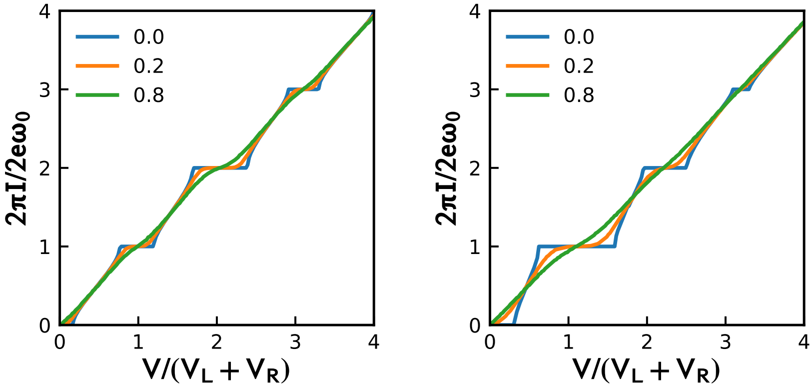

Figure 5.12: Smoothing of current plateaux at finite temperature. I-V characteristics of symmetric setup under gate voltage modulation with $\omega = \omega_0$ at dimensionless temperatures $\tilde{T}$ shown in the labels. Left: strong coupling regime, $\tilde{C} = 0.2$, $q_0 = \pi/2$, the induced charge modulation $A = 6$. Left: weak coupling regime, $\tilde{C} = 50$, the voltage gate modulation $A = 100$ with $q_0 = \pi/2$. At the same temperature, the degree of smoothing is bigger for the plateaux of smaller width. The same degree of smoothing in the weak coupling regime occurs at twice smaller temperature as compared with the strong coupling regime.

same degree of smoothing in the weak coupling regime requires twice smaller temperature as compared to the strong coupling regime. This is explained by the fact that the height of the Coulomb barrier is twice smaller in the weak coupling regime. Indeed, since the junctions are uncoupled, the Coulomb barriers are determined by $eV_{L,R}$ as compared to $e(V_L + V_R)$ in the strong coupling regime.

The smoothing of the well-developed integer plateaux with $\Delta V \simeq V_\Sigma$ follows the same pattern (Fig. 5.12). Also here the same degree of smoothing occurs at approximately twice smaller temperature in the weak coupling regime. One can see it, for instance, for the second plateau that is slightly wider in the weak coupling regime but is more smoothed at the same temperature. We also see that the smaller plateaux are smoother at the same temperature. This leads us to a simple scaling hypothesis: for each plateau, the degree of smoothing is defined by the temperature relative to the plateau width (c.f. [38]). To check the hypothesis, we need to choose a measure of smoothing.

To do this, we note that a common experimental signature of imperfect plateaux are the peaks in differential resistance. Typical current dependences of the differential resistance for various temperatures are plotted in Fig. 5.13. There, we see the peaks at the quantized values of the current that diverge at vanishing temperature, take finite value at finite temperatures and eventually merge with the background $\approx R_\Sigma$ at higher temperatures. We define the width of the plateaux at finite temperature as the length of the voltage interval where the differential conductance exceeds the background resistance at least by a factor of Q, and choose $Q = 3$. With this definition, the plateau widths becomes zero at some critical temperature where the peak differential resistance is thrice the background. Despite the arbitrariness of this definition, it seems to be a reasonable practical compromise. To extract so-defined width numerically, we change voltage in small steps near the quantized values of the current checking the differential conductance at each step.

The simple scaling hypothesis would imply that the temperature-dependent width in

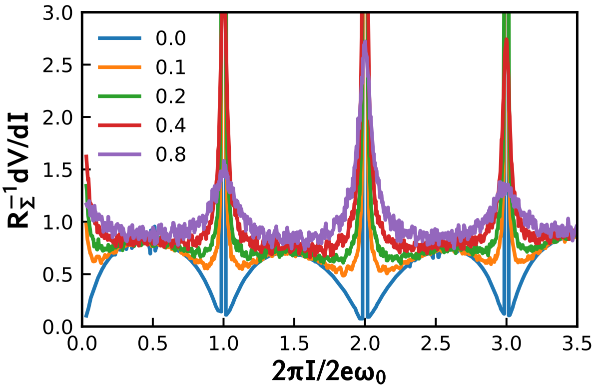

Figure 5.13: The differential resistance versus current. Symmetric setup, $\tilde{C} = 0.2$, a.c. voltage modulation at $\omega = \omega_0$, $A = 6$, the dimensionless temperature $\tilde{T}$ is given in the labels. The resistance is obtained numerically from I-V characteristics taken at discrete values of voltage with the current step $0.03\frac{2e\omega_0}{2\pi}$. The noise in the data comes from the actual noise: To obtain I-V curves, we average the current over a finite time interval picking up its fluctuations. The smoothed plateaux are manifested as the peaks of differential resistance. The height of the peaks decreases with increasing temperature. We define the "width" of the plateau at finite temperature as the length of the voltage interval where the differential resistance exceeds the background differential resistance $\simeq R$ by at least a factor of 3.

units of zero-temperature width is a universal function of temperature in units of the zero-temperature width,

$$\frac{\Delta V(T)}{\Delta V(0)} = f\left(\frac{k_B T}{e\Delta V(0)}\right) \tag{5.42}$$

To check the hypothesis, we plot the evaluated widths of several plateaux in coordinates $\Delta V(T)/\Delta V(0)$, $\tilde{T}V_\Sigma/\Delta V(0)$. We plot the data both for strong and weak coupling regime, correcting the temperature by a factor of 2 in for the latter case. We see a good collapse of the data into a single curve despite significantly different widths of the plateaux. We concude that the width of a plateau is halved at $k_B T \approx 0.03 e\Delta V(0)$ and vanishes at

$$k_B T_c \approx 0.06 e\Delta V(0). \tag{5.43}$$

The suggested scaling is not exact in any obvious limit, in fact, since we have to correct the weak coupling regime data, it would not work in between the regimes at $\tilde{C} \simeq 1$. Albeit it seems to work empirically.

To convert it into a quantum noise estimation, we substitute $k_B T_c = \hbar\omega$ and $\omega = \omega_0$. This gives a minimum value of the resistance R_Σ at which the plateau is still observable,

$$R_c \approx 16\frac{\pi\hbar}{e^2}\frac{V_\Sigma}{\Delta V(0)}. \tag{5.44}$$

Being encouraged with the success of the simple scaling hypothesis for the integer plateaux, we analyse the effect of finite temperature on the fractional plateaux in the intermediate regime $\tilde{C} \simeq 1$. The results are presented in Fig. 5.15. We observe there pronounced fractional plateaux at vanishing temperature, with the width up to $\simeq 0.1 V_\Sigma$.

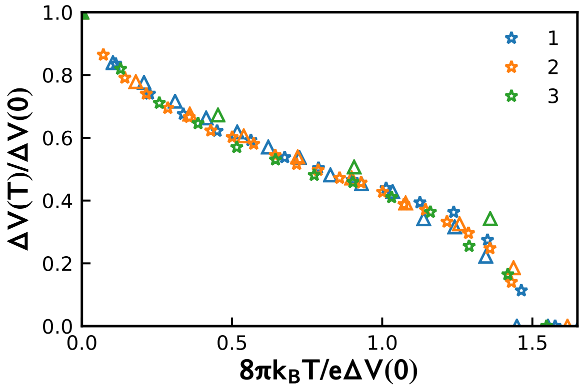

Figure 5.14: The scaling of the integer plateau smoothing with temperature. We check a simple scaling hypothesis $\Delta V(T)/\Delta V(0) = f(k_B T/eV(0))$ and see the data collapsing into the same universal curve for both weak and strong coupling regime and various plateaux. For the weak coupling regime, we correct the temperature by a factor of 2. The data for the strong coupling regime ($\tilde{C} = 0.2$, $A = 6$, $q_0 = \pi/2$) are plotted with stars, those for the weak coupling regime ($\tilde{C} = 50$, $A = 100$) are plotted with trianlge, the color of the star/triangle corresponds to first, second, third plateau as shown in the labels, $\omega = \omega_0$ for all situations.

However, they vanish rather quickly, at the temperatures of two orders of magnitude lower than the integer ones. One could think that this is due to smaller width of the plateaux, so we check the simple scaling hypothesis plotting the temperature-dependent width in coordinates $\Delta V(T)/\Delta V(0)$, $\tilde{T} V_\Sigma/\Delta V(0)$. We do not find the correspondence with the scaling of integer plateaux: the critical temperatures in units of the width are at least by a factor of 5 lower, and decrease with increasing the denominator. There is no scaling for different fractions, even for those with the same denominators. This may be explained by the fact that the shape of the effective energy barrier for fractional plateaux is different from that for integer plateaux, and is different from fraction to fraction. In conclusion, the fractional plateaux can only be observed at temperatures by two orders of magnitude lower than the integer ones.

5.8. CONCLUSIONS

In conclusion, we propose to synchronize Bloch oscillations in a double phase-slip junction by modulating the gate voltage. This is advantageous in comparison with the bias voltage modulation since the a.c. signal does not produce extra dissipation that may kill the synchronization by overheating. We show that a.c. modulation gives rise to the pronounced plateaux of quantized current of the width V_Σ corresponding to the optimistic estimations for bias voltage modulation.

We distinguish and investigate in detail three regimes corresponding to the ratio of the gate capacitance C and effective junction capacitance V_Σ/e. The strong coupling regime $C \ll V_\Sigma/e$ is characterized by strong interference of the phase slips that is tuned by q_0, the charge induced by the d.c. part of the gate voltage. Well-developed plateaux are achieved at a.c. induced charge $\tilde{q}_g \simeq e$ corresponding to a.c. modulations The interference is suppressed in the opposite regime of weak coupling, $C \ll V_\Sigma/e$. The well-developed plateaux

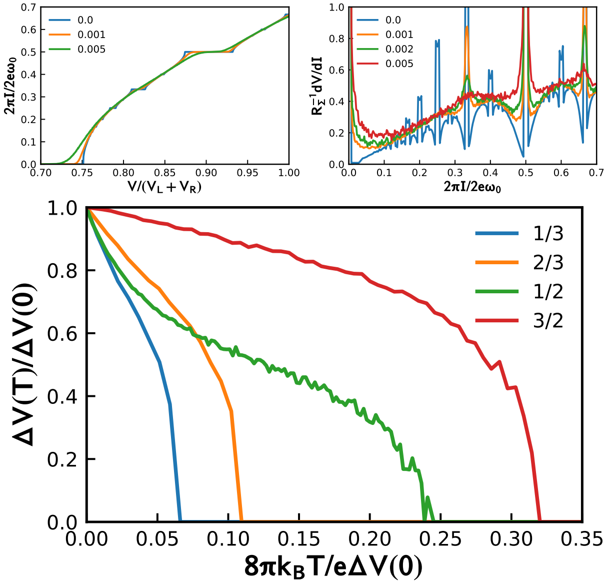

Figure 5.15: Failure of the simple scaling hypothesis for fractional plateaux. The data are for symmetric setup, $\omega = \omega_0$, $A = 4$, $q_0 = \pi/2$, $C = 5$. Upper pane left: The I-V characteristics for various dimensionless temperatures $\tilde{T}$ marked in the labels. Lower pane: Temperature-dependent plateaux width for a set of fractional plateaux versus the temperature in units of the width obtained at current step $\Delta I = 0.01\frac{2e\omega_0}{2\pi}$. In contrast to Fig. 5.14, the curves are different for different fractions: there is no universal scaling.

require bigger induced charge amplitudes $\tilde{q}_g \simeq CV_\Sigma$ but smaller gate voltage amplitudes $\tilde{V}_g \simeq V_\Sigma$. Interestingly, well-developed fractional plateaux are developed in the intermediate regime of $C \simeq V_\Sigma/e$.

We investigate the effect of finite temperature on the smoothing of plateaux in all three regimes. The smoothing of integer plateaux is found to obey an empirical scaling law: the degree of smoothing is determined by the temperature in units of the plateau width. No such scaling was found for fractional plateaux that are only observable at temperatures by two orders of magnitude lower than the integer ones.

To support open science and open software initiatives and to comply with institutional policies, we have published all relevant code and instructions for running it on the Zenodo repository [40].

5.9. APPENDIX

We analyze double phase slip junction for which we can write down governing equations assuming quantum fluctuations of charge are negligible as follows:

$$\begin{cases} \frac{e}{\pi} R_L \dot{q}_L = V - V_L \sin q_L - V_N(t) + \xi_L(t) \\ \frac{e}{\pi} R_R \dot{q}_R = V_N(t) - V_R \sin q_R + \xi_L(t) \\ V_N(t) = \frac{e}{\pi}\frac{q_L - q_R}{C} + V_g(t) \end{cases} \tag{5.45}$$

where $\langle \xi(t)\xi(t')\rangle = 2k_B T R\delta(t-t')$.

To analyze this system with a reasonable parameter space we dimensionalize it. To start we rewrite the system as follows:

$$\begin{cases} \dot{q}_L/\omega_0 = \frac{R_L+R_R}{2R_L}\left(\frac{2V}{V_L+V_R} - \frac{2V_L}{V_L+V_R}\sin q_L - \frac{2V_N(t)}{V_L+V_R}\right) + \frac{2\pi}{eR_L\omega_0}\xi_L(t) \\ \dot{q}_R/\omega_0 = \frac{R_L+R_R}{2R_R}\left(\frac{2V_N(t)}{V_L+V_R} - \frac{2V_R}{V_L+V_R}\sin q_R\right) + \frac{2\pi}{eR_R\omega_0}\xi_R(t) \\ V_N(t) = \frac{e}{\pi}\frac{q_L-q_R}{C} + V_g(t) \end{cases} \tag{5.46}$$

where $\omega_0 = \pi V_\Sigma / eR_\Sigma$.

To simplify we shall introduce dimensionless parameters $u = (V_L - V_R)/V_\Sigma$, $r = (R_L - R_R)/R_\Sigma$ which enables to consider a following system:

$$\begin{cases} \dot{q}_L = \frac{1}{1+r}\left(2\tilde{V} - (1+u)\sin q_L - \frac{1}{\tilde{C}}(q_L - q_R) - 2\tilde{V}_g(t)\right) + \tilde{\xi}_L(t) \\ \dot{q}_R = \frac{1}{1-r}\left(-(1-u)\sin q_R + \frac{1}{\tilde{C}}(q_L - q_R) + 2\tilde{V}_g(t)\right) + \tilde{\xi}_R(t) \end{cases} \tag{5.47}$$

where $\tilde{V} = V/V_\Sigma$, $\tilde{V}_g = V_g/V_\Sigma$, $\tilde{C} = \pi C V_\Sigma/2e$ and $\langle \tilde{\xi}_L(t)\xi_L(t')\rangle = \frac{\tilde{T}}{1+r}\delta(t-t')$, $\langle \tilde{\xi}_R(t)\xi_R(t')\rangle = \frac{\tilde{T}}{1-r}\delta(t-t')$ with dimensionless temperature being $\tilde{T} = 8\pi\frac{k_B T}{eV_\Sigma}$.

It is convenient to express the dimensionless gate voltage in terms of quasi-static charge on the capacitor $q_g(t)$ as follows:

$$\tilde{V}_g(t) = \frac{1-r}{2}\tilde{V} - \frac{1}{2\tilde{C}}q_g(t) \tag{5.48}$$

where q_g can be arbitrary signal. In this paper we are interested in harmonic modulation of Saphiro steps thus we choose $q_g(t) = q_0 + A\sin(\omega t)$.

5.9.1. SYMMETRIC SETUP

To analyze the system at $u = 0$, $r = 0$ let's change the variables to $q_L = q+Q$ and $q_R = q-Q$. The system for such variables reduces to (tildes are dropped):

$$\dot{q} = V - \cos Q \sin q \tag{5.49}$$

$$\dot{Q} = -\cos q \sin Q - \frac{2}{C}(Q - \frac{q_g(t)}{2}) \tag{5.50}$$

To formally analyze the system we shall expand Q in terms of capacitance $Q = Q^{(0)} + Q^{(1)} + O(C^2)$. Plugging in the second equation we would see that $Q^{(0)} = q_g(t)/2$.

For the first order we get:

$$Q^{(1)}(t) = -\frac{C}{4}(\frac{\dot{q}_g(t)}{2} + 2\sin\frac{q_g(t)}{2}\cos q) + O(C^2) \tag{5.51}$$

We thus shall substitute the solution into equation for $q(t)$:

$$\dot{q} = V - \cos\left(\frac{q_g(t)}{2} - \frac{C}{4}\left(\dot{q}_g(t) + 2\sin\frac{q_g(t)}{2}\cos q\right)\right)\sin q \tag{5.52}$$

and expand it in terms of capacitance which shall give us:

$$\dot{q} = V - \cos\frac{q_g(t)}{2}\sin q - \frac{C}{4}\sin^2\frac{q_g(t)}{2}\sin 2q + \frac{C}{4}\dot{q}_g(t)\sin\frac{q_g(t)}{2}\sin q + O(C^2) \tag{5.53}$$

5.9.2. ASYMMETRIC SETUP WITH A SINGLE PHASE SLIP

A qualitatively different dynamics raises in a completely asymmetric system where only one phase slip is present. To consider it we shall take $u = 1$ and $r = 0$ which gives us equations:

$$\begin{cases} \dot{q}_L = V - 2\sin q_L - \frac{1}{C}(q_L - q_R - q_g(t)) \\ \dot{q}_R = V + \frac{1}{C}(q_L - q_R - q_g(t)) \end{cases} \tag{5.54}$$

To solve the system perturbatively we make an expansion $q_L = q_L^{(0)} + q_L^{(1)} + q_L^{(2)} + O(C^3)$ and $q_R = q_R^{(0)} + q_R^{(1)} + q_R^{(2)} + O(C^3)$. For the zeroth order terms looking at powers of $1/C$ in the equation we obtain:

$$q_L^{(0)} - q_R^{(0)} = q_g(t) \tag{5.55}$$

Looking on the zeroth order $O(1)$ terms of the equation we get a system:

$$\begin{cases} \dot{q}_L^{(0)} = V - 2\sin q_L^{(0)} - \frac{1}{C}(q_L^{(1)} - q_R^{(1)}) \\ \dot{q}_R^{(0)} = V + \frac{1}{C}(q_L^{(1)} - q_R^{(1)}) \end{cases} \tag{5.56}$$

We can now substitute $q_L^{(1)} - q_R^{(1)}$ from the second equation in the first and obtain:

$$\dot{q}_L^{(0)} = V - \sin q_L^{(0)} + \frac{1}{2}\dot{q}_g(t) \tag{5.57}$$

which explains why in asymmetric case integer step magnitude is unaffected but modulation with q_0 disappears.

In numerics we observed the presence of fractional steps. To explain the we shall consider a first order corrections. To do so we shall use a formula:

$$\sin(q_L^{(0)} + q_L^{(1)}) = \sin q_L^{(0)} \cos q_L^{(1)} + \cos q_L^{(0)} \sin q_L^{(1)} \tag{5.58}$$

Assuming that $q_L^{(1)} \ll 1$ we can put $\cos q_L^{(1)} = 1 + O(C^2)$ giving us the corresponding equation for the first order correction to be:

$$\begin{cases} \dot{q}_L^{(1)} = -2\cos q_L^{(0)} \sin q_L^{(1)} - \frac{1}{C}(q_L^{(2)} - q_R^{(2)}) \\ \dot{q}_R^{(1)} = \frac{1}{C}(q_L^{(2)} - q_R^{(2)}) \end{cases} \tag{5.59}$$

To proceed we shall again substitute $q_L^{(2)} - q_R^{(2)}$ from the second one to the first one giving us:

$$\dot{q}_L^{(1)} = -2\cos q_L^{(0)} \sin q_L^{(1)} - \dot{q}_R^{(1)} \tag{5.60}$$

We can obtain $\dot{q}_R^{(1)}$ from the second equation 5.56 by taking time derivative which gives:

$$\dot{q}_R^{(1)} = \dot{q}_L^{(1)} - C\ddot{q}_R^{(0)} \tag{5.61}$$

To proceed we shall use equation 5.55 and rewrite the term as:

$$\dot{q}_R^{(1)} = q_L^{(1)} + C(\ddot{q}_g(t) - \ddot{q}_L^{(0)}) \tag{5.62}$$

Finally we shall use the first equation of 5.56 and obtain:

$$\ddot{q}_L^0 = -V\cos q_L^{(0)} + \frac{1}{2}\sin 2q_L^{(0)} - \frac{1}{2}\dot{q}_g(t)\cos q_L^{(0)} + \frac{1}{2}\ddot{q}_g(t) \tag{5.63}$$

which upon substitution gives us the $\dot{q}_R^{(1)}$:

$$\dot{q}_R^{(1)} = \dot{q}_L^{(1)} + \frac{C}{2}\ddot{q}_g(t) + C(V\cos q_L^{(0)} - \frac{1}{2}\sin 2q_L^{(0)} + \frac{1}{2}\dot{q}_g(t)\cos q_L^{(0)}) \tag{5.64}$$

We can now substitute this in the equation 5.60 and obtain:

$$\dot{q}_L^{(1)} = -\cos q_L^{(0)}\sin q_L^{(1)} - \frac{C}{2}\ddot{q}_g(t) - \frac{CV}{2}\cos q_L^{(0)} + \frac{C}{4}\sin(2q_L^{(0)}) - \frac{C}{4}\dot{q}_g(t)\cos q_L^{(0)} \tag{5.65}$$

The last step is to sum up the zeroth order and first order equations 5.56 and 5.65 respectively. To do so we shall use again approximation that $q_L^{(1)} \ll 1$ thus $\sin q_L^{(0)} + \cos q_L^{(0)}\sin q_L^{(1)} = \sin(q_L^{(0)} + q_L^{(1)}) + O(C^2)$ and substitute $Cq_L^{(0)} \to Cq_L + O(C^2)$ and so we get the first order equation for the system to be:

$$\dot{q}_L = V - \sin q_L + \frac{C}{4}(2V - \dot{q}_g(t))\cos q_L + \frac{C}{4}\sin 2q_L + \frac{1}{2}\dot{q}_g(t) - \frac{C}{2}\ddot{q}_g(t) + O(C^2) \tag{5.66}$$

5.9.3. Fractional steps for symmetric setup

So we are about to analyze an equation:

$$\dot{q} = V - \sin\frac{q_g(t)}{2}\sin q - \frac{C}{4}\sin^2\frac{q_g(t)}{2}\sin 2q \tag{5.67}$$

In order to simplify it we shall divide every term by $\langle\sin\frac{q_g(t)}{2}\rangle = J_0(A/2)\cos(q_0/2)$ change the frequency scale to $\omega' = J_0(A/2)\cos(q_0/2)\omega_0$ and thus arrive at equation:

$$\dot{q} = \tilde{V} - f(t)\sin q + g(t)\sin 2q \tag{5.68}$$

where $f(t) = \sin\frac{q_g(t)}{2}/\langle\sin\frac{q_g(t)}{2}\rangle$ and $g(t) = \frac{C}{4}\sin^2\frac{q_g(t)}{2}/\langle\sin\frac{q_g(t)}{2}\rangle$. Naturally it follows that $\langle f(t)\rangle = 1$ and $\langle g(t)\rangle = \frac{C}{4}\langle\sin^2\frac{q_g(t)}{2}\rangle/\langle\sin\frac{q_g(t)}{2}\rangle = \alpha$. We shall treat the $\sin 2q$ term only perturbatively and thus expand in terms of $\varepsilon = \max|g(t)|$.

The autonomous equation of this equation is:

$$\dot{q}_* = \tilde{V} - \sin q_* + \alpha\sin 2q_* \tag{5.69}$$

We can use this equation to express full solution introducing a slowly varying phase $\phi(t)$ as follows: $q(t) = q_*(t + \frac{1}{\Omega}\phi(t))$ where Ω is a period for autonomous equation. Putting that in the original equation gives us equation for the phase:

$$\frac{1}{\Omega}\dot{\phi} = \delta\tilde{V}\langle\dot{q}_*^{-1}\rangle_\Omega + \langle f(t)\frac{\sin q_*}{\dot{q}_*}\rangle_\Omega + \langle g(t)\frac{\sin 2q_*}{\dot{q}_*}\rangle_\Omega \tag{5.70}$$

where averaging is over a time $2\pi/\Omega$.

To get first order correction which determines the fractional step width we can insert zeroth order solution $\alpha = 0$ of autonomous equation in the first and third term. For the second term we need to consider first order contribution to $\sin q_*/\dot{q}_*$ which we shall denote as $\delta\left(\sin q_*/\dot{q}_*\right)$. Thus the equation for slowly varying phase for fractional frequencies ($\langle \dot{q}_*^{-1}\rangle = V/\Omega^2$):

$$\frac{1}{\Omega}\dot{\phi} = \frac{\tilde{V}}{\Omega^2}\delta\tilde{V} + G(\phi) \tag{5.71}$$

where:

$$G(\phi) = \langle f(t)\delta\left(\frac{\sin q_*}{\dot{q}_*}\right)\rangle_\Omega + \langle g(t)\frac{\sin 2q_*}{\dot{q}_*}\rangle_\Omega \tag{5.72}$$

The step width thus is:

$$\Delta\tilde{V} = \frac{\Omega^2}{\tilde{V}}(\max_\phi - \min_\phi)G(\phi,\Omega) \tag{5.73}$$

The term $\langle g(t)\frac{\sin 2q_*}{\dot{q}_*}\rangle_\Omega$

Let's first consider the second term $\langle g(t)\frac{\sin 2q_*}{\dot{q}_*}\rangle_\Omega$. To do so we need to obtain the harmonic expansion coefficients of $\sin 2q_*$ we shall use already known result for $Z = e^{iq_*}$ [15]:

$$Z = \frac{i}{y}\left(1 - 2y\Omega\sum_{k>0}\left(\frac{1}{y}e^{-i(\Omega t+\phi)}\right)^k\right), \qquad V = \frac{1}{2}(y + y^{-1}) \tag{5.74}$$

where $y > 1$.

For the derivation only the it's square is going to be needed which we can evaluate:

$$Z^2 = -\frac{1}{y^2}\left(1 - 4y\Omega\sum_{k>0}\frac{1-(k-1)y\Omega}{y^k}e^{-ik(\Omega t+\phi)}\right) \tag{5.75}$$

Now we can use it to evaluate (for $n > 0$):

$$\langle e^{in\Omega t}\sin 2q_*\rangle = \frac{1}{2i}\left(\langle e^{in\Omega t}Z^2\rangle - \langle e^{-in\Omega t}Z^2\rangle^*\right) = -\frac{2i\Omega}{y^{|n|+1}}(1-(|n|-1)y\Omega)\mathrm{sgn(n)e}^{-\mathrm{in}\phi} \tag{5.76}$$

We shall also rewrite the result in a different form:

$$\sin(2q_*) = \sum_k s_k e^{-ik\Omega t} \qquad s_k = -\frac{2i\Omega}{y^{|k|+1}}(1-(|k|-1)y\Omega)\mathrm{sgn(k)e}^{-\mathrm{ik}\phi} \tag{5.77}$$

An useful integral

$$\int^t \frac{1}{\dot{q}_*}\sin 2q_*\,dt = -\frac{2}{\Omega^3}\sum_{k>0}\frac{1}{k}\mathrm{Im(p_k e^{-ik\Omega t})} \qquad p_k = Vs_k - \frac{e^{i\phi}}{2}s_{k+1} - \frac{e^{-i\phi}}{2}s_{k-1} \tag{5.78}$$

Evaluating p_k we can find:

$$p_0 = 0 \qquad p_1 = -i\frac{\Omega}{y^2}(y(1-y\Omega)+\Omega)e^{-i\phi} \qquad p_k = \frac{2i\Omega^3}{y^k}e^{-ik\phi} \tag{5.79}$$

plugging it in we can get a formula for the integral

$$\int^t \frac{1}{\dot{q}_*}\sin 2q_*\, dt = -\frac{2(\Omega+y)}{\Omega^2 y^2}\cos(\Omega t+\phi)+4\sum_{k>1}\frac{1}{ky^k}\cos(k(\Omega t+\phi)) \tag{5.80}$$

This result had been verified numerically.

We shall now expand the signal in harmonics $g(t)=\sum_m g_m e^{im\omega t}$ and plug it in:

$$\langle\frac{dt}{dq_*}g(t)\sin 2q_*\rangle_\Omega = \sum_m g_m\langle e^{im\omega t}\frac{dt}{dq_*}\sin 2q_*\rangle \tag{5.81}$$

We know from a reasoning that for this term to be nonzero the autonomous and signal frequencies must match $m\omega = n\Omega$. We can implement this relation with a parametrization $m=kM$, $n=kN$ where N and M are integers. That allows to continue the derivation:

$$\begin{aligned} &= \sum_k g_{kM}\langle e^{ikN\Omega t}\frac{dt}{dq_*}\sin 2q_*\rangle = \frac{1}{\Omega^2}\sum_k g_{kM}\langle e^{ikN\Omega t}(V-\cos(\Omega t+\phi)\sin 2q_*\rangle \\ &= \frac{1}{\Omega^2}\sum_k g_{kM}\left(V\langle e^{ikN\Omega t}\sin 2q_*\rangle - \frac{e^{i\phi}}{2}\langle e^{i(kN+1)\Omega t}\sin 2q_*\rangle - \frac{e^{-i\phi}}{2}\langle e^{i(kN-1)\Omega t}\sin 2q_*\rangle\right) \end{aligned} \tag{5.82}$$

We can exclude a case where $N=1$ which corresponds to a correction for integer steps. Also from the harmonic expansion formula for $\sin 2q_*$ we see that we can exclude summation over $k=0$, thus substituting it in we can get:

$$\langle\frac{dt}{dq_*}g(t)\sin 2q_*\rangle_\Omega = -4\Omega\sum_{k>0}\frac{\mathrm{Re}\{\mathrm{g_{kM}e^{-ikN\phi}}\}}{y^{kN}} \tag{5.83}$$

FIRST ORDER CORRECTION TO $\sin q_*/\dot{q}_*$

Previously we neglected corrections coming from the autonomous equation. Let's now consider it with the help of perturbation theory. The equation which we analyze is

$$\dot{q}_\star = V-\sin q_\star + C\sin 2q_\star \tag{5.84}$$

This equation we can expand up to the first order $q_\star = q_* + \delta q_*$:

$$\dot{q}_* = V-\sin q_* \tag{5.85}$$

$$\delta\dot{q}_* = -\cos q_*\delta q_* + C\sin 2q_* \tag{5.86}$$

Of the main interest to us is $\delta(\sin q_*/\dot{q}_*)$ which with $f(t)$ can give rise to the fractional steps. First we can expand

$$\sin q_\star = \sin(q_*+\delta q_*) = \sin q_* + \cos q_*\delta q_* \tag{5.87}$$

$$\frac{1}{\dot{q}_\star} = \frac{1}{\dot{q}_*+\delta\dot{q}_*} = \frac{1}{\dot{q}_*} - \frac{1}{\dot{q}_*^2}\delta\dot{q}_* \tag{5.88}$$

This allows us to rewrite the first order correction as simple as:

$$\delta\left(\frac{\sin q_*}{\dot{q}_*}\right) = \frac{\cos q_*}{\dot{q}_*}\delta q_* - \frac{\sin q_*}{\dot{q}_*^2}\delta \dot{q}_* \tag{5.89}$$

Plugging in expression for $\delta\dot{q}$ and $\frac{\sin q_*}{\dot{q}_*} = \frac{V}{\dot{q}_*} - 1$ we can rewrite the correction as follows:

$$\begin{aligned}\delta\left(\frac{\sin q_*}{\dot{q}_*}\right) &= -2C\cos q_*\left(\frac{V}{\dot{q}_*} - 1\right)^2 + \frac{V\cos q_*}{\dot{q}_*^2}\delta q_* \\ &= -2CV^2\frac{\cos q_*}{\dot{q}_*^2} - 2C\cos q_* + 4CV\frac{\cos q_*}{\dot{q}_*} + \frac{V\cos q_*}{\dot{q}_*^2}\delta q_*\end{aligned} \tag{5.90}$$

It turns out that $\frac{\cos q_*}{\dot{q}_*} = \frac{1}{\Omega}\sin(\Omega t + \phi)$ which we can derive from knowing $\frac{\sin q_*}{\dot{q}_*}$ and $\frac{1}{\dot{q}_*}$. We also know $\frac{1}{\dot{q}_*} = \frac{1}{\Omega^2}(V - \cos(\Omega t + \phi))$ plugging that in the formula above gives us:

$$\begin{aligned}\delta\left(\frac{\sin q_*}{\dot{q}_*}\right) = 2C\left(2\frac{V}{\Omega} - \frac{V^3}{\Omega^3}\right)\sin(\Omega t + \phi) + C\frac{V^2}{\Omega^3}\sin(2(\Omega t + \phi)) \\ - 2C\cos q_* + \frac{V}{\Omega}\sin(\Omega t + \phi)\frac{\delta q_*}{\dot{q}_*}\end{aligned} \tag{5.91}$$

It is fairly easy to derive that $\delta q_* = \frac{C}{\dot{q}_*}\int^t \frac{\sin 2q_*}{\dot{q}_*}dt$ which we can plug in and obtain an intermediate result before we do introduce infinite sums:

$$\begin{aligned}\delta\left(\frac{\sin q_*}{\dot{q}_*}\right) = 2C\left(2\frac{V}{\Omega} - \frac{V^3}{\Omega^3}\right)\sin(\Omega t + \phi) + C\frac{V^2}{\Omega^3}\sin(2(\Omega t + \phi)) \\ - 2C\cos q_* + C\frac{V}{\Omega}\sin(\Omega t + \phi)\int^t \frac{\sin 2q_*}{\dot{q}_*}dt\end{aligned} \tag{5.92}$$

In the last step we shall plug in the series expansions of $\cos q_*$:

$$\cos q_* = -2\Omega\sum_{k>0}\frac{1}{y^k}\sin(k(\Omega t + \phi)) \tag{5.93}$$

and $S(t) = \int^t \frac{\sin 2q_*}{\dot{q}_*}dt$ from 5.80 resulting in:

$$\begin{aligned}\delta\left(\frac{\sin q_*}{\dot{q}_*}\right) = C\left(\frac{4V}{\Omega} - \frac{2V^3}{\Omega^3} - \frac{4\Omega}{y} - \frac{V}{\Omega y^2} - \frac{V}{\Omega}S(0)\right)\sin(\Omega t + \phi) \\ + C\left(\frac{V^2}{\Omega^3} - 4\frac{\Omega}{y^2} - \frac{2V}{3y^3\Omega} - \frac{V(\Omega + y)}{\Omega^3 y^2}\right)\sin(2(\Omega t + \phi)) \\ 2C\sum_{k>2}\left(\frac{V}{\Omega(k-1)y^{k-1}} - \frac{V}{\Omega(k+1)y^{k+1}} - \frac{2\Omega}{y^k}\right)\sin(k(\Omega t + \phi))\end{aligned} \tag{5.94}$$

This result have been verified numerically. See a Pluto notebook `fractional.jl` in [40] for more details.

A formula for half-steps ($N = 2$)

To obtain the real step width we can in fact consider $f(t) = \cos(q_g(t)/2)$ and $g(t) = \sin^2(q_g(t)/2)$ which gives equation for slowly varying phase at non-integer frequencies:

$$\frac{\Omega}{V}\dot{\phi} = \delta V - \frac{\Omega^2}{V}\langle f(t)\frac{\sin q_\star}{\dot{q}_\star}\rangle + \frac{\Omega^2}{V}\langle g(t)\frac{\sin 2q_*}{\dot{q}_*}\rangle \tag{5.95}$$

We are only interested in the half steps $M\omega = 2\Omega$. Thus we can replace

$$\frac{\sin q_\star}{\dot{q}_\star} = \alpha\kappa\sin(2(\Omega t + \phi)) \qquad \kappa = \frac{V^2}{\Omega^3} - 4\frac{\Omega}{y^2} - \frac{2V}{3y^3\Omega} - \frac{V(\Omega + y)}{\Omega^3 y^2} \tag{5.96}$$

Thus the average

$$\langle f(t)\delta\left(\frac{\sin q_\star}{\dot{q}_\star}\right)\rangle = \alpha\kappa J_M\left(\frac{A}{2}\right)\cos\frac{q_0}{2}\sin 2\phi \tag{5.97}$$

Denoting with $H(\phi)$:

$$H_{2M}(\phi, y) = \sin q_0 \sum_{kM\in odd}\frac{J_{kM}(A)}{y^{2k}}\sin(2k\phi) - \cos q_0 \sum_{kM\in even}\frac{J_{kM}(A)}{y^{2k}}\cos(2k\phi) \tag{5.98}$$

the second average according to 5.83 can be rewritten as follows:

$$\langle g(t)\frac{\sin 2q_*}{\dot{q}_*}\rangle = 2\Omega H_{2M}(\phi, y) \tag{5.99}$$

Plugging averages back to an equation of slowly varying phase gives us:

$$\frac{\Omega}{V}\dot{\phi} = \delta V - \alpha\kappa\frac{\Omega^2}{V}J_M\left(\frac{A}{2}\right)\cos\frac{q_0}{2}\sin 2\phi + 2\frac{\Omega^3}{V}H_{2M}(\phi, y) \tag{5.100}$$

Thus the step is:

$$\Delta V_{2M} = \frac{\Omega^2}{V}(\max_\phi - \min_\phi)\left(2\Omega H_{2M}(\phi, y) - \alpha\kappa J_M\left(\frac{A}{2}\right)\cos\frac{q_0}{2}\sin 2\phi\right) \tag{5.101}$$

References

[1] D. McCumber and B. Halperin, *Time scale of intrinsic resistive fluctuations in thin superconducting wires*, Physical Review B **1**, 1054 (1970), cited By 418.

[2] J. Langer and V. Ambegaokar, *Intrinsic resistive transition in narrow superconducting channels*, Physical Review **164**, 498 (1967), cited By 604.

[3] K. Arutyunov, D. Golubev, and A. Zaikin, *Superconductivity in one dimension*, Physics Reports **464**, 1 (2008).

[4] C. Lau, N. Markovic, M. Bockrath, A. Bezryadin, and M. Tinkham, *Quantum phase slips in superconducting nanowires*, Physical Review Letters **87** (2001), 10.1103/physrevlett.87.217003.

[5] T. Aref, A. Levchenko, V. Vakaryuk, and A. Bezryadin, *Quantitative analysis of quantum phase slips in superconducting* $mo_{76}ge_{24}$ *nanowires revealed by switching-current statistics*, Phys. Rev. B **86**, 024507 (2012).

[6] J. N. Voss, Y. Schön, M. Wildermuth, D. Dorer, J. H. Cole, H. Rotzinger, and A. V. Ustinov, *Eliminating quantum phase slips in superconducting nanowires*, ACS Nano **15**, 4108 (2021).

[7] J. Mooij and C. Harmans, *Phase-slip flux qubits*, New Journal of Physics **7**, 219 (2005).

[8] O. V. Astafiev, L. B. Ioffe, S. Kafanov, Y. A. Pashkin, K. Y. Arutyunov, D. Shahar, O. Cohen, and J. S. Tsai, *Coherent quantum phase slip*, Nature **484**, 355 (2012).

[9] J. Peltonen, O. Astafiev, Y. Korneeva, B. Voronov, A. Korneev, I. Charaev, and J. Tsai, *Coherent flux tunneling through nbn nanowires*, Physical Review B **88** (2013), 10.1103/physrevb.88.220506.

[10] I. M. Pop, I. Protopopov, F. Lecocq, Z. Peng, B. Pannetier, O. Buisson, and W. Guichard, *Measurement of the effect of quantum phase slips in a josephson junction chain*, Nature Physics **6**, 589 (2010).

[11] J. E. Mooij and Y. V. Nazarov, *Superconducting nanowires as quantum phase-slip junctions*, Nature Physics **2**, 169 (2006).

[12] M. Vanević and Y. V. Nazarov, *Quantum phase slips in superconducting wires with weak inhomogeneities*, Physical Review Letters **108**, 187002 (2012).

[13] A. M. Hriscu and Y. V. Nazarov, *Model of a proposed superconducting phase slip oscillator: A method for obtaining few-photon nonlinearities*, Phys. Rev. Lett. **106**, 077004 (2011).

[14] A. M. Hriscu and Y. V. Nazarov, *Coulomb blockade due to quantum phase slips illustrated with devices*, Phys. Rev. B **83**, 174511 (2011).

[15] A. M. Hriscu and Y. V. Nazarov, *Quantum synchronization of conjugated variables in a superconducting device leads to the fundamental resistance quantization*, Phys. Rev. Lett. **110**, 097002 (2013).

[16] A. Di Marco, F. W. J. Hekking, and G. Rastelli, *Quantum phase-slip junction under microwave irradiation*, Phys. Rev. B **91**, 184512 (2015).

[17] G. Rastelli, I. M. Pop, and F. W. J. Hekking, *Quantum phase slips in josephson junction rings*, Phys. Rev. B **87**, 174513 (2013).

[18] S. Corlevi, W. Guichard, F. W. J. Hekking, and D. B. Haviland, *Phase-charge duality of a josephson junction in a fluctuating electromagnetic environment*, Phys. Rev. Lett. **97**, 096802 (2006).

[19] V. E. Manucharyan, N. A. Masluk, A. Kamal, J. Koch, L. I. Glazman, and M. H. Devoret, *Evidence for coherent quantum phase slips across a josephson junction array*, Phys. Rev. B **85**, 024521 (2012).

[20] M. Houzet and L. I. Glazman, *Critical fluorescence of a transmon at the schmid transition*, Phys. Rev. Lett. **125**, 267701 (2020).

[21] R. Kuzmin, N. Grabon, N. Mehta, A. Burshtein, M. Goldstein, M. Houzet, L. I. Glazman, and V. E. Manucharyan, *Inelastic scattering of a photon by a quantum phase slip*, Phys. Rev. Lett. **126**, 197701 (2021).

[22] D. V. Averin, A. B. Zorin, and K. K. Likharev, *Bloch oscillations in small josephson junctions*, Soviet Physics - JETP **61**, 407 (1985).

[23] G. Schön and A. Zaikin, *Quantum coherent effects, phase transitions, and the dissipative dynamics of ultra small tunnel junctions*, Physics Reports **198**, 90156 (1990).

[24] U. Geigenmüller and G. Schön, *Single electron effects and bloch oscillations in normal and superconducting tunnel junctions*, Physica B: Condensed Matter **152**, 186 (1988).

[25] N. Constantino, M. Anwar, O. Kennedy, M. Dang, P. Warburton, and J. Fenton, *Emergence of quantum phase-slip behaviour in superconducting NbN nanowires: DC electrical transport and fabrication technologies*, Nanomaterials **8**, 442 (2018).

[26] J. Fenton and J. Burnett, *Superconducting nbn nanowires and coherent quantum phase-slips in dc transport*, IEEE Transactions on Applied Superconductivity **26**, 1 (2016).

[27] L. Kuzmin and D. Haviland, *Observation of the bloch oscillations in an ultrasmall josephson junction*, Physical Review Letters **67**, 2890 (1991).

[28] J. Lehtinen, K. Zakharov, and K. Arutyunov, *Coulomb blockade and bloch oscillations in superconducting ti nanowires*, Physical Review Letters , 109 (2012).

[29] C. Webster, J. Fenton, T. Hongisto, S. Giblin, A. Zorin, and P. Warburton, *Nbsi nanowire quantum phase-slip circuits: dc supercurrent blockade, microwave measurements, and thermal analysis*, Physical Review B **87** (2013), 10.1103/physrevb.87.144510.

[30] Z. M. Wang, J. S. Lehtinen, and K. Y. Arutyunov, *Towards quantum phase slip based standard of electric current*, Applied Physics Letters **114**, 242601 (2019).

[31] J. P. Pekola, O.-P. Saira, V. F. Maisi, A. Kemppinen, M. Möttönen, Y. A. Pashkin, and D. V. Averin, *Single-electron current sources: Toward a refined definition of the ampere*, Reviews of Modern Physics **85**, 1421 (2013).

[32] T. Hongisto and A. Zorin, *Single-charge transistor based on the charge-phase duality of a superconducting nanowire circuit*, Physical Review Letters **108** (2012), 10.1103/physrevlett.108.097001.

[33] S. T. Skacel, *Development of superconducting devices employing coherent quantum phase slip*. KIT-Bibliothek (2019).

[34] S. De Graaf, S. Skacel, T. Hönigl-Decrinis, R. Shaikhaidarov, H. Rotzinger, S. Linzen, and O. Astafiev, *Charge quantum interference device*, Nature Physics **14**, 590 (2018).

[35] K. Arutyunov and J. Lehtinen, *Junctionless cooper pair transistor*, Physica C: Superconductivity and its Applications **533**, 158 (2017), ninth international conference on Vortex Matter in nanostructured Superdonductors.

[36] F. Romeo and R. De Luca, *Effective non-sinusoidal current-phase dependence in conventional d.c. squids*, Physics Letters A **328**, 330 (2004).

[37] C. Vanneste, C. Chi, W. Gallagher, A. Kleinsasser, S. Raider, and R. Sandstrom, *Shapiro steps on current-voltage curves of dc squids*, Journal of Applied Physics **64**, 242 (1988).

[38] K. Likharev, *Dynamics of Josephson Junctions and Circuits* (Taylor & Francis, 1986).

[39] P. Bak, *The devil's staircase*, Physics Today **39**, 38 (1986), https://doi.org/10.1063/1.881047 .

[40] J. Erdmanis, *Data, software and supplementary notes for this paper.* (2021).

ACKNOWLEDGEMENTS

I am grateful that my PhD has finally ended. It would not have been possible without funding, support, direction, engagement and design of the projects from my supervisor, prof.dr. Yuli Nazarov. The scope unquestionably had spanned fascinating subjects of superconductivity at the nanoscale and has given me a taste of various topics. I am also greatly indebted to Arpad Lukacs for showing me the exciting side of mathematical physics, breaking down complex ideas, and repeatedly teaching them to me. You were also exceptionally articulated and had elaborate opinions on how things are, which made debates with you so fun and engaging, fuelled from our different points of view, a true treasure in academia and for my personal growth. I thank Victor Boogers for being engaged in my supervised project, even though I later realized I had designed a weak project. I thank Yuli for forgiving me and helping us to get the best possible outcome.

My personality grew tremendously in regular coffee meetings at 10.30 am and lunch breaks at noon, which occasionally transcended together, one of the things I missed most during covid. The clear, sharp and articulated way Anton Akhamerow participated was admirable and gave me a good set of stimulating thoughts. I would also like to thank Albert, Kim, Daniel, Satish, Pablo, Rafal, Joseph, Tomas, Bas, Adriaan, Piotr, Sebastian, Victoria, Vincent, Sanchar and others for being active participants who warmed and filled up my day with thoughts and hope. I am thankful to Casimir school for organizing the winter retreat at Courchevel, facilitating cross-discipline interactions and reimagining poster sessions without text where I made my best artwork.

I got great admiration and humility from my room colleague Xin at F336. Your ability to endure with about half of the PhD salary around you and your drive to experiment and learn new skills from others while being fine to be different was inspirational. It made me realize the privilege I have been given. Knowing my colleague Yuguang was also a rewarding pleasure. Getting to hear you playing the piano in the Nordita summer school at Sweeden was a jaw-dropping moment. Your drive and obsession with getting to know precisely how things are made me aware of my own thought processes. I also loved your openness to adventures. To sleep in the boat in Geneva overnight because we had booked our flight one day too early for summer school (the hotels in Geneva were really expensive) and go for a small boat trip in the morning. I am also grateful to Vincent for warm welcoming Yuguang and me at your home and involving us in the vine collecting and making process in idyllic scenery.

I thank Graduate school for being here to provide a variety of courses and support. I genuinely found courses as a great way to get together and socialize with other students I would not get together otherwise and to learn many new communication strategies, and to keep checks and balances of the whole health of TU Delft. I also thank for genuine concerns from the graduate school at the end of my PhD. In particular, I thank Estcher Plomp for giving me a frank and thoughtful assessment and helping to recollect my thoughts. This gave me confidence and a path to finish despite having a lot on my plate.

Often when I was under stress, my hobbies and leisure saved me. I am thankful to WTOS for bringing me in and letting me participate in group rides and come with you on cycling trips to Belgium, where I revived my interest in road cycling and admired the organizational abilities of Dutch. I also thank Yuli for letting me to spend almost all my vacation days during the course of my PhD and to return home when covid started.

My greatest indebtedness goes to my family, who, although were incapable of understanding what I do, always were empathetic, giving me security and strength to challenge the way things have been in no matter where my determination would lead me. Particularly I thank my mom and granny for preparing me food and welcoming me for extended summer vacations where I cycled, swam and read many books; my sister for a tree tent in which I slept all summer months providing me with sleep when I went to bed late and agitated at the last months of my PhD. You are all I need to be empowered and creative and to incubate my next venture.

Curriculum Vitæ

Jānis Erdmanis

18-05-1992	Born in Valmiera, Latvia.

Education

2003–2011	Valmieras Valsts Gimnazija Valmiera, Latvia
2011–2014	BSc. in Physics University of Latvia *Thesis:* Application of Wigner function for characterization of single electron sources *Promotor:* Assoc.prof.dr. Vyacheslavs Kashcheyevs
2014–2016	MSc. in Physics University of Latvia *Thesis:* Magnetic liquid droplet dynamics and equilibrium figures in external field *Promotor:* Prof.dr. Andrejs Cebers
2015	Erasmus exchange programme at Umeå University
2016	CERN Summer Student Programme *Project:* Pushing bounds for higsino mass with high luminosity LHC data *Promotor:* Dr. Simone Amoroso
2017–2021	PhD. in Physics Delft University of Technology, Netherlands *Thesis:* Quantum effects of superconducting phase *Promotor:* Prof.dr. Yuli V. Nazarov *Promotor:* Prof.dr. Yaroslav M. Blanter

Awards

2011–2014	Study scholarship “Jura Melbarza pieminas stipendija” from “Vitolu fonds”

LIST OF PUBLICATIONS

5. **Janis Erdmanis**, Árpád Lukács, Yuli Nazarov *Drastic effect of weak interaction near special points in semiclassical multiterminal superconducting nanostructures* https://arxiv.org/abs/2107.14105 (2021), submitted to PRB.

4. **Janis Erdmanis**, Yuli Nazarov, *Synchronization of Bloch oscillations by gate voltage modulation*, https://arxiv.org/abs/2107.10565 (2021), submitted to PRB.

3. Victor Boogers, **Janis Erdmanis**, Yuli Nazarov, *Holonomic quantum manipulation in the Weyl Disk*, https://arxiv.org/abs/2107.04814 (2021), submitted to PRB.

2. **Janis Erdmanis**, Árpád Lukács, Yuli V. Nazarov *Weyl Disks: Theoretical prediction*, Physical Review B (2018).

1. **J. Erdmanis**, G. Kitenbergs, R. Perzynski, A. Cebers, *Magnetic micro-droplet in rotating field: numerical simulation and comparison with experiment.*, Journal of Fluid Mechanics (2017).

Casimir PhD Series 2021-43
ISBN 978-90-8593-507-0